

AN IDEAL JOSEPHSON JUNCTION IN AN ULTRACOLD TWO-DIMENSIONAL FERMI GAS

Dissertation
zur Erlangung des Doktorgrades
an der Fakultät für Mathematik, Informatik und Naturwissenschaften
Fachbereich Physik
der Universität Hamburg

vorgelegt von
Niclas Clemens Luick

Hamburg, im Mai
2020

Gutachter der Dissertation Prof. Dr. Henning Moritz
Prof. Dr. Ludwig Mathey

Vorsitzender des Fach-Promotionsausschusses Physik Prof. Dr. Günter H. W. Sigl

Leiter des Fachbereichs Physik Prof. Dr. Wolfgang Hansen

Dekan der Fakultät MIN Prof. Dr. Heinrich Graener

ABSTRACT

Achieving a better understanding of strongly correlated quantum systems is a fascinating scientific endeavour which could provide the basis for the construction of novel materials with unprecedented properties such as room-temperature superconductors. Of particular interest are strongly correlated two-dimensional (2D) systems which are present in almost all known superconductors with high critical temperatures. However, even after decades of research the origin for such unconventional superconductivity is still under debate. Ultracold 2D Fermi gases have emerged as clean and controllable model systems to simulate such strongly correlated 2D quantum states, but so far superfluidity has not been directly observed in these systems.

In this thesis, I report on the realisation of a Josephson junction in an ultracold 2D Fermi gas which clearly demonstrates phase coherence and provides strong evidence for superfluidity. We measure the frequency of Josephson oscillations as a function of the phase difference across the junction and find excellent agreement with a sinusoidal current-phase relation. This result shows that the Josephson junction is well described as an ideal tunnel junction whose critical current is directly linked to the wave function overlap of the coupled superfluids. We determine this critical current in the crossover from tightly bound molecules to weakly bound Cooper pairs and thereby realize a probe for 2D superfluidity in the strongly correlated regime.

This accomplishment of an ideal Josephson junction was enabled by various experimental advances in the preparation, manipulation and characterisation of ultracold Fermi gases - in particular by our realisation of homogeneous 2D systems - which were achieved during the course of this thesis and make our system an ideal platform to gain further insight into the nature of strongly correlated 2D quantum matter.

ZUSAMMENFASSUNG

Ein besseres Verständnis stark korrelierter Quantensysteme zu entwickeln ist eine faszinierende wissenschaftliche Herausforderung, welche die Konstruktion neuartiger Materialien mit einzigartigen Eigenschaften, wie z.B. Raumtemperatur-Supraleitern, ermöglichen könnte. Von besonderem Interesse sind stark korrelierte zweidimensionale (2D) Systeme, welche in fast allen Supraleitern mit den höchsten kritischen Temperaturen zu finden sind. Selbst nach jahrzehntelanger Forschung wird immer noch über den Ursprung solch unkonventioneller Supraleitung debattiert. Ultrakalte 2D Fermigase sind ideale Modellsysteme um stark korrelierte 2D Quantenzustände in einer sauberen und gut kontrollierten Umgebung zu simulieren. Bisher gibt es jedoch keinen direkten Nachweis von Suprafluidität in diesen Systemen.

In dieser Arbeit wird die Realisierung eines Josephson-Kontakts in einem ultrakalten 2D Fermigas präsentiert und damit ein klarer Nachweis für Phasenkohärenz und starke Evidenz für Suprafluidität in diesem Gas erbracht. Wir messen die Frequenz der Josephson Oszillationen als Funktion der Phasendifferenz am Josephson-Kontakt und finden eine hervorragende Übereinstimmung mit einer sinusoidalen Strom-Phasen-Beziehung. Dieses Resultat zeigt, dass der Josephson-Kontakt als idealer Tunnel-Kontakt beschrieben werden kann dessen kritischer Strom direkt vom Wellenfunktionsüberlapp der gekoppelten Suprafluide bestimmt wird. Wir messen diesen kritischen Strom im Übergang von tief gebundenen Molekülen zu schwach gebundenen Cooper Paaren und untersuchen damit 2D Suprafluidität im stark korrelierten Regime.

Diese Realisierung eines idealen Josephson-Kontakts wurde durch zahlreiche experimentelle Fortschritte im Bereich der Erzeugung, Manipulation, und Charakterisierung von ultrakalten Fermigasen ermöglicht - insbesondere durch unsere Realisierung von homogenen 2D Systemen - welche im Rahmen dieser Arbeit erreicht wurden und unser System als ideale Plattform etablieren, um weitere Einblicke in die Natur stark korrelierter 2D Quantenmaterie zu gewinnen.

CONTENTS

1	Introduction	3
2	Summary of the main results in this thesis	9
2.1	An ideal Josephson junction in an ultracold two-dimensional Fermi gas	9
2.2	Two-dimensional homogeneous Fermi gases	10
2.3	Calibrating high intensity absorption imaging	10
2.4	Further publications within this thesis	11
I	Experimental Setup and Methods	13
3	Fundamentals of ultracold 2D Fermi gases	15
3.1	Two-body scattering properties	15
3.2	Superfluidity in a 2D Fermi gas	18
4	Experimental apparatus and upgrades	21
4.1	Overview of the experimental sequence	21
4.2	Replacing the metal science cell by a glass cell	25
4.3	Improving the cooling resonator setup	26
5	Novel methods for the preparation and characterisation of ultracold 2D Fermi gases	31
5.1	Preparing a single-layer ultracold 2D Fermi gas	31
5.2	Projecting tailored potentials	34
5.3	Calibrating high intensity absorption imaging	35
5.4	Measuring the momentum distribution using matter wave focusing	37
II	Homogeneous Two-Dimensional Fermi Gases	43
6	Homogeneous Two-Dimensional Fermi Gases	45
6.1	Experimental realisation of a homogeneous 2D Fermi gas	46
6.2	Measurement of the equation of state	48
6.3	Observation of Pauli blocking in the momentum distribution	48
6.4	Measuring $\tilde{n}(\mathbf{k})$ of interacting homogeneous 2D Fermi gases	52
III	An Ideal Josephson Junction in an Ultracold Two-dimensional Fermi Gas	55
7	Theoretical and experimental background of Josephson junctions	59
7.1	Superconducting Josephson junctions	59
7.2	Superfluid Josephson junctions: the crossover from dissipative phase slips to coherent Josephson dynamics	65
7.3	Cold atom Josephson junctions	66
8	Realisation of a Josephson junction in an ultracold two-dimensional Fermi gas	69

8.1	Experimental methods	72
8.2	Understanding the Josephson dynamics in an LC circuit model	75
8.3	Comparison with numerical simulations	76
9	Observation of a sinusoidal current-phase relation in a cold atom Josephson junction	79
9.1	Probing the current-phase relation of an ideal Josephson junction	79
9.2	Estimate of higher order contributions	83
9.3	Methods	84
10	The critical current in the 2D BEC-BCS crossover	87
10.1	Results	88
10.2	Methods	91
11	Conclusion and outlook	95
11.1	Outlook	96
A	Calibrating High-Intensity Absorption imaging	99
A.1	Introduction	99
A.2	High intensity imaging	100
A.3	Experimental setup	101
A.4	Method	103
A.5	Conclusion	107
	ACKNOWLEDGEMENTS	127

The quest to understand high-temperature superconductivity

A fascinating aspect of nature is that systems with many interacting particles can give rise to the emergence of collective phenomena that are qualitatively different from the behaviour of the system at the single particle level [1]. A prominent example for such an emergent behaviour with far-reaching technological applications is superconductivity. While for normal conductors the movement of electrons leads to dissipation, in superconductors these electrons can collectively flow through the material without any friction once the system is cooled below its critical temperature T_c . Conventional superconductivity generally occurs only at very low temperatures of a few Kelvin, but the discovery of superconductivity in the cuprates [2] revealed that certain materials can remain superconducting up to much higher temperatures, with a present record of $T_c = 133$ K [3]. Explaining the origin for such high critical temperatures is currently one of the most fascinating unsolved problems in physics with the tantalising prospect of understanding how to construct a material at ambient pressure¹ that remains superconducting at room temperature.

Of particular interest is the empirical observation that superconductors with the highest critical temperatures involve two-dimensional (2D) structures. The most prominent examples are cuprates such as YBCO [5] and BSCCO [6], where there is strong evidence that superconductivity is restricted to two-dimensional CuO_2 planes [7], and iron pnictides such as FeSe, where it was found that reducing the thickness of the material down to a single atomic layer could increase the critical temperature from its bulk value of 9 K up to 80 K–100 K [8, 9]. While both cuprates and iron based superconductors are complex compounds in which it is difficult to isolate the role of a reduced dimensionality, very recently high² critical temperatures were also reported in a simple purely carbon based two-dimensional superconductor based on twisted bilayer graphene (TBG) [10]. This apparent link between high critical temperatures and a reduced dimensionality is remarkable, because thermal fluctuations become more pronounced as the dimensionality is reduced [11, 12]. In fact, 2D superconductivity can only exist in a competition between order and fluctuations as explained by Berezinskii-Kosterlitz-Thouless (BKT) theory [13–15].³ Understanding the origin for high critical temperatures is challenging, because high- T_c materials are not just quantitatively but qualitatively different from conventional superconductors with low critical temperatures. Conventional superconductors such as Nb-Ti are well understood by Bardeen-Cooper-Schrieffer (BCS) theory [18], which predicts that a weak attractive interaction between electrons leads to

¹ Very recently, it was shown that LaH_{10} remains superconducting up to $T_c = 250$ K under extremely high pressures of 170 GPa, but the relevance of this result for high-temperature superconductivity at ambient pressure is not clear [4].

² The authors of [10] report on the observation of a critical temperature of $T_c = 1.7$ K, which is small in absolute terms but among the highest relative critical temperatures $T_c/T_F \approx 0.1$ when normalized to the low Fermi Temperature $T_F \propto n$ due to the very low carrier density n in the material.

³ Evidence for the relevance of BKT theory for high-temperature superconductivity is provided by measurements of the spin relaxation rate in YBCO which show that the critical temperature $T_c \propto n_s$ is directly proportional to the superfluid density n_s as expected from BKT theory for superconductivity in 2D [16, 17].

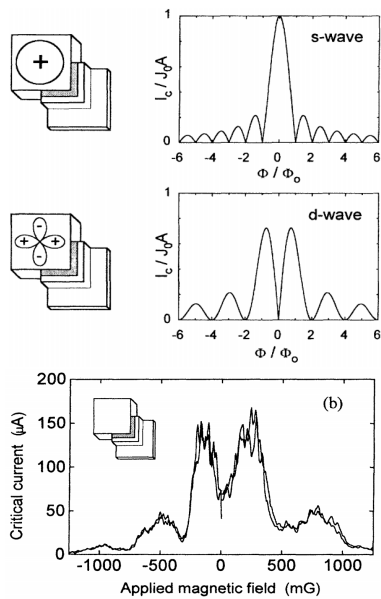


Figure 1.1: Experimental demonstration of the d-wave pairing symmetry in cuprate superconductors. For a corner Josephson junction fabricated with YBCO, the critical current was observed to have a minimum at vanishing applied magnetic field. This provides clear evidence for a superconducting order parameter with a d-wave symmetry, which is expected to introduce a phase shift of π around the loop of circulating supercurrents. For more details on this experiment see chapter 7.1.2. Adapted from [29].

the formation of bosonic-like Cooper pairs which condense below T_c into a macroscopic quantum state described by the pair wave function Ψ . In conventional superconductors, this weak attractive interaction is provided by electrons interacting with the surrounding crystal lattice. High-temperature superconductivity, however, generally arises from a system with *strong repulsive* interactions, i.e. when electrons are removed from a Mott-insulating state [19]. Explaining the mechanism for electron pairing despite these repulsive interactions is one of the key challenges to understand unconventional superconductivity.

The minimal theoretical model that is often assumed to capture the essence of unconventional superconductivity in strongly correlated 2D systems is the doped repulsive 2D Hubbard model [20–22]. In this model, the dynamics of electrons in the periodic potential formed by the nuclei are approximated as a discrete 2D lattice on which electrons can tunnel between neighbouring lattice sites and interact repulsively on each site [23]. Developing a theoretical understanding of such strongly correlated 2D systems, however, is an extremely challenging task. On the one hand, basic theoretical approaches such as perturbation theory and mean field theory fail in these systems because the strong interactions between particles cannot be treated as a small perturbation from the non-interacting limit and the strong fluctuations due to the reduced dimensionality cause mean field approaches to fail. On the other hand, exact diagonalisation becomes intractable on a classical computer already for system sizes as small as ~ 20 sites [24–26] and the powerful numerical quantum Monte Carlo method suffers from the fundamental fermionic sign problem away from half-filling [27]. Therefore, despite the fact that the Hubbard model has been the most widely studied system in condensed matter theory for decades [28], only recently numerical methods have started to explore solutions in the strongly correlated regime relevant to high- T_c materials [22]. Due to this lack of theoretical understanding the importance of experiments for our understanding of high-temperature superconductivity cannot be overstated.

Probing the nature of high-temperature superconductors with Josephson junctions

In particular, Josephson junctions have proved to be an indispensable experimental tool to gain insight into the nature of unconventional superconductivity [7, 30]. Based on the basic principle that a phase difference ϕ between two superconductors separated by a weak link drives a current $I(\phi)$, Josephson junctions offer a unique sensitivity to the phase of the superconducting order parameter Ψ . This was utilized to establish the following key characteristics of cuprate superconductors: First, it was demonstrated that despite their repulsive interactions the electrons form pairs just like in conventional superconductors [31]. Second, it was unambiguously shown that the pairing gap $\Delta_{\mathbf{k}}$, which characterises the energy gained by forming such a pair of electrons with momenta $+\mathbf{k}$ and $-\mathbf{k}$, has a d-wave symmetry

$\Delta_{\mathbf{k}} \propto \cos(k_x) - \cos(k_y)$ (s. Fig. 1.1) [29, 32], which is in sharp contrast to the isotropic s-wave gap $\Delta_{\mathbf{k}} = \Delta_0$ found in conventional superconductors. These Josephson junction experiments provided an important benchmark for existing theories, which suggested a d-wave symmetry based on Anderson's resonating valence bond state [21, 33, 34]. While more recently further numerical evidence could be provided that the 2D Fermi Hubbard model can support d-wave superconductivity [22], the real difficulty remains to determine if its ground state is indeed superconducting. In the fragile balance between order and fluctuations [35, 36], it was observed that such a 2D system can support various other types of order such as the stripe phase which is assumed to be very close in energy to the superconducting state [37, 38]. Finally, for higher temperatures close to T_c , it is fundamentally unclear which of these competing ground states determines the conductance properties [35] and our basic understanding of solids in terms of a Fermi liquid of quasiparticles appears insufficient to describe the observed pseudogap and strange metal phases. While recently unconventional approaches from string theory [39, 40] and neural networks [41] were adopted, it remains unclear if our currently available methods are suited to describe such strongly correlated 2D quantum matter.

BEC-BCS superfluids:

Quantum simulators for high-temperature superconductivity

*"Nature isn't classical, dammit, and if you want to make a simulation of nature, you'd better make it quantum mechanical, and by golly it's a wonderful problem, because it doesn't look so easy."*⁴²

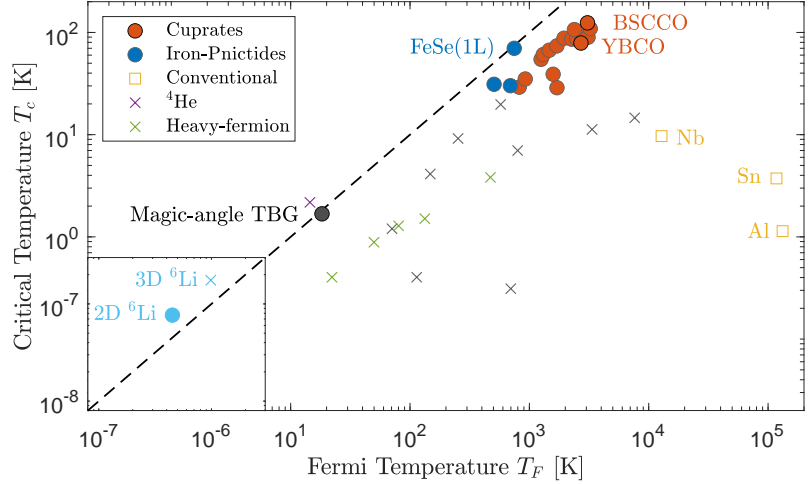
⁴² R. P. Feynman: , vol. 21, (1982)

Ultracold quantum gases are ideally suited to understand the role of reduced dimensionality for high-temperature superconductivity due to their unprecedented level of control over the preparation and characterisation of quantum many body states. In these systems, the periodic potential of solids can be directly emulated by an optical lattice formed by interfering laser beams [43]. While substantial progress has been made with such quantum simulators [44] starting from the ground-breaking realisation of Mott insulating states [45, 46] to the recent observation of a 2D antiferromagnet [47], d-wave superfluidity in such an optical lattice system is expected to require significantly lower temperatures than currently achievable.

Remarkably, fermionic superfluidity in ultracold quantum gases can be realised even without the presence of a lattice potential. The key to create such superfluids is the ability to introduce attractive interactions between fermions and thereby form pairs via *Feshbach resonances* [48]. The strength of these attractive interactions can be widely tuned to create pairs ranging from the limit of weakly bound Cooper pairs to deeply bound dimers and thereby realise s-wave superfluids in the entire crossover from BCS to Bose-Einstein condensation (BEC) [49]. Various experiments reached temperatures well below the critical temperatures for condensation [50–54] and superfluidity [55–59]

Figure 1.2: Critical temperature T_c in dependence of Fermi temperature T_F for various superconductors and superfluids as first shown in [60, 61] and recently revisited in the context of magic-angle TBG [10]. 2D or quasi-2D materials (filled circles) have the highest critical temperatures close to $T_c/T_F \approx 0.1$ (dashed diagonal line), which is the expected maximal critical temperature close to the 2D BEC-BCS crossover [62]. The critical temperature for ultracold 2D ^6Li was extracted from the measured critical temperature for pair condensation in [63]. Also, heavy-fermion (light green crosses) and other unconventional superconductors (grey crosses) have significantly higher critical temperatures than conventional superconductors (orange squares).

and enabled an extensive study of this strongly correlated superfluid in the BEC-BCS crossover.



⁴ For an extensive review of the application of the BEC-BCS crossover theory to high-temperature superconductors see [65].

While the pairing symmetry of such ultracold superfluids is not d-wave, it was already suggested in 1989 that the study of the BEC-BCS crossover can provide valuable insight into high-temperature superconductivity [64].⁴ In the BEC-BCS crossover picture, high critical temperatures are explained to arise from the short coherence lengths $\xi \sim 1/k_F$ observed in unconventional superconductors [10, 66–68], which are on the order of the interparticle spacing $\sim 1/k_F$ and thereby bring such materials in the strongly correlated regime, where the critical temperature T_c/T_F has a maximum [69]. Indeed, when the critical temperatures of superconductors are normalised to their natural energy scale set by the Fermi energy T_F [70], all unconventional superconductors lie in a band of similarly high critical temperatures of $T_c/T_F \sim 0.01 - 0.1$, while conventional BCS superconductors have a much lower value of $T_c/T_F < 0.0001$ (s. Fig. 1.2). Most notably, for magic-angle TBG with a coherence length of $\xi \approx 50$ nm and similar interparticle distance of ~ 26 nm the observed critical temperature of $T_c/T_F \sim 0.1$ agrees well with the expected maximal critical temperature in the 2D BEC-BCS crossover (s. Fig. 1.3) [62]. Finally, further evidence for the relevance of the BEC-BCS crossover to understand high- T_c materials is provided by the observation of fermionic pairing with a d-wave symmetry even above the critical temperature for superconductivity [71]. This measurement suggests a precursor of the superconducting phase with pre-formed pairs which are an essential property of systems in the BEC-BCS crossover - especially in 2D, where fermions can form pairs already at the two-body level for an arbitrary interaction strength.

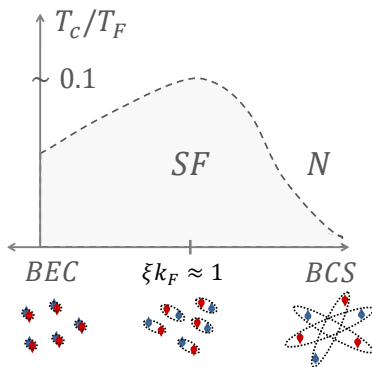


Figure 1.3: Illustration of the critical temperature T_c for superfluidity in the 2D BEC-BCS crossover following [72]. The critical temperature in units of the Fermi temperature T_F has a maximum in the strongly correlated regime when the Cooper pair size ξ is on the order of the interparticle spacing $\sim 1/k_F$.

Despite this apparent relevance for high-temperature superconductivity, only recently the 2D BEC-BCS crossover was started to be explored with ultracold Fermi gases [72–76]. While condensation of fermionic pairs [63] and signatures of pairing above the critical temperature were detected [77], superfluidity was not directly observed.

Furthermore, all experiments with 2D Fermi gases so far were performed in harmonic traps, which complicated a quantitative analysis of fundamental non-local properties of the system such as its momentum distribution [78].

In the course of this thesis, we achieved several major advances in the ability of ultracold atoms to model strongly correlated 2D quantum matter. As the main result, I present our realisation of a Josephson junction in an ultracold 2D Fermi gas, which we use to unambiguously show phase coherence and provide strong evidence for superfluidity in the entire 2D BEC-BCS crossover. This achievement was made possible by our realisation of a homogeneous 2D Fermi trapped in a box potential, which constitutes a textbook example of statistical physics and enables us to quantitatively measure its momentum distribution. These results are briefly summarized in the following chapter.

2

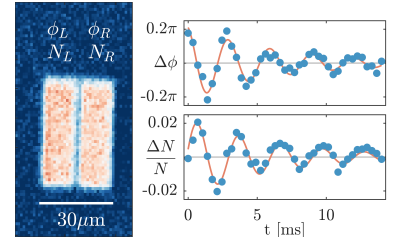
SUMMARY OF THE MAIN RESULTS IN THIS THESIS

2.1 An ideal Josephson junction in an ultracold two-dimensional Fermi gas

published in N. Luick, L. Sobirey, M. Bohlen, V.P. Singh, L. Mathey, T. Lompe, and H. Moritz, arXiv:1908.09776 (2019), accepted for publication in Science

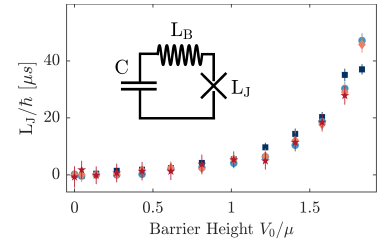
Observation of Josephson oscillations in a 2D Fermi gas

The main achievement of this thesis is the first realisation of a Josephson junction in an ultracold 2D quantum gas. In contrast to previous 3D cold atom junctions, we realize our junction with two homogeneous reservoirs separated by a tunnelling barrier, which makes it a much closer analog to the superconducting tunnel junctions ubiquitous in solid state systems. We control the initial phase difference ϕ_0 and observe Josephson oscillations in the relative phase $\phi = \phi_L - \phi_R$ and particle number $\Delta N = N_L - N_R$ between the two reservoirs.



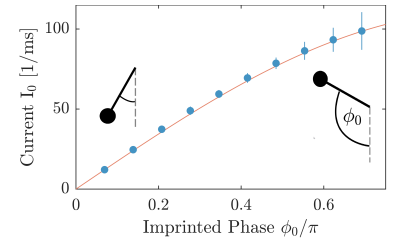
Understanding the Josephson dynamics via an LC circuit model

The dynamics of our junction can be quantitatively explained by an LC circuit model commonly used to describe superconducting Josephson junctions. We measure the oscillation frequency ω for various box sizes from $15 \mu\text{m}$ to $30 \mu\text{m}$ to show that our junction is well described by an inductance L_J which is only determined by the height V_0 of the tunnelling barrier.



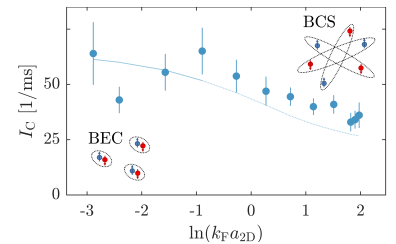
Observing the sinusoidal current-phase relation of an ideal Josephson junction

While Josephson junctions were extensively studied with ultracold atoms, the characteristic nonlinear current-phase relation could not be observed so far. We probe the current-phase relation of our junction by measuring the Josephson oscillation frequency for large phase excursions ϕ_0 and for the first time observe the sinusoidal form $I(\phi) = I_c \sin(\phi)$ in a cold atom Josephson junction.



The critical current: an in-situ probe for phase coherence in a 2D superfluid

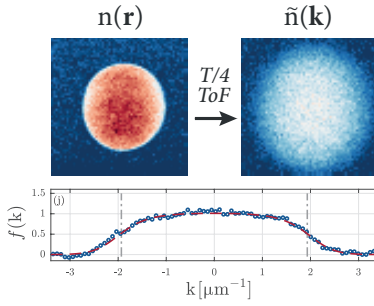
Finally, we observe that the Josephson oscillations, and hence our signature of superfluidity, persist across the entire 2D BEC-BCS crossover. We extract the critical current $I_c \propto n_c$, which for our ideal junction is determined by the wave function overlap and therefore provides access to the condensate density n_c . We determine $n_c \propto (1/L)^\eta$ in the bosonic limit and extract the algebraic scaling exponent η as a probe for the phase coherence of our 2D superfluid over the finite size L of our box.



2.2 Two-dimensional homogeneous Fermi gases

published in K. Hueck, N. Luick, L. Sobirey, J. Siegl, T. Lompe, and H. Moritz, *Phys. Rev. Lett.* **120**, 060402 (2018)

I contributed to the planning and conduction of experiments, the interpretation of our results and the writing of the publication. A detailed description of our realisation of homogeneous 2D Fermi gases is given in [79].



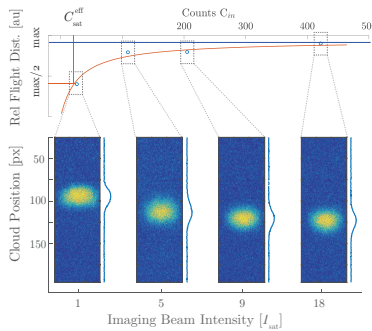
Previously, 2D Fermi gases have only been studied in harmonic trapping potentials. During the course of this work, we implemented an optical box potential in our experimental setup which enabled us to realise the first homogeneous 2D Fermi gases. In addition, we developed methods to locally manipulate the gas with a resolution on the order of the interparticle distance using a digital micromirror device (DMD) and extract its momentum distribution using matter wave focusing. We applied these methods to our homogeneous gas to measure its equation of state $n(\mu, T)$ and extract the momentum distribution $\tilde{n}(\mathbf{k})$ of interacting and non-interacting 2D Fermi gases, directly observing Pauli blocking in momentum space.

The high level of control over the preparation, manipulation and characterisation of our 2D Fermi gas achieved in the context of this work provided the foundation for the realisation of Josephson junctions described above. For future experiments, this homogeneous system will constitute an ideal starting point to realize the elusive Fulde-Ferrell-Larkin-Ovchinnikov state and study non-equilibrium dynamics of strongly correlated 2D quantum matter.

2.3 Calibrating high intensity absorption imaging

published in K. Hueck, N. Luick, L. Sobirey, T. Lompe, H. Moritz, L. Clark, and C. Chin, *Opt. Express* **25**, 8670 (2017)

I contributed to the planning and conduction of experiments, the data analysis and the writing of the publication. A detailed description of our calibration of high intensity absorption imaging is given in [79].



Our experiments described above require an accurate density determination which can be challenging for a 2D Fermi gas due to the requirement of low densities of $n \sim 1/\mu\text{m}^2$ to remain in the 2D regime. During the course of this thesis, we developed a method to calibrate the intensity I of our imaging beam relative to the saturation intensity I_{sat} which enables a quantitative density determination with an optimal signal-to-noise ratio in the regime of $I \sim I_{\text{sat}}$. For this calibration, we measure the momentum transferred from the imaging beam onto the atoms and determine the relative intensity at which the transferred momentum starts to saturate.

2.4 Further publications within this thesis

- **Observation of superfluidity in a strongly correlated two-dimensional Fermi gas**
L. Sobirey, N. Luick, M. Bohlen, H. Biss, H. Moritz, T. Lompe
 arXiv:2005.07607 (2020), submitted to Science
- **Sound propagation and quantum limited damping in a two-dimensional Fermi gas**
M. Bohlen, L. Sobirey, N. Luick, H. Biss, T. Enss, T. Lompe, H. Moritz
 arXiv:2003.02713 (2020)
- **Josephson junction dynamics in a two-dimensional ultracold Bose gas**
V.P. Singh, N. Luick, L. Sobirey, L. Mathey
 arXiv:2002.08375 (2020)
- **Note: Suppression of khz-frequency switching noise in digital micro-mirror devices**
K. Hueck, A. Mazurenko, N. Luick, T. Lompe, H. Moritz
 Review of Scientific Instruments **88**, 016103 (2017)
- **Detecting Friedel oscillations in ultracold Fermi gases**
K. Riechers, K. Hueck, N. Luick, T. Lompe, H. Moritz
 The European Physical Journal D **71**, 232 (2017)
- **Probing superfluidity of Bose-Einstein condensates via laser stirring**
V. P. Singh, W. Weimer, K. Morgener, J. Siegl, K. Hueck, N. Luick, H. Moritz, L. Mathey
 Physical Review A **93**, 023634 (2016)

Part I

EXPERIMENTAL SETUP AND METHODS

3

FUNDAMENTALS OF ULTRACOLD 2D FERMİ GASES

In this chapter, I provide a brief overview over the basic two-body and many-body properties of ultracold 2D Fermi gases. For a more detailed description, I recommend the review articles on 2D Fermi gases by Levinsen and Parish [72, 80] and Turlapov and Kagan [80], as well as a review on 2D Bose gases by Hadzibabic and Dalibard [81] for an excellent introduction to BKT physics.

Reducing the dimensionality of a 3D Fermi gas to 2D has a profound impact on fundamental aspects of the BEC-BCS crossover. On a two-body level, the strongly confined geometry leads to a significant modification of scattering between particles. On a many-body level, the reduced dimensionality leads to an enhancement of phase fluctuations and 2D superfluidity exists despite the absence of long-range phase coherence as explained by BKT theory. This combination makes strongly correlated 2D superfluids a fascinating yet challenging system to understand.

3.1 Two-body scattering properties

3.1.1 The interaction parameter

For an ultracold 3D Fermi gas, interactions between particles can be parametrised by a single s-wave scattering length a_{3D} .⁵ Using a Feshbach resonance, a_{3D} and hence the 3D coupling parameter $g_{3D} = 4\pi\hbar^2 a_{3D}/m$ can be widely tuned to realise systems ranging from attractive Fermi gases ($a_{3D} < 0$) to repulsive Bose gases ($a_{3D} > 0$). The transition between the two regimes is marked by a diverging $a_{3D} \rightarrow \pm\infty$ in the unitary regime, where a two-body bound state with binding energy $E_{B,3D} = \hbar^2/(ma_{3D}^2)$ enters the system and enables the formation of bosonic dimers for $a_{3D} > 0$.

When the dimensionality of the Fermi gas is reduced to 2D, these scattering properties are significantly modified. Commonly, such ultracold 2D Fermi gases can be realized by trapping fermions in strongly anisotropic potentials, whose energy level spacing $\hbar\omega_z$ in the strongly confined direction exceeds all energy scales of the gas such as its chemical potential μ and temperature T (s. Fig. 3.1). While microscopically interactions in such a system are still 3D, it can be shown [83] that for $\hbar\omega_z \gg \mu, k_B T$ such a system is well-described as a quasi-2D⁶ system with an effective 2D scattering length⁷

$$a_{2D} = l_z \sqrt{\frac{\pi}{A}} e^{-\sqrt{\frac{\pi}{2}} \frac{l_z}{a_{3D}}}, \quad (3.1)$$

determined by both a_{3D} and the harmonic oscillator length $l_z = \sqrt{\hbar/m\omega_z}$ as an additional length scale. This value for a_{2D} yields the dimen-

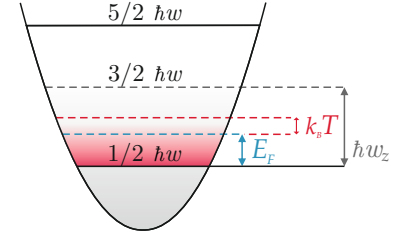


Figure 3.1: Criteria for the quasi-2D regime. Quasi-2D gases can be realised with ultracold atoms by trapping the gas in a strongly confining potential whose oscillator spacing $\hbar\omega_z$ exceeds all relevant energy scales of the system set by the Fermi energy E_F , chemical potential μ and temperature T . Adapted from [82].

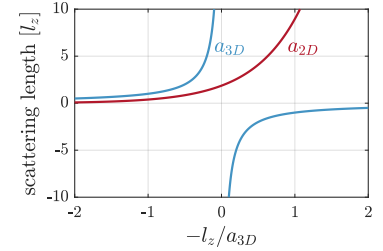


Figure 3.2: Comparing the scattering length in 2D and 3D. While the 3D scattering length a_{3D} diverges and changes sign at unitarity, the 2D scattering length a_{2D} always remains positive.

⁵ For a detailed description of the 3D BEC-BCS crossover see [49].

⁶ In the original work by Petrov and Shlyapnikov [83] the quasi-2D regime is defined for two-body scattering processes of harmonically trapped particles with a relative momentum k well below the oscillator length l_z , i.e. $kl_z \ll 1$. In contrast, recent experimental works extend the use of the term to scattering between particles that also occupy higher transverse states [75].

⁷ Note, that there exists an alternative definition of the 2D scattering length $a_2 = a_{2D} 2e^{-\gamma_E} \approx 1.12a_{2D}$ which is used e.g. in [80], where $\gamma_E = 0.577$.

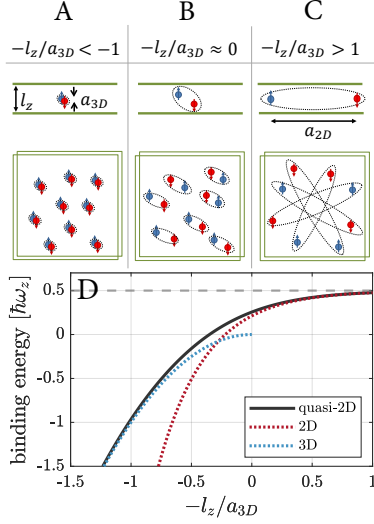


Figure 3.3: Confinement induced bound state and binding energy. (A–C) The size d of the two-body bound state in a strongly confining potential (green lines) increases continuously from (A) $d \sim a_{3D} \ll l_z$ far in the bosonic limit, to (B) $d \sim l_z$ at unitarity, to (C) $d \sim a_{2D} \gg l_z$ far in the BCS limit. (D) The corresponding binding energy E_B of the quasi-2D bound state is obtained from eq. 3.4 which can be approximated by $E_B \approx \hbar^2/(ma_{3D}^2)$ far in the bosonic limit and $E_B \approx \hbar^2/(ma_{2D}^2)$ far in the BCS limit. For the 2D and quasi-2D binding energy an energy offset of $\hbar\omega_z/2$ was added to account for the ground state energy of the confinement potential.

⁸ In the bosonic limit, we can use eq. 3.2 to map our system to a bosonic theory by replacing l_z with the harmonic oscillator length for dimers $l_{z,d} = \sqrt{\hbar/2m\omega_z}$ and a_{3D} with the effective scattering length $a_{3D,d} = 0.6a_{3D}$ for dimer-dimer scattering [84].

⁹ For a 3D system, pairing for $a_{3D} < 0$ can only occur as the result of many-body Cooper pairs which require the presence of a Fermi surface.

¹⁰ As described in [85] we expect corrections to eq. 3.4 due to the finite range of interactions between particles which can be accounted for by replacing $l_z/a_{3D} \rightarrow l_z/a_{3D} + \frac{r_{\text{eff}}}{2l_z} \left(\frac{E_B}{\hbar\omega_z} - \frac{1}{2} \right)$ in eq. 3.4, where r_{eff} is the effective range of interactions.

sionless interaction parameter $\ln(k_F a_{2D})$ which replaces the parameter $1/k_F a_{3D}$ commonly used to parametrise interactions in 3D systems.

While for 3D systems at unitarity $k_F a_{3D} \rightarrow \infty$, for 2D systems the strongly correlated regime occurs for $k_F a_{2D} = 1$ when the size $\sim a_{2D}$ of the two-body bound state is on the order of the interparticle distance $\sim 1/k_F$. Therefore, in contrast to the 3D case, one can tune between the bosonic limit ($k_F a_{2D} \ll 1$) and the fermionic limit ($k_F a_{2D} \gg 1$) also by changing the density of the system. The coupling constant in these regimes is given by

$$g_{2D} = -\frac{\hbar^2}{m} \frac{2\pi}{\ln(k_F a_{2D})}, \quad (3.2)$$

which similarly to the 3D coupling parameter describes repulsive interactions ($g_{2D} > 0$) in the bosonic limit⁸ and attractive interactions ($g_{2D} < 0$) in the fermionic limit. In the weakly-interacting limit of $|a_{3D}| \ll l_z$, eq. 3.2 further reduces to

$$g_{2D} \approx \frac{\hbar^2}{m} \sqrt{8\pi} \frac{a_{3D}}{l_z}, \quad (3.3)$$

which can be recast as the dimensionless coupling constant $\tilde{g} = mg_{2D}/\hbar^2$ commonly used to describe weakly interacting 2D Bose gases [81].

3.1.2 Crossover from 3D dimers to confinement induced bound states

The reduced dimensionality has a profound impact on the origin of pairing between fermions, which is of central importance for fermionic superfluidity. In sharp contrast to the 3D case⁹, in 2D there exists a two-body bound state for arbitrary interaction strength. The nature of this bound state and hence its binding energy E_B is determined by the size d of the pair compared to the characteristic length of the confinement l_z .

Far in the bosonic limit ($l_z/a_{3D} \gg 1$), the average dimer size $d \ll l_z$ is much smaller than the harmonic oscillator length and the nature of the bound state is 3D. In this limit, the binding energy is not affected by the confinement and approaches the 3D value of $E_{B,3D} = \hbar^2/(ma_{3D}^2)$ (s. Fig. 3.3). As the size of dimers increases, the influence of the confinement becomes more dominant and reaches a universal value $E_B \approx 0.244\hbar\omega_z$ in the strong coupling regime, where $a_{3D} \rightarrow \infty$ [72]. Eventually, for negative values of a_{3D} the two-body bound state can only exist due to the presence of the confinement and far in the BCS limit the binding energy can be approximated by $E_B \approx \hbar^2/(ma_{2D}^2)$. For arbitrary interaction strength¹⁰, the binding energy can be calculated following [44] using

$$\frac{l_z}{a_{3D}} = \mathcal{F} \left(\frac{E_B}{\hbar\omega_z} \right), \quad (3.4)$$

where

$$\mathcal{F}(x) = \int_0^\infty \frac{du}{\sqrt{4\pi u^3}} \left(1 - \frac{e^{-xu}}{\sqrt{(1 - e^{-2u})/2u}} \right). \quad (3.5)$$

However, as described above this binding energy obtained from eq. 3.4 is generally not a good parameter to quantify the 2D scattering length according to $E_B = \hbar^2 / (ma_{2D}^2)$. In particular, far in the bosonic regime this approach would yield $a_{2D} \sim a_{3D}$, which is much larger than the exponentially suppressed actual 2D scattering length a_{2D} between particles and thus significantly overestimates the mean field contribution as already pointed out in [80].

Extra 3.1: Derivation of the 2D scattering length

The common approach to derive the 2D scattering length for a 2D quantum gas is to equate the scattering amplitudes of a pure 2D system [80]

$$f_{2D}(k, a_{2D}) = \frac{4\pi}{-\ln(k^2 a_{2D}^2) + i\pi} \quad (3.6)$$

with the quasi-2D scattering amplitude f_{q2D} of a 3D gas in a geometry with a strong confinement along the z-axis. In their pioneering work, Petrov and Shlyapnikov [83] showed that for scattering processes that remain in the vertical ground state the quasi-2D scattering amplitude is given by

$$f_{q2D}(k, a_{3D}, l_z) = \frac{4\pi}{\sqrt{2\pi} l_z / a_{3D} + w(k^2 l_z^2 / 2)}, \quad (3.7)$$

where $w(\xi)$ is defined in [80, 83] and shown in Fig. 3.4. For small relative momenta k of colliding particles, we can approximate

$$w\left(\frac{k^2 l_z^2}{2}\right) \approx w_{\text{lim}}\left(\frac{k^2 l_z^2}{2}\right) \equiv -\ln\left(\frac{2\pi}{A} \frac{k^2 l_z^2}{2}\right) + i\pi \quad (3.8)$$

and get

$$a_{2D} = l_z \sqrt{\frac{\pi}{A}} e^{-\sqrt{\pi/2} l_z / a_{3D}}, \quad (3.9)$$

where $A \approx 0.905$.

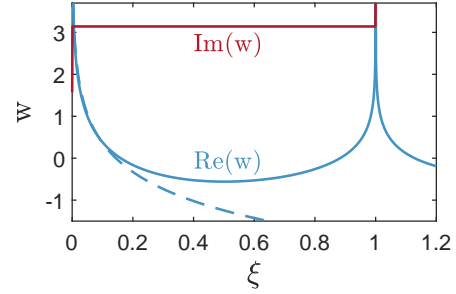


Figure 3.4: Plot of the function $w(\xi)$ introduced in [83] to describe scattering in quasi-2D geometries. For $\xi < 0.1$, the real part of w is well approximated by $\text{Re}(w) \approx -\ln\left(\frac{2\pi}{A} \frac{k^2 l_z^2}{2}\right)$ (blue dashed line).

Extra 3.2: Parametrising interactions in the strongly correlated 2D regime

Since for an interacting 2D Fermi gas the characteristic momentum k of interacting particles can reach up to k_F , the approximation made to obtain eq. 3.9 is generally not accurate. Following the approach in [74, 75], eq. 3.9 acquires a momentum dependent correction

$$a_{2D,k} = a_{2D} e^{-\frac{1}{2} \Delta w(k^2 l_z^2 / 2)}, \quad (3.10)$$

determined by the deviation $\Delta w = w - w_{\text{lim}}$. To calculate $a_{2D,k}$, eq. 3.10 is evaluated for a characteristic momentum $k_\mu = \sqrt{2m\mu}/\hbar$ for collisions between particles determined by the chemical potential μ . While this approach should be accurate

for zero temperature far on the BCS side where interactions between particles are restricted to the Fermi surface, we expect this approach to fail in the strongly correlated regime and at higher temperatures. So far, it seems unlikely that a universal interaction parameter exists for this strongly correlated 2D regime. While recently, a strong coupling theory for 2D fermions was developed which adds a second parameter - a confinement-induced effective range - to parametrise the momentum dependence of the scattering to first order [86, 87], further experimental work is needed to test their model [88].

3.2 Superfluidity in a 2D Fermi gas

For sufficiently low temperatures, an interacting Fermi gas can become a superfluid - a striking state of matter in which particles can collectively flow through the system without any friction. In this section, I will briefly explain how the nature of such superfluids depends on the dimensionality of the system.

3.2.1 Overview of the BKT transition

For a 3D Fermi gas, the phase transition to a superfluid is directly linked to the onset of long-range phase coherence, which means that the phase ϕ of the superfluid order parameter Ψ remains correlated throughout the whole system. Hence, for such a 3D superfluid the first order correlation function

$$g_1(\mathbf{r}, \mathbf{r}') = \langle \Psi^\dagger(\mathbf{r})\Psi(\mathbf{r}') \rangle \quad (3.11)$$

remains non-zero even for points \mathbf{r} and \mathbf{r}' in the superfluid which are separated by an arbitrarily large distance $r = |\mathbf{r} - \mathbf{r}'|$.

When the dimensionality is reduced to 2D, thermal phase fluctuations in the form of phonons and vortices become more pronounced and thereby prevent such long-range phase coherence for any non-zero temperature [11, 12]. However, despite this absence of true long-range order a 2D Fermi gas can still become a superfluid. As explained by the seminal BKT theory [13, 14], the mechanism that enables the existence of superfluidity in 2D is the formation of vortex-antivortex pairs, which bind for sufficiently low temperatures $0 < T < T_{\text{BKT}}$ and thereby significantly suppress long-range phase fluctuations. The characteristic feature of such a 2D superfluid is an algebraic decay of phase coherence

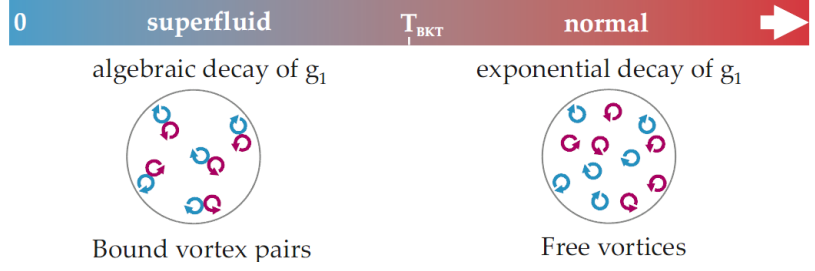
$$g_1(r) \propto (1/r)^\eta, \quad (3.12)$$

where the decay exponent $\eta = 1/n_s \lambda_{\text{dB}}^2$ is determined by the superfluid density n_s and the thermal de-Broglie wavelength $\lambda_{\text{dB}} = \frac{2\pi\hbar}{\sqrt{2\pi m k_B T}}$. While in sharp contrast to a 3D superfluid $g_1(r)$ approaches zero for large distances r , this algebraic decay is generally very weak since the maximal scaling exponent is limited by BKT theory to $\eta \leq 1/4$. Hence, 2D superfluids are commonly associated with *quasi*-long-range order. As the temperature of the superfluid is increased, the number of thermally activated vortex-antivortex pairs increases which reduces n_s . Remarkably, at the critical temperature T_{BKT} for the BKT transition the superfluid density suddenly jumps from a universal value of $n_s = 4/\lambda_{\text{dB}}^2$ to zero [89].¹¹ Above this critical temperature, vortex-antivortex pairs start to unbind and the proliferation of free vortices leads to a fast exponential decay¹² of $g_1 \propto e^{-r/l}$.

¹¹ This characteristic jump of the superfluid density at the BKT transition can be quantitatively understood from a renormalisation group analysis. This analysis shows that for any temperature $T > T_{\text{BKT}}$ the RG flow equations for the superfluid density go to zero in the limit of large distances.

¹² The length scale of this exponential decay is given by $l = \lambda_{\text{dB}} \exp\left(\sqrt{\frac{a T_{\text{BKT}}}{T - T_{\text{BKT}}}}\right)$ with a model-dependent dimensionless constant a [81].

Figure 3.5: The BKT transition to a 2D superfluid. Below the critical temperature T_{BKT} for 2D superfluidity, vortex-antivortex pairs are formed and phase correlations decay algebraically $g_1(r) \propto (1/r)^\eta$ with a characteristic scaling exponent $\eta = 1/n_s \lambda_{\text{dB}}^2$ determined by the superfluid density n_s . For $T > T_{\text{BKT}}$, vortex pairs unbind and phase correlations decay exponentially $g_1(r) \propto e^{-r/l}$ on a length scale l determined by λ_{dB} [81]. Adapted from [82].



3.2.2 The critical temperature

BKT theory is generally expected to describe superfluidity in 2D Fermi gases in the entire crossover from deeply bound molecules to weakly bound Cooper pairs [72, 78]. Making a quantitative prediction for the critical temperature T_c/T_F , however, is generally a very challenging task. While BKT theory yields a universal value of the superfluid density $n_s \lambda_{\text{dB}}^2 = 4$ at the critical point, the corresponding total density n is not explicitly specified. Far in the bosonic limit, we can use the numerical result from a classical field Monte-Carlo simulation for a weakly interacting 2D Bose gas [90] which predicts

$$n \lambda_{\text{dB,d}}^2 \approx \ln(380/\tilde{g}) \quad (3.13)$$

which can be recast [62, 72] as

$$T_c/T_F = \frac{1}{2} \left[\ln \left(\frac{380}{4\pi} \ln \left(\frac{4\pi}{k_F^2 a_{2D}^2} \right) \right) \right]^{-1}, \quad (3.14)$$

where we used $T_c/T_F = \frac{1}{2} \frac{1}{n \lambda_{\text{dB,d}}^2}$ and eq. 3.2 (s. Fig.3.6).¹³

Far in the fermionic limit, the critical temperature for superfluidity is determined by the energy required to break pairs and can therefore be determined from the temperature T at which the superfluid gap Δ vanishes [72]. Using this approach, a simple approximation for T_c was obtained from the mean-field BCS Hamiltonian which yields $T_c/T_F = 2e^{\gamma_E}/\pi k_F a_{2D}$, where $\gamma_E = 0.577$ [91]. More recently, this prediction was extended in [62] up to second order in perturbation theory which yields

$$\frac{T_c}{T_F} = \frac{2e^{\gamma-1}}{\pi k_F a_{2D}}. \quad (3.15)$$

Making a quantitative prediction for the critical temperature in the intermediate strong coupling regime is still an active area of research.¹⁴ Therefore, we show in Fig. 3.6 a simple interpolation between the well-established results of eq. 3.14 and eq. 3.15 which suggests a maximum of T_c/T_F in the regime of $\ln(k_F a_{2D}) \approx 1$.

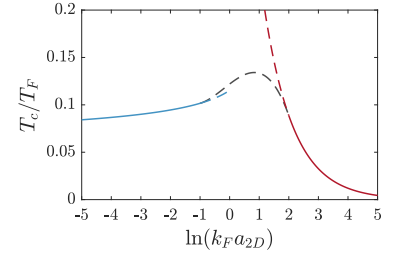


Figure 3.6: Critical temperature for superfluidity in a 2D Fermi gas. In the bosonic limit ($\ln(k_F a_{2D}) < -1$) the critical temperature is calculated using eq. 3.14 which is obtained from a classical field Monte-Carlo simulation [90] (blue line). In the fermionic limit ($\ln(k_F a_{2D}) > 2$) the critical temperature is calculated using eq. 3.15 obtained from the Thouless criterion including Gorkov–Melik-Barkhudarov corrections as derived in [62] (red line). We use a cubic interpolation between the bosonic and the fermionic regime to obtain an estimate for T_c/T_F in the regime of $(-1 > \ln(k_F a_{2D}) < 2)$ (grey dashed line).

¹³ The factor of 1/2 originates from the definition of the Fermi temperature T_F in terms of the single fermion mass m , while the thermal wavelength $\lambda_{\text{dB,d}} = \lambda_{\text{dB}}/\sqrt{2}$ is defined for the dimer mass $M = 2m$.

¹⁴ Very recently, results for T_c/T_F in the strong coupling regime were obtained using a Gaussian pair fluctuation theory [92].

4

EXPERIMENTAL APPARATUS AND UPGRADES

In this chapter, I provide an overview of our experimental apparatus to create ultracold 2D Fermi gases.¹⁵ Particular focus is put on the improvements of our resonator cooling scheme and our vacuum system which we conducted during the initial years of my work as a PhD student. These improvements eventually enabled us to achieve sufficiently low temperatures for 2D superfluidity and significantly improved the reproducibility of our experiment and thereby formed the basis for the realisation of a Josephson junction in our 2D Fermi gas as described in detail in part III of this thesis.

¹⁵ For more details of the experiment see previous PhD theses [82, 93–95].

Outline of the experiment

The goal of our experiment is the creation of ultracold 2D Fermi gases to realise a versatile platform for the study of low-dimensional strongly correlated quantum matter in a clean and well-controlled environment. In this endeavour, we perform our experiments with fermionic ${}^6\text{Li}$ whose broad Feshbach resonance enables both fast thermalisation rates for efficient evaporative cooling as well as a widely tunable interaction strength in the strongly correlated regime. We employ a sequence of laser cooling and evaporative cooling steps to reach temperatures on the order of $T/T_F \approx 0.03$, which is well below the critical temperature for 2D superfluidity [62, 72]. At the same time, we optically transport the atoms to a glass vacuum chamber for optimal optical access and subsequently bring our gas into the 2D regime by compressing it in a sequence of optical dipole traps. Finally, we use two high-resolution microscope objectives to both project additional potentials and image our ultracold 2D Fermi gas with a resolution on the order of the interparticle distance. This system offers a very high degree of control over the preparation and characterisation of quantum many body states which we utilized to realise the first homogeneous 2D Fermi gas [96] and the first Josephson junction in an ultracold 2D quantum gas [97] as described in part II and III.

4.1 Overview of the experimental sequence

Our experimental cycle to create an ultracold 2D Fermi gas takes about 10 s and involves a sequence of preparation steps in which ${}^6\text{Li}$ atoms are cooled to quantum degeneracy and simultaneously brought to the 2D regime by applying a sequence of tailored optical traps (s. Fig. 4.1). This whole preparation is performed inside multiple connected ultra-high vacuum chambers at a pressure of $\sim 1 \times 10^{-11}$ mbar to minimise the collision rate with room-temperature background atoms, which would limit the atomic lifetime and achievable temperature of our system.

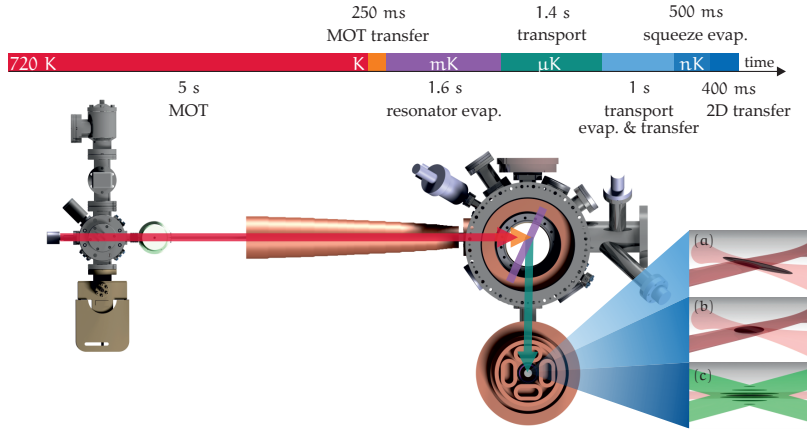


Figure 4.1: **Overview of the experimental cycle to create an ultracold 2D Fermi gas.** (**red arrow**) Fermionic ${}^6\text{Li}$ atoms are ejected from the oven, decelerated in a Zeeman slower and captured in a 3D MOT. After loading the MOT for about 5 s, we shift the MOT (orange arrow) to transfer atoms to a deep optical dipole trap created by the standing wave of two counterpropagating far detuned ($\lambda = 1064\text{ nm}$) beams inside a high-finesse cavity (purple). After evaporative cooling in this resonator (s. Fig. 4.2 for more details), the gas is loaded into a far-off-resonant trap (FORT) which is focussed to the resonator waist. (**green arrow**) By moving the focus position of the FORT the gas is transported to the science chamber, where we apply magnetic offset fields of $B \approx 830\text{ G}$ close to the Feshbach resonance of ${}^6\text{Li}$ to perform efficient evaporative cooling. Finally, we create a two-dimensional system by squeezing the gas in a highly elliptical optical trap (a,b) and transferring the gas into a single layer of a repulsive ($\lambda = 532\text{ nm}$) 1D optical lattice (c). Adapted from [82].

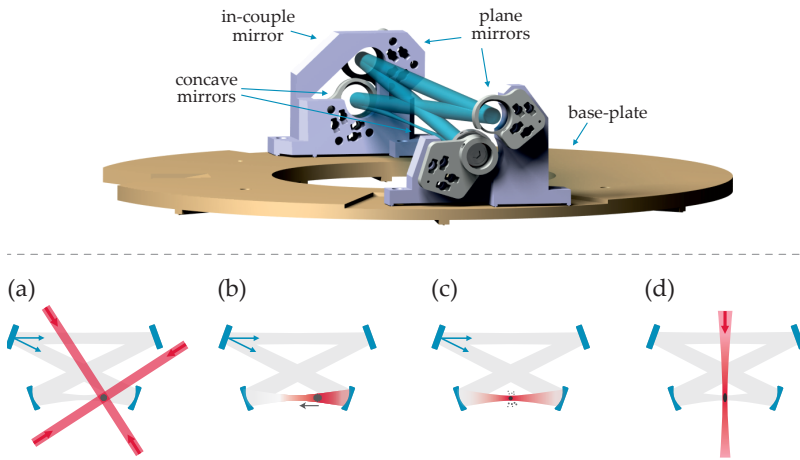


Figure 4.2: **The cooling resonator.** (**top panel**) CAD model of the in vacuo cooling resonator. (**bottom panel**) Details of the updated resonator loading scheme. (a) We load atoms from the MOT (red beams) into the standing wave of the resonator (grey) by shifting the MOT to a position about 3 cm from the focal plane of the TEM_{00} mode, where the increased radial waist of about $200\text{--}300\mu\text{m}$ ensures a high transfer efficiency. (b) We detune the secondary beam by a fixed frequency offset of $\Delta\nu_{\text{AOM}} = 200\text{ kHz}$, which moves the standing wave at a velocity $v = \lambda\Delta\nu_{\text{AOM}} \approx 0.2\text{ m/s}$ and transports the atoms within $\sim 137.5\text{ ms}$ to the focus of the resonator mode. (c) We switch off the secondary beam completely and evaporatively cool the gas in this running wave trap at an magnetic offset field of 300 G by ramping down the power of the primary beam by a factor of ~ 100 . (d) At the end of this evaporation the atoms are trapped inside the FORT (red beam) and transported to the science chamber. Adapted from [82] with minor modifications to account for the updated cooling protocol.

Oven - Zeemanslower - 3D MOT

For the first part of our experiment, we employ a conventional combination of a Zeeman slower and a 3D MOT.¹⁶ Our atom source is provided by ~ 1 g of ${}^6\text{Li}$ with an isotopic purity of about 95 % which is placed inside our oven chamber and heated to a temperature of ~ 400 °C. At this temperature, the solid lithium is melted and produces the required vapour pressure for a sufficient atom flow ejected from the oven chamber [99]. To increase the number of atoms within the capture range of our 3D MOT, we use a decreasing-field Zeeman slower, which connects the oven chamber and the MOT chamber and reduces the velocity of atoms from an initial mean value of about $v_{\text{th}} \approx 1000$ m/s. After loading the MOT for about 5 s, we accumulate about $\sim 1 \times 10^8$ atoms at a temperature somewhat above the Doppler temperature $T_D \approx 140$ μK , which is limited by the scattering rate $\Gamma \approx 2\pi \times 6$ MHz of the addressed D2 transition (s. Fig. 4.3).

The cooling resonator

Next, the atoms are transferred to a series of far detuned ($\lambda = 1064$ nm) optical dipole traps, which have a significantly lower photon scattering rate Γ than the resonant MOT beams and thereby enable an efficient evaporative cooling to reach quantum degeneracy. While this large frequency detuning Δ significantly reduces the scattering rate $\Gamma \propto I/\Delta^2$, it also requires higher optical intensities I for the same trap depth $U \propto I/\Delta$. In principle, sufficient trap depths of ~ 1 mK necessary to directly load atoms from our MOT can be achieved using a high-power ~ 200 W laser which is focused down to sufficiently small spot sizes to increase the intensity.¹⁷ However, such a small spot size also implies a small overlap of the dipole trap with the MOT and hence a reduced transfer efficiency.

To solve these issues, our experiment features a novel high-finesse in vacuo resonator which enhances the intensity experienced by atoms by a factor of ~ 1000 and thereby eliminates the need for high power lasers and enables high trap volumes for an optimal transfer efficiency from the MOT.¹⁸ The cooling resonator was originally designed and implemented in [93, 104] and consists of two counterpropagating laser beams ($\lambda = 1064$ nm) which form a standing wave in the TEM₀₀ mode between two curved mirrors, where atoms are trapped, transported and cooled (s. Fig. 4.2). To achieve a high trap overlap for an optimal transfer efficiency, we first load the atoms ~ 3 cm off-center from the waist of the resonator where the trap volume is larger. Finally, we detune one of the laser beams to shift the lattice pattern and transport atoms to the waist position, where we switch off one of the beams and evaporatively cool the gas in a running wave trap.¹⁹

¹⁶ For more details on laser cooling and trapping see [98].

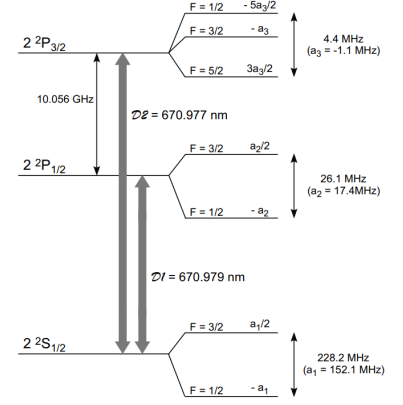


Figure 4.3: Level diagram of the D1 and D2 transition in ${}^6\text{Li}$. Adapted from [99].

¹⁷ see e.g. experiments with ultracold ${}^6\text{Li}$ in the groups of Selim Jochim [100], Markus Greiner [101] or Waseem Bakr [102].

¹⁸ A similar cooling resonator scheme is used in [103], which consists of a single retroreflected laser beam and therefore does not enable atom transport to the beam focus as implemented in our setup.

¹⁹ Due to large heating rates during the transport, evaporative cooling was previously performed at the loading position. During the course of this thesis, we performed upgrades to the cooling resonator setup (s. section 4.3) which solved this issue and enabled the successful implementation of the originally intended protocol described in [93].

Transport to the science chamber

Manipulating and imaging our Fermi gas with a high resolution on the order of the interparticle distance $\sim 1 \mu\text{m}$ requires the use of high-NA microscope objectives which generally have to be placed as close to the atoms as possible. Furthermore, to utilize the broad Feshbach resonance of ${}^6\text{Li}$ for both efficient evaporative cooling and a tunable interaction strength in the strongly correlated regime, we need to create high magnetic offset fields on the order of $B \approx 1000 \text{ G}$, which is simplified by bringing electromagnetic coils close to the atoms. We achieve these requirements by transporting the gas from the MOT chamber into a separate science chamber²⁰, which offers excellent optical access for our experiments and enables bringing the coils and microscope objectives close to the gas.

For the transport, we load the gas after evaporation inside the resonator into a tightly focused ($w_{x,y} \approx 25 \mu\text{m}$)²¹ conventional far-off-resonant trap ($\lambda = 1064 \text{ nm}$), which due to the pre-cooling only requires a moderate beam power of 4 W to transfer $\sim 1 \times 10^6$ atoms into the trap. For the transport, we use a lens mounted on a translation stage to move the focus of the FORT and thereby transport the gas from the center of the resonator mode to the heart of our experiment: the science chamber.

Science chamber

In the science chamber, we perform the last experimental steps to prepare, manipulate and image 2D fermionic superfluids. To reach the 2D regime, we first transfer the gas from the FORT to a highly elliptical²² attractive ($\lambda = 1064 \text{ nm}$) *squeeze trap*. By increasing the power of the squeeze trap to $\sim 1 \text{ W}$ we compress the gas along the strongly-confined direction to $\sim 1 \mu\text{m}$ which finally enables us to load the gas into a single layer of a strongly confining repulsive 1D optical lattice. In this lattice, we achieve a maximal trap frequency along the z direction of $\omega_z \approx 2\pi \times 12 \text{ kHz}$ which exceeds the typical energy scales of our gas set by its temperature T and chemical potential μ and therefore enables us to realize a 2D Fermi gas.²³ During these preparation steps, we apply magnetic offset fields around $B \approx 830 \text{ G}$ close to the Feshbach resonance of ${}^6\text{Li}$ to perform efficient further evaporative cooling inside the FORT and squeeze trap and thereby reach temperatures of our 2D gas on the order of $T/T_F \approx 0.03$, which is well below the predicted critical temperature for 2D superfluidity[62]. Finally, we use two high-resolution ($\text{NA} = 0.62$) microscope objectives placed directly above and below the upper and lower windows of the glass cell to both project arbitrary potentials and image the gas with a resolution on the order of the interparticle distance (s. Fig. 4.4).

²⁰ We replaced the previously used metal chamber with a glass cell (s. section 4.2). This profound change in our vacuum setup significantly improved our single particle lifetime and enabled the creation of 2D Fermi gases with a temperature well below the critical temperature for 2D superfluidity.

²¹ In this thesis, Gaussian beam waists w denote the $1/e^2$ radius of the intensity.

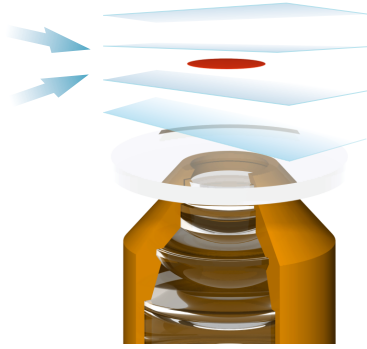


Figure 4.4: High-resolution probing of a 2D Fermi gas The 1D lattice (light blue) is formed by interfering two elliptical [$w_y \times w_z \approx (400 \times 40) \mu\text{m}$] $\lambda = 532 \text{ nm}$ beams which intersect with an opening angle of 10.4° and thereby create a lattice with a spacing of $2.9 \mu\text{m}$. We load the gas (red) into a single layer of this lattice to bring it into the 2D regime and use two microscope objectives (only lower objective is shown) to manipulate and image the gas with a high resolution. Adapted from [82].

²² aspect ratio of the squeeze trap: $w_y \times w_z \approx (400 \times 10) \mu\text{m}$

²³ More details on the creation manipulation and detection techniques for our ultracold 2D Fermi gases are given in chapter 5.

4.2 Replacing the metal science cell by a glass cell

A basic requirement for experiments with ultracold atom experiments is the realisation of an ultra-high vacuum with a typical pressure on the order of 1×10^{-11} mbar to minimise the probability of collisions with the background gas. Well after the initial construction of our experiment we realized that this requirement was not met for our science chamber. Measurements of the single particle lifetime²⁴ τ showed that the pressure inside the science chamber ($\tau \approx 8$ s) was increased by almost a factor of 20 compared to the pressure inside the MOT chamber ($\tau \approx 160$ s) (s. Fig. 4.6). Remarkably, we also observed that this reduced lifetime was accompanied by a significantly increased heating rate of gases with strong interactions. In particular, we found that the lifetime of molecular condensates was an order of magnitude smaller than the corresponding single particle lifetime and thereby posed a major limitation on the minimal achievable temperatures in our experiment [95].

To find the origin for the insufficient vacuum in our science chamber, we first ruled out the possibility of a leak in our metal chamber by performing helium leak testing. Eventually, we concluded that the poor vacuum in our science chamber was caused by an insufficient pumping rate for our metal chamber due to the narrow CF16 connection to the MOT chamber and substantially higher outgassing rates than expected.²⁵

To solve this issue, we replaced the metal cell with a glass cell which is expected to have a significantly lower outgassing rate compared to the metal chamber. After this replacement, we observed a significant increase of the single-particle lifetime to $\tau = (126 \pm 12)$ s which is comparable to the lifetime in the MOT chamber (s. Fig. 4.6). Eventually, this improvement of our vacuum in the science chamber reduced the previously observed heating rates and thereby enabled us to reach sufficiently low temperatures for 2D superfluidity required for the realisation of a Josephson junction as described in part III.

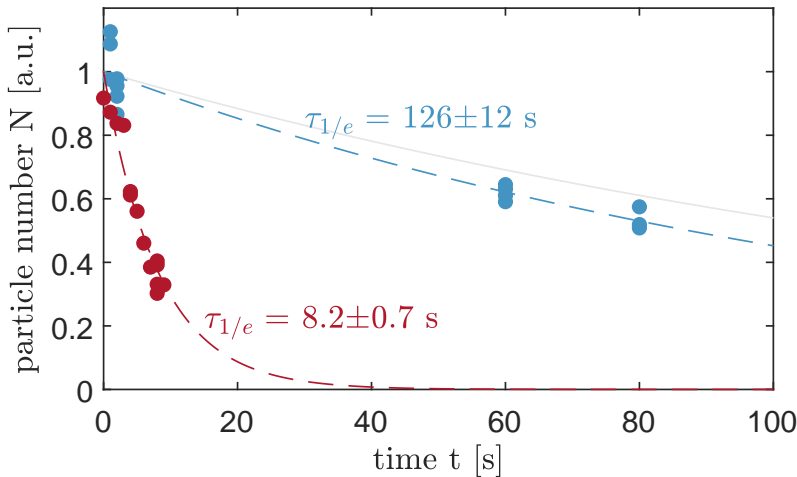


Figure 4.5: The new glass science cell. Shown is the glass cell after integration into the experiment after the surrounding coils and breadboards were reinstalled. The paper sheet was used to align the pilot beam which is both central and orthogonal to both upper and lower glass cell windows and is used for the subsequent microscope alignment.

²⁴ A measure for the pressure $P \propto 1/\tau$ inside an ultra high vacuum system is the single-particle lifetime τ [105], which quantifies the loss in atom number $N(t) = N_0 e^{-t/\tau}$ due to collisions with the background gas.

²⁵ The surface outgassing rate of untreated steel of 1×10^{-10} mbar L/(s cm²) for our metal chamber with an area of ~ 10 cm² yields a total outgassing rate of 10×10^{-9} mbar L/s. Since the area of the CF16 tube limits the pumping rate to ~ 10 L/s we would expect a pressure in our previously used metal chamber of $\sim 10 \times 10^{-10}$ mbar. However, the metal chamber was baked under vacuum at $\sim 150^\circ$, so the outgassing rate should be lower than for untreated steel. Similar observations were made in the group of Silke Ospelkaus [106].

Figure 4.6: Improved single-particle lifetime after replacing the metal cell with a glass cell. To measure the single-particle lifetime $\tau_{1/e}$ we prepare a non-interacting Fermi gas at a magnetic offset field of 530 G, measure the particle number N after holding the gas for varying times t in an optical trap and fit the decay in the particle number with an exponential function $N \propto \exp(-t/\tau_{1/e})$ (dashed lines). We observe a lifetime of $\tau_{1/e} = (126 \pm 12)$ s in the glass cell (blue dots) which is greatly increased from the lifetime of $\tau_{1/e} = (8.2 \pm 0.7)$ s in the previously used metal cell (red dots). For comparison, we show the decay in particle number inside the MOT chamber with a fitted lifetime of (162 ± 18) s (light grey line). The provided error values denote the 1σ fit error.

²⁶ For more details on the cooling resonator see [79, 93].

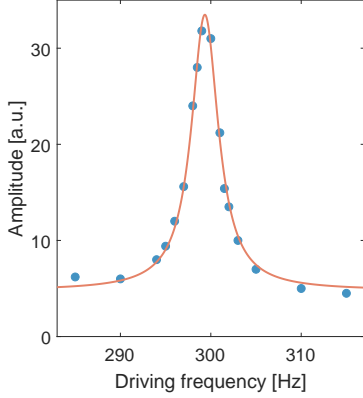


Figure 4.7: Mechanical resonance of the resonator cavity. We acoustically drive the resonator and measure the oscillation amplitude in the frequency of the transmission resonance. Using a Lorentzian fit we determine a resonance frequency of $\nu_{ac} = 299.3$ Hz and FWHM linewidth of $\Gamma_{ac} = 3.6$ Hz (red line).

²⁷ In principle, this stabilisation can also be done by using piezos to tune the cavity resonance to match the laser frequency, but the option to control the piezos was eliminated during the initial construction of the experiment [93].

²⁸ While for a stable cavity the PDH method can be used to reduce the linewidth of a laser and reach extremely low linewidths of 40 mHz as demonstrated in [107], the linewidth of our laser is probably increased by the PDH scheme due to the poor mechanical vibration isolation of our resonator which features a pronounced acoustic resonance at 299 Hz (s. Fig. 4.7).

²⁹ In practice, the mixing frequency ν_{mix} has an adjustable phase ϕ_{mix} to maximise the error signal amplitude. Occasionally, we observed a drift in this optimal value of the phase which is detrimental to the frequency stabilisation and needs to be adjusted.

4.3 Improving the cooling resonator setup

The cooling resonator is a central component in our experiment which enables direct optical trapping of atoms from the MOT without the need for high power lasers.²⁶ While the high finesse of the resonator enables the realisation of high trap depths at moderate laser powers, the corresponding narrow resonator linewidth of ~ 80 kHz also implies high demands on the laser frequency stabilisation. Furthermore, a stable optical setup to couple the laser into the resonator is needed for a reliable operation of the experiment.

The original cooling resonator setup did not meet our overall stability requirements which often led to undesired experimental downtime and required adjustments on a daily basis. In this section, I describe how we significantly improved the stability of the cooling resonator which now does not require manual adjustments on a timescale of several months. At the same time, we managed to implement the originally envisaged cooling scheme which was prevented in the original setup due to heating during transport inside the resonator.

4.3.1 Basic principle of the resonator

An overview of the main electrical and optical components of the cooling resonator setup is shown in Fig. 4.8. In short, this setup enables us to couple two laser beams into the resonator, and stabilize and control their respective frequency and power for loading, transport and evaporative cooling as described in the previous section.

Measuring frequency and amplitude

The basic requirement for the frequency stabilisation is to control the frequency ν of the laser to match one of the cavity resonances ν_0 well within their respective linewidth of $\Gamma \sim 80$ kHz.²⁷ We achieve this by employing a conventional Pound-Drever-Hall (PDH) stabilisation scheme.²⁸

We modulate frequency sidebands of $\nu \pm 68$ MHz onto the laser using an electro-optical modulator, measure the light reflected from one input coupler of the bow-tie cavity on a fast photodiode and mix this signal with the same frequency $\nu_{mix} = 68$ MHz to create the DC error signal $\epsilon(\nu) \propto \nu - \nu_0$ for the frequency lock (s. extra 4.1).²⁹ Additionally, we measure the power inside the cavity using two slow photodiodes to control the respective power of the two beams and implement a power threshold for the frequency lock which is needed to prevent locking to higher cavity modes.

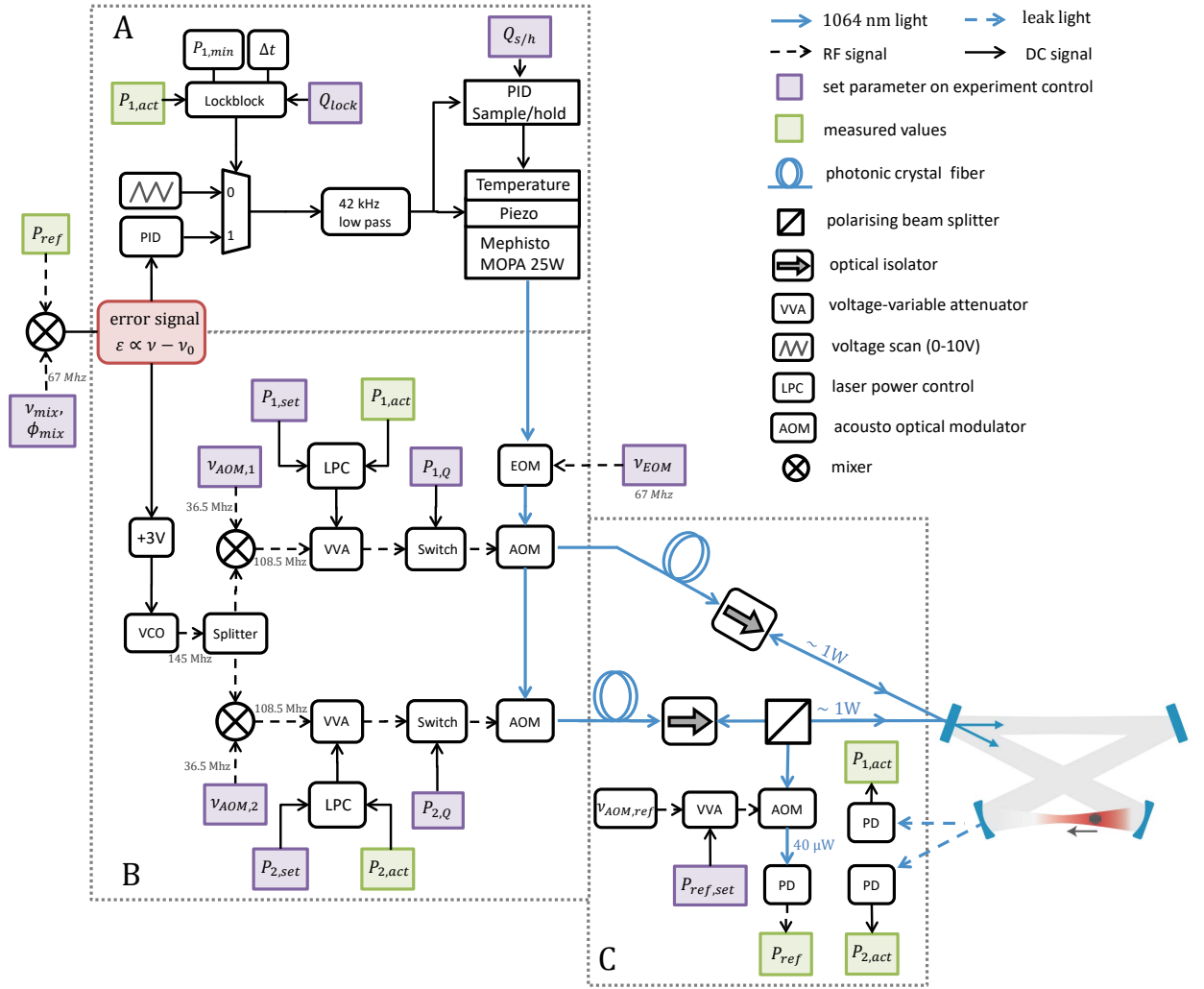


Figure 4.8: **The cooling resonator.** Complete overview of the main electrical and optical components of the cooling resonator. (A) Laser piezo and laser temperature PID loop. The laser piezo has a large frequency tuning range of ± 65 MHz with a bandwidth of ~ 100 kHz limited by piezo resonances, which require the installation of an additional low pass filter (42 kHz) for stable operation of the frequency lock. The PID is enabled for a time interval Δt when both the transmission power exceeds the set threshold $P_{1,min}$ and the lock is enabled via the control parameter Q_{lock} . The slow temperature PID loop with a bandwidth of ~ 1 Hz keeps the PID output within the center of its tuning range and is realised by a sample/hold PID which is enabled by the control parameter $Q_{s/h}$. (B) Fast AOM frequency feedback loop. An AOM in both resonator beams enables both a fast proportional frequency feedback with a bandwidth of ~ 1 MHz and a power stabilisation of the measured transmission power $P_{1,act}$ and $P_{2,act}$ to the set values of $P_{1,set}$ and $P_{2,set}$ respectively. (C) Experimental upgrade of the resonator coupling performed during the course of this thesis. The light of both resonator beams is coupled into a photonic crystal fiber and subsequently passes through an optical isolator to prevent detrimental feedback for the frequency lock. After trapping the atoms from the MOT, we introduce a frequency offset $\nu_{AOM,1} - \nu_{AOM,2} = 200$ kHz to move the atoms inside the standing wave to the waist position of the resonator mode. The power P_{ref} which measures the reflection of the primary resonator beam from the cavity to generate the error signal (s. extra 4.1) is held at a constant value of $P_{ref,set} = 40 \mu W$ to maintain a constant error signal amplitude for optimal lock performance during the subsequent evaporative cooling inside the resonator. Not shown in this illustration for better readability are RF attenuators, amplifiers, couplers and additional low-pass and high-pass filters. For more details on individual components see [79, 93].

Extra 4.1: PDH error signal generation

The light reflected from the cavity P_{ref} consists of components at the carrier frequency ν , which close to resonance enter the cavity and obtain a frequency dependent phase shift, and the sidebands $\nu \pm \delta\nu$ which get rejected since $\delta\nu > \Gamma$ exceeds the linewidth $\Gamma \approx 80$ kHz of the cavity and therefore have a constant phase shift of 180° . As shown in [108], the reflected light therefore has a beat component at the frequency $\delta\nu$

$$P_{\text{ref}} \propto \frac{\nu - \nu_0}{\Gamma} \sin(\delta\nu) \quad (4.1)$$

which is proportional to the deviation of the laser frequency from the cavity resonance. This signal is mixed with a frequency $\nu_{\text{mix}} = \delta\nu$ to generate the DC error signal $\epsilon(\nu)$.

Adjusting frequency and amplitude

We use the error signal $\epsilon(\nu)$ as a feedback in our control loop to adjust the laser frequency using three components: acousto-optical modulators, the laser piezo, and the laser temperature.

The AOMs are used for a fast proportional frequency feedback and placed in the primary and secondary beam path to add an adjustable frequency offset around 108.5 MHz to each beam in the first diffraction order. In our feedback loop, this frequency offset is controlled by using the sum of our DC error signal and a fixed voltage as the input of a fast voltage controlled oscillator³⁰ (VCO) which transforms the applied DC voltage into a variable frequency of 145 MHz which is finally mixed with a $\nu_{\text{AOM}} = 36.5$ MHz reference to match the AOM center frequency. This circuit realizes a fast proportional frequency feedback with a bandwidth of ~ 1 MHz, which is limited by delays in the AOM crystal³¹ and the bandwidth of the electrical components. This frequency feedback signal is split between the two AOMs which enables us to introduce an additional frequency offset $\Delta\nu = \nu_{\text{AOM},1} - \nu_{\text{AOM},2}$ between the two beams to translate the standing wave inside the resonator. Additionally, the power of each resonator beam can be adjusted using a voltage variable attenuator in the RF source for each AOM.

We complement the fast proportional AOM feedback by a separate PID loop in which the frequency is tuned by the laser piezo. In this piezo feedback loop, we use our error signal as input for a conventional PID controller and amplify the control output to match the voltage range of the laser piezo. Compared to the AOM feedback, this feedback loop provides a larger tuning range of ± 65 MHz at a reduced bandwidth of ~ 42 kHz limited by the response bandwidth of the laser of 100 kHz.³²

Finally, we use a slow laser temperature feedback loop on top of the laser piezo feedback to keep the frequency of the resonator mode within the tuning range of the piezo. This additional feedback layer is

³⁰ Mini-Circuits ZX95-200A+

³¹ To achieve a high feedback bandwidth of the AOM, it is crucial to have a small beam close to the RF source in the AOM crystal to minimise delays in the frequency control due to acoustic wave propagation.

³² For a stable frequency feedback it is very crucial to have a ~ 42 kHz low pass filter on the control output to suppress the piezo resonances of the laser at frequencies above the response bandwidth of 100 kHz.

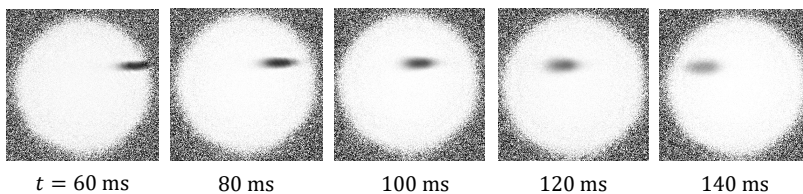
needed because the tuning range of the piezo is smaller than the free spectral range ~ 345 MHz of the cavity.

4.3.2 Redesign of the resonator coupling

In addition to the correct frequency, the spatial profile of the incoming light beam also has to match the resonator mode for a high coupling efficiency. Previously, we directly guided the diffraction of both AOMs over a distance of ~ 2 m to the incoupling mirror of the resonator, which suffered from a low coupling stability and therefore required adjustments on a regular basis. To overcome this issue, we couple the diffracted light of both AOMs into two separate fibers³³, and place the fiber output in the direct vicinity of the resonator (s. Fig. 4.8C). This approach significantly improved the stability of our setup, which does not require adjustments of the coupling on a timescale of months.

Furthermore, the fiber cleans the beam profile which greatly reduces the amount of rejected light which can be detrimental to the lock performance. To further prevent any unwanted back reflections we placed an optical isolator between the fiber outputs and the resonator. These isolators are crucial to prevent optical feedback resulting from fiber tip reflections which would interfere with the error signal and reduce the lock stability. In addition, a combination of a cleaning cube with a $\lambda/2$ wave plate can be used to adjust the polarisation of the incoming light. In contrast to the results reported in [93], we could not observe a significant dependence of the coupling efficiency on the polarisation of the incoming light.³⁴

4.3.3 Operation of the new cooling resonator scheme



Previously, the originally intended operation of the cooling resonator was prevented by a significant loss rate during transport, which was suggested to arise from parametric heating in the lattice potential [93]. The improvements of the frequency lock and the optical setup described above finally enabled us to implement this originally envisaged scheme and achieve a stable operation of the resonator without a single failed preparation in ~ 10000 cycles corresponding to 2 days.

At the beginning of a typical experimental cycle, we lock the resonator within ~ 1 s during the loading of the MOT.

To achieve a high fidelity of this locking process, it is crucial to have a *lock block*, which enables the frequency stabilisation only for

³³ We use photonic crystal fibers which are very well suited to handle a beam power on the order of a few watt at wavelengths of 1064 nm.

³⁴ The polarisation dependence of the coupling efficiency reported in [93] probably resulted from the polarisation dependent reflection of a mirror between the resonator and the transmission power photodiode.

Figure 4.9: Transporting atoms inside the resonator. By introducing a frequency difference of 200 kHz between the resonator beams, we move the atoms inside the standing wave within ~ 140 ms to the waist position, where the gas is subsequently evaporatively cooled in a running wave trap and loaded into the FORT for transport.

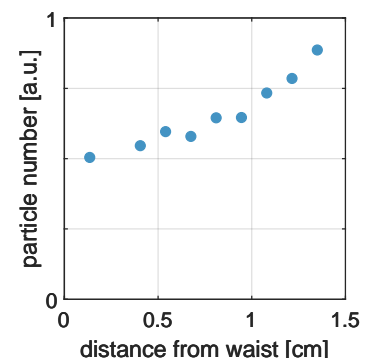


Figure 4.10: Measured particle number N in dependence of the distance from the resonator waist.

³⁵ We realized that it is helpful to introduce an adjustable time interval Δt for which the lock is enabled after reaching the power threshold for optimal operation. This time interval increases the duration for which the lock is enabled during the frequency scan and thereby improves the frequency lock fidelity.

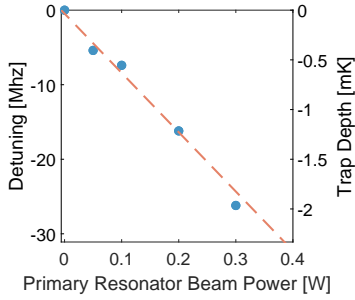


Figure 4.11: We determine the trap depth at the focus position of the resonator inside a running wave. The trap depth is determined by measuring the light shift caused by the trapping potential. The primary resonator beam power denotes the measured power before the input mirror.

³⁶ A satisfactory operation of the resonator requires an additional overhead in the maximal available power of ~ 0.5 W to further suppress noise with the laser power control and enable a sufficiently large buffer to fluctuations of the fiber coupling efficiency.

³⁷ The introduced frequency detuning $\Delta\nu_{\text{AOM}} > \Gamma$ reduces the transmission power due to the limited linewidth $\Gamma \approx 80$ kHz of the resonator.

sufficiently high transmission powers and thereby prevents the undesired locking of the laser to higher resonator modes. In practice, this *lock block* compares the measured primary beam transmission power $P_{1,\text{act}}$ during the frequency scan with an adjustable threshold $P_{1,\text{min}}$ and enables the lock for a certain time window Δt once $P_{1,\text{act}}$ exceeds $P_{1,\text{min}}$.³⁵

To load atoms into the resonator, we stabilise the power of each incoming resonator beam to ~ 1 W, compress the MOT and shift it to a position about ~ 3 cm off-center from the waist of the resonator. At this transfer position, the waist of the resonator beams is increased from its minimal waist of $w_0 = (20 - 30)\mu\text{m}$ to $w = (200 - 300)\mu\text{m}$ which ensures a larger overlap with atoms inside the MOT and therefore increases the transfer efficiency.³⁶ We then introduce a frequency difference $\Delta\nu_{\text{AOM}} = \nu_{\text{AOM},2} - \nu_{\text{AOM},1} = 200$ kHz between the resonator beams to move the standing wave at a speed of ~ 0.2 m/s and transport the atoms within 137.5 ms to the waist position of the resonator mode, where the secondary beam can be switched off completely (s. Fig. 4.9).³⁷ To reduce the initial acceleration during this transport we linearly increase the frequency difference to its maximal value $\Delta\nu_{\text{AOM}}$ within 100 μs .

Finally, we apply a magnetic offset field of 300 G and perform evaporative cooling at the waist position in the remaining running wave of the primary beam. Due to the increased intensity in the waist position, we need to decrease the power of the primary beam from 1 W down to ~ 10 mW for evaporation.

To keep the laser locked to the cavity while reducing the power by a factor of ~ 100 , we use an AOM to keep a constant reflected light power of 40 μW directly in front of the reflection PD and thereby maintain the error signal amplitude during evaporation.

5

NOVEL METHODS FOR THE PREPARATION AND CHARACTERISATION OF ULTRACOLD 2D FERMI GASES

In this chapter, I describe in more detail our realisation and characterisation of ultracold 2D Fermi gases. Particular focus is given on our implementation of novel methods ranging from a stable single-layer preparation to the projection of tailored optical potentials, a calibration of absorption imaging and finally measurements of the momentum distribution. Parts of these results are published in

K. Hueck, N. Luick, L. Sobirey, T. Lompe, H. Moritz, L. Clark, and C. Chin, Opt. Express 25, 8670 (2017)

and the supplementary materials of

K. Hueck, N. Luick, L. Sobirey, J. Siegl, T. Lompe, and H. Moritz, Phys. Rev. Lett. 120, 060402 (2018).

For both publications, I contributed to the conception and conduction of experiments, the interpretation of our results and the writing of the manuscript.

5.1 Preparing a single-layer ultracold 2D Fermi gas

We realise our 2D Fermi gases by loading atoms into a repulsive 1D optical lattice with a lattice spacing of $l_{\text{latt}} \approx 2.9 \mu\text{m}$, which is created by the interference of two blue-detuned ($\lambda = 532 \text{ nm}$) beams intersecting with an opening-angle of 10.4° (s. Fig. 5.1). We achieve typical trap frequencies along the strongly confined direction of $\omega_z \approx 2\pi \times 12 \text{ kHz}$ (s. Fig. 5.4) which exceeds the chemical potential μ and temperature T of our system and thereby brings our gas into the 2D regime (s. Fig. 3.1). To deterministically load into a single layer of this optical lattice, we transfer our atoms from the FORT into a highly elliptical³⁸ red-retuned ($\lambda = 1064 \text{ nm}$) *squeeze* beam and increase its power to compress the gas along the z direction to a size of about $1 \mu\text{m}$. Since this size of the cloud is smaller than the lattice spacing, we can load into a single layer of our lattice by aligning the vertical position of the squeeze trap with a minimum of the optical lattice (s. Fig. 5.2A). Alternatively, by aligning the position of the squeeze with a maximum of the lattice potential we can create two adjacent layers with equal population (s. Fig. 5.2B). This alignment process requires an accurate control over the position of the squeeze trap which we achieve by using piezo-actuated mirrors in its beam path.

5.1.1 Detecting the occupation of individual layers

We verify the preparation of a single or a double-layer system by detecting the occupation in individual sites. While such a detection usually requires a high-resolution imaging system or stable magnetic field

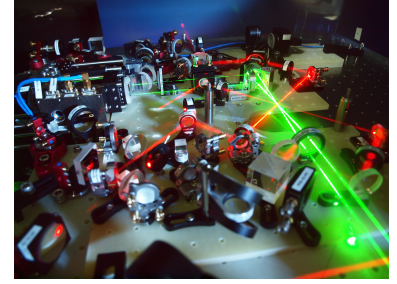


Figure 5.1: Optical lattice setup to create 2D Fermi gases. We create our optical lattice by the interference of two ($\lambda = 532 \text{ nm}$) beams which interfere in the center of the glass cell at the position of the atoms (green beams). Shown is the setup before integration into our experiment. Figure adapted from [109].

³⁸ $1/e^2$ waists of the squeeze trap:
 $w_y \times w_z \approx (400 \times 10) \mu\text{m}$

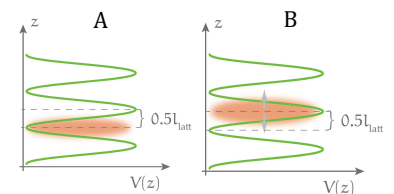


Figure 5.2: Illustration of single and double-layer loading. The squeeze trap (orange) is aligned with (A) a minimum or (B) a maximum of the repulsive optical lattice potential (green) to create a single or double-layer system respectively. Figure adapted from [79].

Figure 5.3: Single and double-layer loading and detection (a) We determine the occupation of individual layers in our lattice by flashing on the squeeze potential which separates adjacent layers after time of flight. (b) Absorption images of a double-layer (left) and single-layer (right) configuration. Adapted from the supplementary material of [96].

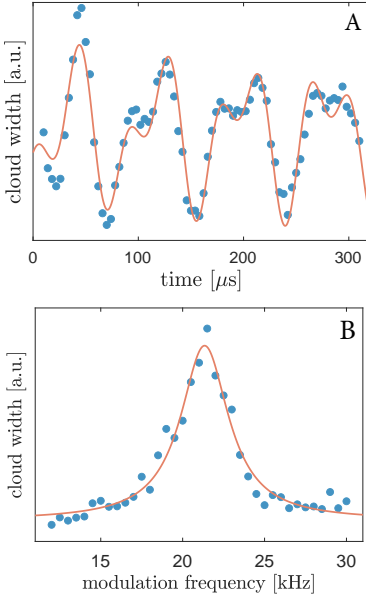
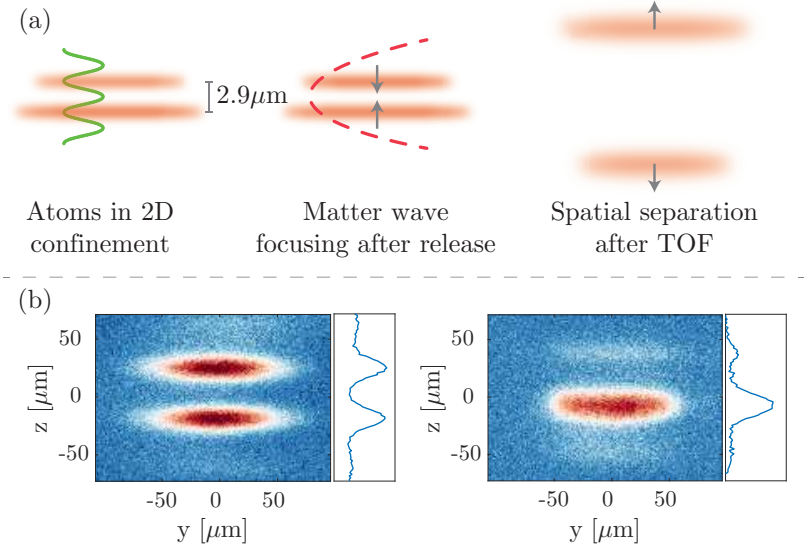


Figure 5.4: Trap frequency measurements. (A) We prepare a non-interacting double-layer system and briefly apply our squeeze trap to excite both a center of mass and a compression mode in each layer. Since our squeeze trap kicks each layer in opposite directions we can also detect the center of mass mode in the width of the cloud after expansion. We fit the resulting beat with a sum of oscillations at frequencies of $\nu_{01} = (12.4 \pm 0.1)$ kHz and $\nu_{02} = (23.3 \pm 0.1)$ kHz, which correspond to the center of mass mode and the compression mode respectively. The frequency of the compression mode is $\nu_{02} < 2\nu_{01}$ due to the anharmonicity of our trapping potential. (B) We modulate the intensity of our lattice potential for varying frequencies and measure the width of the cloud after a short TOF. We observe a pronounced maximum corresponding to the frequency ν_{02} of the compression mode.

gradients for a precise RF addressing of individual sites, we here show that a simple matter wave focusing technique can be used to determine the occupation in each layer of our lattice.

To resolve individual occupations we suddenly switch off the lattice, let the cloud expand for $50 \mu\text{s}$ and flash on the squeeze trap again for a short time of about $18 \mu\text{s}$. This flash gives individual sites a relative momentum to each other, which we resolve by imaging the system orthogonal to the kick direction after a short time of flight of 1 ms (s. Fig. 5.3B). This method enables us to detect the occupation in each layer with a high fidelity. In particular, we observe that for a fully thermalized machine our single and double-layer preparation remains stable over a timescale of hours (s. Fig. 5.5). To achieve a more robust loading under less reproducible conditions, we implemented an active feedback mechanism that detects the occupation of individual layers as described above and adjusts the vertical alignment of the squeeze trap accordingly. Using this feedback scheme we achieve a robust preparation of 2D Fermi gases which does not require any manual alignment on a timescale of days as required for the measurements presented in part III of this thesis.

5.1.2 Experimental verification of the 2D regime

To demonstrate that we have indeed realized a 2D system we have to show that the system occupies only the ground state along the tightly confined direction of our lattice potential. While in principle information about the occupation of higher transverse states could be obtained from in-situ measurements of the density distribution, resolving occupation numbers from such a measurement would be very challenging due to the very small length scales of the system on the order of the harmonic oscillator length of $l_z \approx 400 \text{ nm}$. Instead, we follow the approach established in [110] and access information about the occu-

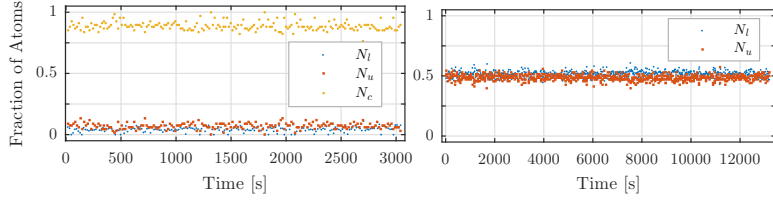


Figure 5.5: The occupations N_u , N_c , and N_l in the upper, central, and lower layer remain stable over a time scale of hours for both the single-layer (left panel) and double-layer (right panel) configuration. Figure adapted from the supplementary material of [96].

pation of transverse oscillator states by time of flight measurements. We prepare Fermi gases with densities ranging from $n = 0.2/\mu\text{m}^2$ to $n = 1.5/\mu\text{m}^2$, suddenly switch off the lattice and measure the width of the cloud along the previously strongly confined direction after a short time of flight (s. Fig. 5.6).

Once the chemical potential of our system reaches the oscillator spacing we expect a population of the first excited state which should lead to a broader momentum distribution and hence an increase in the density distribution after time of flight. Indeed, we observe that the width of the cloud remains constant up to some critical density³⁹ of $n_0 \approx 0.7/\mu\text{m}^2$ and then starts to increase for higher densities as higher oscillator states are populated. This measurement clearly shows that for sufficiently low densities we can realise an interacting 2D Fermi gas with a vanishing occupation of higher transverse states.

— *Extra 5.1: Do strong interactions break 2D kinematics?* —

For sufficiently high trap frequencies, $\hbar\omega_z > E_F > \mu$ we would expect to remain in the 2D regime in the entire BEC-BCS crossover since the chemical potential cannot exceed the Fermi energy. However, it is under debate if this simple criterion is accurate in the strongly interacting regime where $\ln(k_F a_{2D}) \approx 0$. While some argue that in this strongly correlated regime where $a_{3D} > l_z$ one should realize a true 2D system where scattering processes are also two-dimensional [81], others argue that the diverging scattering length inevitably leads to a dominant contribution of higher excited states and hence a breakdown of 2D kinematics even for a chemical potential $\mu \ll \hbar\omega_z$ well below the oscillator spacing [111]. While time of flight measurements for a strongly interacting 2D Fermi gas are available to support the claimed breakdown of 2D kinematics (s. Fig. 5.7) [110], it was recently argued that this data could also be interpreted in terms of an increased role of interactions during the expansion of a superfluid [80]. In fact, even for a system in the transverse ground state interactions during the initial expansion dynamics would lead to a density dependent change of the cloud width after time of flight. So far, the question if strong interactions break 2D kinematics is an important unresolved issue [80] which deserves further experimental investigation.

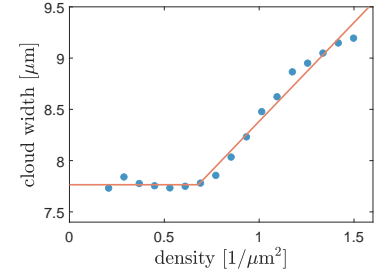


Figure 5.6: Verification of the 2D regime We prepare an interacting 2D Fermi gas at a magnetic offset field of $B = 1020\text{G}$ with varying densities, switch off the trap and measure the width of the cloud after a short expansion time. Below a critical density of $n_0 \approx 0.7/\mu\text{m}^2$ the width saturates towards a density independent value which shows that all particles occupy the vertical ground state of the lattice potential.

³⁹ This critical density corresponds to a critical Fermi energy of $E_{F,0} \approx 7.4\text{kHz}$ which is reduced from its theoretical maximum of $E_{F,0} = \hbar\omega_z$ due to the finite temperature of $T/T_F \approx 0.3$ in this measurement.

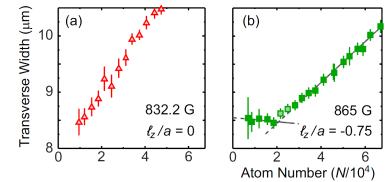
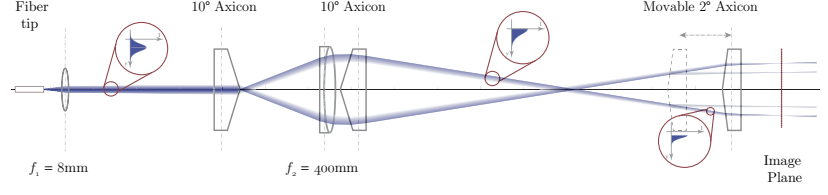


Figure 5.7: First study of criteria for 2D kinematics reported in [110]. Analogous to our measurement shown in Fig. 5.6 the cloud width after release from the confinement is measured for various particle numbers N for (a) $l_z/a_{3D} = 0$ and (b) $l_z/a_{3D} = -0.7$. Adapted from [110]

Figure 5.8: Generation of the ring potential. The ring potential is generated by a setup of two lenses and three axicons with different opening angles. The two lenses image the fiber tip onto an intermediate image plane (red dotted line), which is then imaged onto the atoms using a high resolution objective (not shown). The first axicon splits the beam into a ring beam which is then optically inverted by the combination of a second axicon and the second lens. After this optical inversion the steep part of the split Gaussian beam faces towards the center of the ring. The movable third axicon collimates the geometry of the ring with a variable diameter. Adapted from the supplementary materials of [96].



5.2 Projecting tailored potentials

Here, we present how we use our high-resolution microscope objective to project tailored optical potentials onto our 2D Fermi gas which enables us to manipulate the density and phase of our gas on the order of the interparticle distance. This capability enables us to create steep box potentials and narrow tunnelling barriers required for the realisation of homogeneous systems and Josephson junctions in our 2D Fermi gas.

5.2.1 Optical ring potential

So far, experiments with 2D Fermi gases were performed in harmonic traps, which gives rise to an inhomogeneous density distribution which can be a limiting factor for the creation and characterisation of many body states [78]. Recently, these issues were overcome by trapping atoms in a box potential which results in gases with a uniform density distribution [112–114]. We create the first homogeneous 2D Fermi gases with our setup by projecting a repulsive optical ring potential onto our 2D gas.

In principle, such ring potentials can be generated by imaging a mask, which blocks large parts of the beam and is therefore less power efficient. Instead, we follow an approach similar to the one described in [114] and create the ring potential using axicons, which enables us to guide all of the incoming light into a ring shape and thereby realise high intensities in the walls at a moderate beam power. In contrast to the setup presented in [114], our optical setup uses a set of three axicons and lenses (s. Fig. 5.8) which enables the creation of steep potential walls on the inside of the ring potential (s. Fig. 5.9). For more details on the design, implementation and characterisation of our ring potential setup see [79].

5.2.2 Projecting tailored potentials using digital micromirror devices

Digital-micromirror-devices (DMD) are uniquely suited to modify the spatial intensity profile of light, and have therefore become a well-established experimental tool to generate arbitrary potentials for ultracold atoms. For the experiments presented in this thesis, we use two separate DMDs⁴⁰ which are both illuminated with $\lambda = 532$ nm light and directly imaged onto our 2D Fermi gas with a demagnifi-

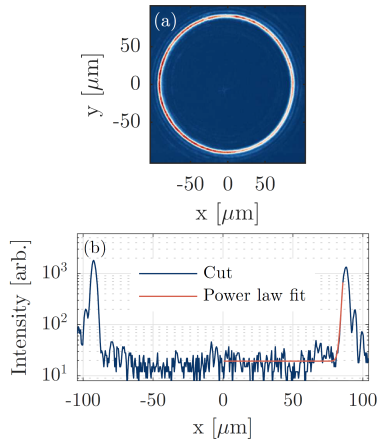


Figure 5.9: Characterizing the box potential. A cut (b) through an image of the ring potential (a) reveals the steepness of the potential wall. The potential can be approximated by a power law fit $V(x) \propto x^{87 \pm 4}$. Figure and caption adapted from the supplementary materials of [96].

⁴⁰ Texas Instruments DLP6500FYE

cation of ~ 50 . This setup enables us to create a variety of repulsive potentials ranging from box potentials to narrow tunnelling barriers and sharp potential steps, which we use to realize homogeneous systems, Josephson junctions and control the local phase of our system.

By using two separate DMDs we achieve a greater dynamic control over time dependent potentials. To dynamically change the potential in time, we display separate patterns on each DMD and control the power of the illuminating light on each DMD individually, which enables us to smoothly change between images. While in principle a single DMD would be sufficient to change the potential in time by displaying a series of images, the switching between images is only possible at a rate of ~ 10 kHz which would be limiting for experiments that require fast changes on a timescale of $\sim 1 \mu\text{s}$. In addition, this switching between patterns is accompanied by a short $1 \mu\text{s}$ time interval in which the display is in an off-state. Since this flickering noise would lead to heating and is already a problem for static potentials, we have developed a method to stop the intrinsic refresh rate of each DMD and create static low-noise potentials (s. Fig. 5.10). For more details on the design, implementation and characterisation of our DMD setup see [79].

5.3 Calibrating high intensity absorption imaging

Absorption imaging is a well-established experimental technique to gain quantitative information about the density distribution of cold atom systems. The basis for this imaging method is the absorption of resonant light by atoms, which creates a shadow that is imaged onto a camera and translated to an absolute density by comparing the incoming and outgoing intensities I_{in} and I_{out} . For low intensities, the relation between incoming and outgoing light intensity takes a simple logarithmic form as described by the Beer-Lambert law

$$\sigma_0 n_{2D} = -\ln\left(\frac{I_{\text{out}}}{I_{\text{in}}}\right), \quad (5.1)$$

and the 2D density n_{2D} can be extracted from the ratio $\frac{I_{\text{out}}}{I_{\text{in}}}$ and the scattering cross-section σ_0 . However, this low-intensity regime generally corresponds to very few scattered photons which is not ideal for an optimal signal-to-noise ratio and generally not suited for optically dense systems. To overcome these issues, we perform absorption imaging at high intensities $I \approx I_{\text{sat}}$, where the saturation of the optical transition leads to the more general relation for the density

$$\sigma_0 n_{2D} = -\ln\left(\frac{I_{\text{out}}}{I_{\text{in}}}\right) + \frac{I_{\text{in}} - I_{\text{out}}}{I_{\text{sat}}^{\text{eff}}}, \quad (5.2)$$

which is modified compared to eq. 5.2 by an additional linear term determined by the ratio I/I_{sat} of the intensity relative to the saturation intensity I_{sat} . While in principle, the ratio I/I_{sat} can be determined by using the absolute value for $I_{\text{sat}} = 2.54 \text{ mW/cm}^2$, estimating the absolute light intensity I at the position of the atoms suffers from sys-

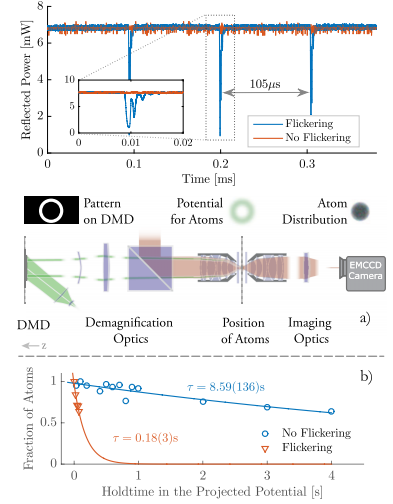
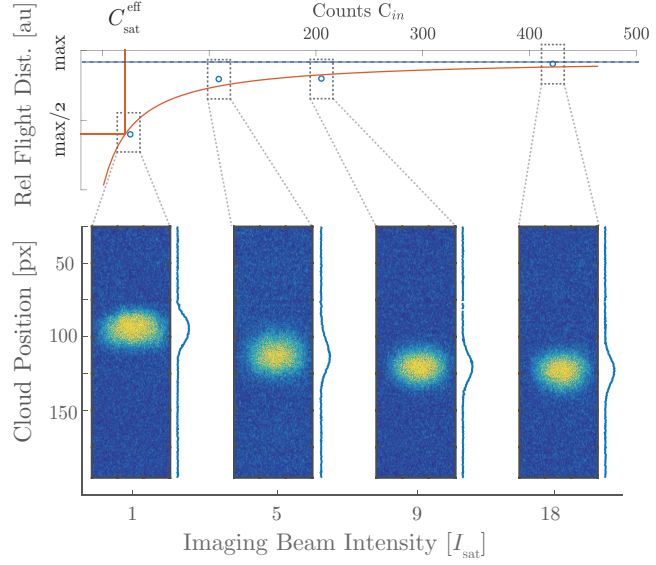


Figure 5.10: Reflection signal of the DMD with applied mirror clocking pulse (MCP) and with the MCP pulled to ground (red line). The lifetime of a gas trapped inside light reflected of a DMD is greatly enhanced when the flicker of the DMD mirrors is disabled. Figure and caption adapted from [115]

Figure 5.11: Calibrating the imaging beam intensity for high-intensity absorption imaging. We use our imaging beam to illuminate our cloud for a short time of $1\ \mu\text{s}$ and measure the momentum transferred onto the atoms from the flight distance of the cloud after a short time of flight. We observe that the flight distance and hence the rate of scattered photons per atom saturates which is used to calibrate the intensity I of our imaging beam in units of the saturation intensity I_{sat} . Figure adapted from [116].



tematic uncertainties. Furthermore, to account for potential imperfections in the imaging caused e.g. by mismatches in the polarisation, both the scattering cross section and saturation intensity have to be replaced by effective values $\sigma_{\text{eff}} = \sigma_0/\alpha$ and $I_{\text{sat}}^{\text{eff}} = I_{\text{sat}}/\alpha$ determined by some scaling factor $\alpha \geq 1$, which is not *a-priori* known. Finally, an additional complication in the high-intensity regime with many scattered photons per atom is the accumulated Doppler shift of each atom which is particularly relevant for light elements such as ${}^6\text{Li}$.

Here, we present a novel calibration method for high-intensity absorption imaging which overcomes the issues described above. The central idea behind our method is to measure the momentum transferred from the imaging beam onto the atoms as a reference for the scattering rate to calibrate the saturation intensity I_{sat} and the scaling factor α . To measure the momentum transferred onto the atoms we record the flight distance along the propagation of the imaging beam a short time after the illumination (s. Fig. 5.11). We repeat this measurement for varying imaging intensities and observe that the flight distance and hence the scattering rate saturates for large intensities according to

$$\gamma = \frac{\Gamma}{2} \frac{s_0}{1 + s_0} \quad (5.3)$$

from which we extract the intensity of our imaging beam in units of the recorded count rate c_{sat} on our camera. To obtain the scaling factor α , we first set the polarisation of our imaging beam to σ^+ , which is orthogonal to our addressed σ^- transition, and measure the residual scattering rate at high beam intensity $I^+ \gg I_{\text{sat}}$. Afterwards, we set the polarisation back to σ^- and find the value I^- which corresponds to the same scattering rate. We obtain a ratio $I^+/I^- \approx 0.004$ which corresponds to a polarisation purity of 99.6% and we can therefore set $\alpha = 1$. Additionally, we use the measurement of the scattering rate described above to calibrate a frequency chirp during the imaging which

compensates the accumulated Doppler shift and enables us to maintain an optimal photon scattering rate for imaging pulse durations up to $\sim 10 \mu\text{s}$. For more details on our calibration of high intensity absorption imaging see appendix A and [116].

5.4 Measuring the momentum distribution using matter wave focusing

After we have shown how to prepare 2D Fermi gases in various geometries and accurately determine the density of such systems, we finally show how to measure its momentum distribution. The momentum distribution $n(\mathbf{k})$ of a quantum system is of fundamental interest, because it contains information about the phase of the superfluid order parameter Ψ , which is not detectable in single in-situ measurements of the density $n = |\Psi|^2$. In particular, for our 2D Fermi gas the momentum distribution $n(\mathbf{k})$ is used to observe Pauli blocking in momentum space (s. part II), access the phase difference of Josephson junctions (s. part III) and could enable future studies of the degree of phase coherence as a probe for BKT physics.

A well-established technique to measure the momentum distribution of ultracold gases is to release the gas from the trap and reconstruct the momentum of particles from their position after a certain *time of flight*. Commonly, such time of flight measurements are performed in the presence of an underlying harmonic trap $V(\mathbf{r}) = \frac{1}{2}m\omega_r^2 r^2$, in which case the momentum distribution can be directly obtained from the density distribution $n(\mathbf{r}, t)$ after a time $t = T/4$

$$\tilde{n}(\mathbf{k}) = l_r^4 n(\mathbf{r} = \mathbf{k}l_r^2, t = T/4), \quad (5.4)$$

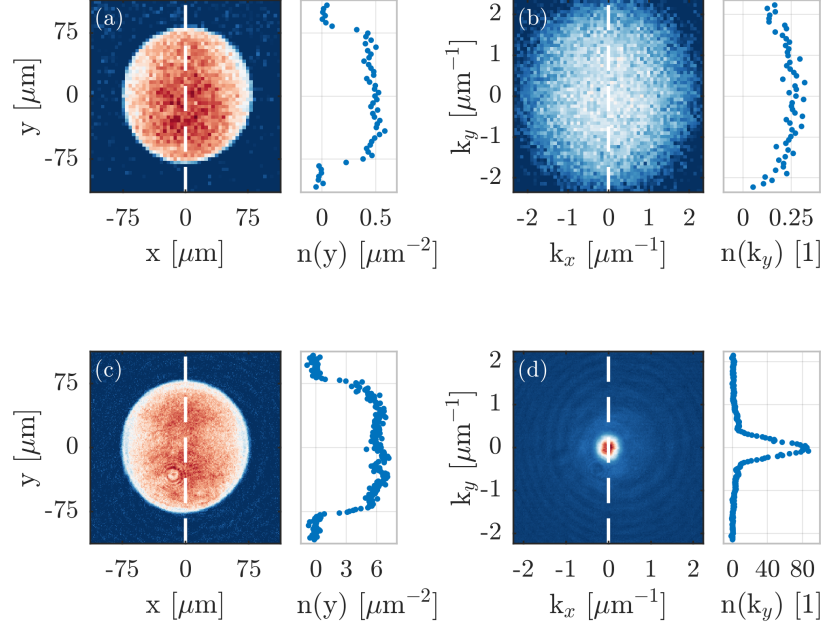
where the scaling factor is determined by the harmonic oscillator length $l_r = \sqrt{\hbar/m\omega_r}$ and T is the oscillation period in the harmonic potential. Recently, such matter wave focusing⁴¹ measurements were applied to harmonically trapped 2D Fermi gases to observe pair condensation [100] and to measure the decay of the first order correlation function $g_1(\mathbf{r}) = \text{F.T.}(\tilde{n}(\mathbf{k}))$ [78].

We apply matter wave focusing for the first time to homogeneous 2D Fermi gases trapped in a box potential as described in detail in chapter 6. In contrast to harmonically trapped systems, the in-situ density distribution in our box potential does not change when crossing over from the bosonic to the fermionic limit (s. Fig. 5.12). The momentum distributions, however, show a dramatic difference between these two regimes. On the BEC side we detect a narrow peak corresponding to the macroscopic occupation of low-momentum modes, while for non-interacting fermions we detect a much broader momentum distribution corresponding to a occupation of momentum states up to the Fermi wave vector k_F .

To extract quantitative information about the momentum distribution from these measurements, we need to address two technical complications that are common to time of flight measurements. First, interactions between particles during time of flight can significantly modify the detected momentum distribution. Second, switching off the

⁴¹ Matter wave focusing can be understood as a direct analogy of coherent light propagation through a lens, since the light distribution in the focal plane of a lens is determined by the Fourier transform of the incident light field [117].

Figure 5.12: Measurements of the in-situ and momentum distribution in the fermionic and bosonic limit. In our box potential, the in-situ density distribution is qualitatively similar for (a) a non-interacting 2D Fermi gas and (c) a gas of deeply bound dimers. We extract the momentum distribution of both systems using matter wave focusing and observe (b) a broad distribution in the fermionic limit and (d) a very narrow peak in the bosonic regime indicating the macroscopic occupation of low-momentum modes.



trap leads to a rapid expansion along the strongly confined direction which complicates the imaging of the system within the depth of field of our microscope objectives. In the following, we will present our approach to address both issues. In particular, we show how a spin removal technique can be used to eliminate interactions during the initial expansion of an interacting 2D Fermi gas. Finally, we present an optical slicing technique which enables a full resolution of the finite size limited momentum distribution in the bosonic limit.

5.4.1 Reducing the influence of interactions during time of flight

Parts of the following section have been adopted with minor modifications from the supplementary materials of [96].

A central assumption in matter wave focusing to obtain the in-situ momentum distribution $n(\mathbf{k})$ according to eq. 5.4 is a free time evolution of the wave function, which is justified when the mean number of scattering events per particle $N_{\text{sc}} \ll 1$. While for 2D systems the rapid initial expansion during matter wave focusing leads to a quick decrease in the density and hence reduces scattering, there can still be a significant number of scattering events in particular in the strongly interacting regime [110]. To circumvent this issue previous experiments with 2D Fermi gases used a rapid ramp of the magnetic field deep into the bosonic regime, which results in the formation of deeply bound dimers with a significantly reduced interaction strength [63].

Here, we present our implementation of an optical spin ejection which quenches the gas to the non-interacting regime and thereby enables us to measure the atomic momentum distribution $\tilde{n}(\mathbf{k})$ and the corresponding occupation $f(k)$ of interacting 2D Fermi gases. To eliminate the influence of collisions, we remove one of the spin com-

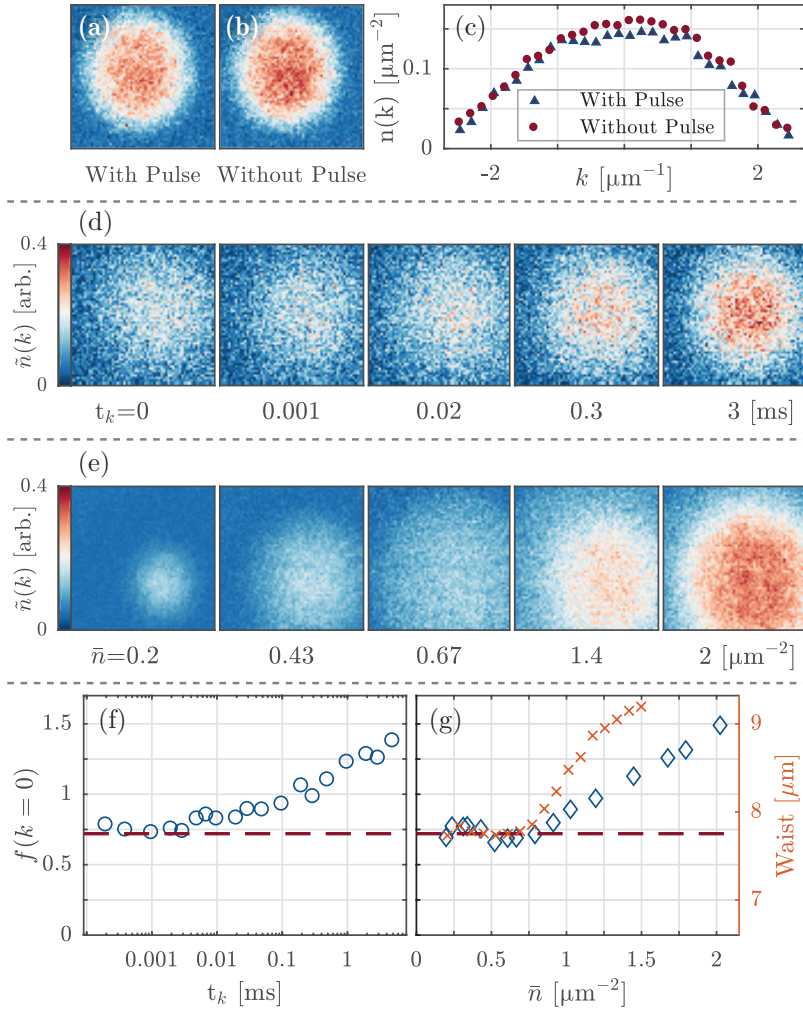


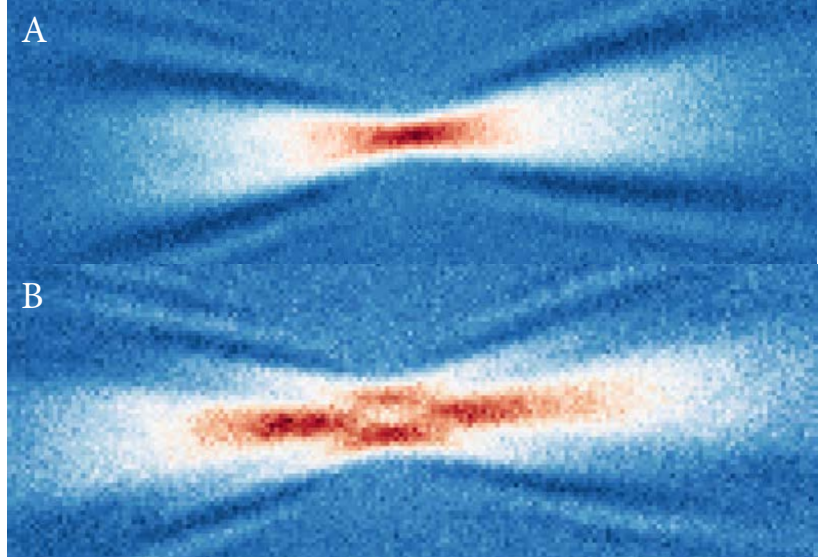
Figure 5.13: Influence of collisions and transverse excited states on matter wave focusing. To prevent collisions during matter wave focusing, we remove state $|\uparrow\rangle$ using a resonant light pulse. To verify that this pulse has only negligible effects on atoms in state $|\downarrow\rangle$, we compare measurements with (a) and without (b) the pulse in a non-interacting system. Line cuts (c) through these images show that the momentum distribution of state $|\downarrow\rangle$ in a non-interacting system is not significantly altered by the optical removal pulse. For an interacting system, we map out the effect of collisions on the measured momentum distribution by waiting for a variable interaction time t_k between switching off the optical confinement and removing state $|\uparrow\rangle$. With increasing t_k , we observe a redistribution of momentum (d,f). For comparison, the central occupation obtained with $t_k = 0$ in Fig. 6.4 (c) is marked by red dashed lines. An additional source for error is that for high 2D densities, low momentum modes in higher transverse levels become occupied. We record the momentum distribution for different in situ densities \bar{n} (e) and observe an increase in central momentum occupation (blue diamonds, (g)) above a density of $\bar{n} \approx 0.75/\mu\text{m}^2$. For comparison, we show our data from Fig. 5.6 (red crosses), which indicate an occupation of higher transverse states at the same density. Figure and caption adapted from the supplementary materials of [96].

ponents, thereby effectively projecting the system onto a free Fermi gas. We accomplish this by illuminating the atoms in state $|\uparrow\rangle$ with a resonant $2\ \mu\text{s}$ light pulse with an intensity of $I = I_{\text{sat}}$ before performing matter wave focusing. This removes the atoms in state $|\uparrow\rangle$ with a $1/e$ time constant of $\tau_{\uparrow} \approx 150\ \text{ns}$, whereas state $|\downarrow\rangle$ has a much longer lifetime of $\tau_{\downarrow} \approx 70\ \mu\text{s}$. Using a non-interacting Fermi gas, we verify that the momentum distribution of state $|\downarrow\rangle$ is not significantly altered by the light pulse (Fig. 5.13 (a-c)).

We then apply this method to an interacting system at $B = 1020\ \text{G}$. We map out the influence of interactions on the momentum distribution by switching off the z -confinement and removing state $|\uparrow\rangle$ after different expansion times t_k . We observe that when increasing the time t_k during which collisions can take place beyond $3\ \mu\text{s}$, the apparent occupation of lower momentum modes increases (see Fig. 5.13 (d,f)). We attribute this to collisions transferring momentum from the radial into the transverse direction.

Finally, the dimensionality of the system has a profound impact on the momentum distribution. For low densities, our system is in the

Figure 5.14: Momentum space slicing. We image the momentum distribution of a 2D homogeneous Fermi gas with size $(40 \times 40)\mu\text{m}$ in the limit of deeply bound dimers. (A) A small tilt angle between the imaging beam and the expansion axis enables us to spatially separate the central in-focus part from the outer image-broadened part of the imaged distribution. (B) We imprint a phase difference of π on one half of the box system and observe two distinct maxima which shows our ability to resolve the Fourier limited width of such a system with a size on the order $40\mu\text{m}$.



2D regime and we find that $f(k=0)$ remains constant as we increase the density, while the width of the distribution grows. As the density surpasses a value of $n \approx 0.75/\mu\text{m}^2$, $f(k=0)$ begins to increase which we attribute to the population of higher transverse states (see Fig. 5.13 (e.g)). This interpretation is supported by our previously presented measurement of the transverse width of the cloud after short time of flight (s. Fig. 5.6), where the transverse width starts to increase around the same density, signalling the beginning of the crossover to a 3D system.

5.4.2 Resolving finite-size limited momentum peaks

Measurements of the momentum distribution $\tilde{n}(k)$ of a uniform 2D Bose gas can be used to obtain $g_1 = \text{F.T.}(\tilde{n}(k))$ and thereby directly show the predicted algebraic decay of phase coherence and quantitatively extract the scaling exponent η . However, such a measurement requires resolving narrow momentum peaks which is a challenging task.

For a uniform BEC at zero-temperature, the width $\Delta k = \pi/L$ of the momentum distribution

$$n(k) \propto \text{sinc}^2\left(\frac{kL}{2}\right) \quad (5.5)$$

decreases with the size L of the system which using matter wave focusing corresponds to a width in position space of $\Delta x = \pi l_r^2/L \approx 2\mu\text{m}$ for typical experimental parameters of $L = 40\mu\text{m}$, $\omega_r = 2\pi \times 30\text{Hz}$, $l_r = 5.3\mu\text{m}$. In principle, such small spatial structures on the order of $2\mu\text{m}$ can be resolved for systems within the depth of field of our imaging system. However, the rapid expansion of the cloud during matter wave focusing leads to a spatial extent of the cloud which greatly exceeds our depth of field and therefore significantly limits the achievable spatial resolution. While previous measurements addressed this

issue by compressing the cloud shortly after the release, the width of the cloud could in these experiments still not be kept within the depth of field which lead to a significant broadening of the detected momentum distribution [78]. Furthermore, compressing the cloud during time of flight also increases the density and hence the effect of undesired interactions during the expansion.

Here, we employ a simple modification of matter wave focusing that enables a full optical resolution of Fourier limited momentum peaks. We achieve this by performing matter wave focusing of a homogeneous 2D Bose system with size $L \times L = (40 \times 40) \mu\text{m}$ and using a small tilt angle between the imaging beam and the expansion axis. This tilt results in cone-shaped absorption images of the momentum distribution, where the part of the cloud within the focal plane of our objective can be easily isolated from the regions which are out of focus (s. Fig. 5.14). This enables us to slice through the narrow in-focus part of the image to get a quantitative measure of the momentum distribution. To test the achievable resolution in this in-focus part of the momentum distribution we imprint a phase difference of π on one half of the box system, which in momentum space should correspond to two equally high peaks whose respective width is defined by the size L of the system. Indeed, we observe two clearly pronounced peaks which shows that our resolution in momentum space is sufficient to resolve the finite size limited width of $\tilde{n}(\mathbf{k})$ for system sizes on the order of $40 \mu\text{m}$.

Part II

HOMOGENEOUS TWO-DIMENSIONAL FERMI GASES

6

HOMOGENEOUS TWO-DIMENSIONAL FERMI GASES

In this chapter, we report on the experimental realization of homogeneous 2D Fermi gases with tunable interactions, which is published in

*K. Hueck, N. Luick, L. Sobirey, J. Siegl, T. Lompe, and H. Moritz,
Phys. Rev. Lett. **120**, 060402 (2018)*

and reprinted here with minor modifications. I contributed to the conception and conduction of all measurements presented here, including the interpretation of our results and the writing of the publication.

Ultracold 2D Fermi gases are uniquely suited to investigate the interplay of reduced dimensionality and strong interactions in quantum many-body systems in a clean and well-controlled environment. Experiments have reported on the creation of 2D Fermi gases with equal [118, 119] and unequal spin populations [120, 121] and investigated pairing [122–125], Fermi-liquid [126] and polaron physics [127, 128]. The EOS [129–131] was determined and evidence for pair condensation [63] and for a Berezinskii-Kosterlitz-Thouless (BKT) transition [132] could be observed. Yet so far, ultracold 2D Fermi gases have always been studied in harmonic trapping potentials, which qualitatively change the density of states and give rise to inhomogeneous density distributions. This hinders the observation of critical phenomena with diverging correlation length and exotic phases such as the Fulde-Ferrell-Larkin-Ovchinnikov (FFLO) state [133–136]. Furthermore, the inhomogeneous density distribution complicates the interpretation of non-local quantities such as correlation functions or momentum distributions, which can only be extracted as trap-averaged quantities [63, 132].

These issues can be overcome by creating homogeneous gases in box potentials whose walls are formed by repulsive optical dipole potentials. Following this method, three-dimensional (3D) uniform Bose gases have recently been realized and used to investigate coherence and thermodynamic properties [112, 137] as well as non-equilibrium dynamics [113]. In homogeneous 2D Bose gases, the emergence of condensation, vortices and supercurrents were studied [138, 139]. Very recently, the creation of 3D Fermi gases in a box potential has been demonstrated, Pauli blocking in momentum space was observed and both balanced and imbalanced Fermi gases have been studied in the strongly-interacting regime [114].

In this chapter, we report on the experimental realization of homogeneous 2D Fermi gases with tunable interactions. By preparing a non-interacting Fermi gas we realize a textbook example of statistical physics and directly observe Pauli blocking in the occupation of momentum states. To measure the momentum distribution of interacting gases we have established a technique to rapidly remove one

spin component and thereby project the system onto a non-interacting state. We apply this technique to a gas with intermediate attractive interactions and observe a momentum distribution that is qualitatively similar to that of a non-interacting gas.

6.1 Experimental realisation of a homogeneous 2D Fermi gas

We perform our experiments with an equal spin mixture of ${}^6\text{Li}$ atoms in the lowest two hyperfine states $|F, m_F\rangle = |\frac{1}{2}, \frac{1}{2}\rangle$ and $|\frac{1}{2}, -\frac{1}{2}\rangle$, which we designate as $|\uparrow\rangle$ and $|\downarrow\rangle$, respectively. A sketch of the experimental setup is shown in Fig. 6.1(a). The atoms are pre-cooled as described in [140] and then transferred into a hybrid trap consisting of a highly elliptic red detuned optical trap and a variable radial magnetic confinement, which is generated by the curvature of the magnetic offset field used to tune the interparticle interactions. This variable trapping can be used to compensate for anti-confinement introduced by the lattice potential, which provides the 2D confinement described below. After forced evaporative cooling in the elliptic trap (Fig. 6.1(d)), we ramp on a repulsive optical ring potential as sketched in Fig. 6.1(b,c). This ring potential is generated by a cascaded setup of three axicons and projected onto the atoms using a high-resolution ($\text{NA} = 0.62$) objective [114, 141, 142]. We use the ring to cut out the central, low-entropy part of the cloud (Fig. 6.1(e)) and then ramp down the radial magnetic confinement such that the excess atoms outside the ring leave the observation volume. Next, we bring the gas into the 2D regime by loading it into a blue detuned optical lattice in z -direction. In this lattice, the level spacing $\hbar\omega_z = h \cdot (12.4 \pm 0.1)$ kHz between the ground and first excited state in the vertical direction exceeds both the highest chemical potential $\mu < h \cdot 4$ kHz and the highest thermal energy $k_B T < h \cdot 2$ kHz encountered during our experiments and hence the system is in the 2D regime [143].

To transfer the atoms into a single node of the lattice, we recompress the cloud by ramping up the power of the elliptic trap, which reduces the width of the cloud in z -direction below the lattice spacing of $2.9 \mu\text{m}$. By optimizing the position of the elliptic trap with respect to the lattice, optimally 93% of the atoms can be loaded into a single layer, where the number of atoms in adjacent layers can be determined to high precision in a single shot matter wave focusing measurement. By shifting the z -position of the elliptic trap by half a lattice period, it is also possible to create two equally populated adjacent layers [144]. This makes the loading of non-interacting gases more robust against populating adjacent layers by thermally excited atoms and furthermore doubles the recorded signal for absorption imaging.

In a first series of experiments, we study a non-interacting Fermi gas, which provides us with a well-defined starting point for our exploration of interacting systems. To create such non-interacting systems we first prepare a dual layer homogeneous 2D Fermi gas at a magnetic offset field of $B = 320$ G. At this field the gas is weakly in-

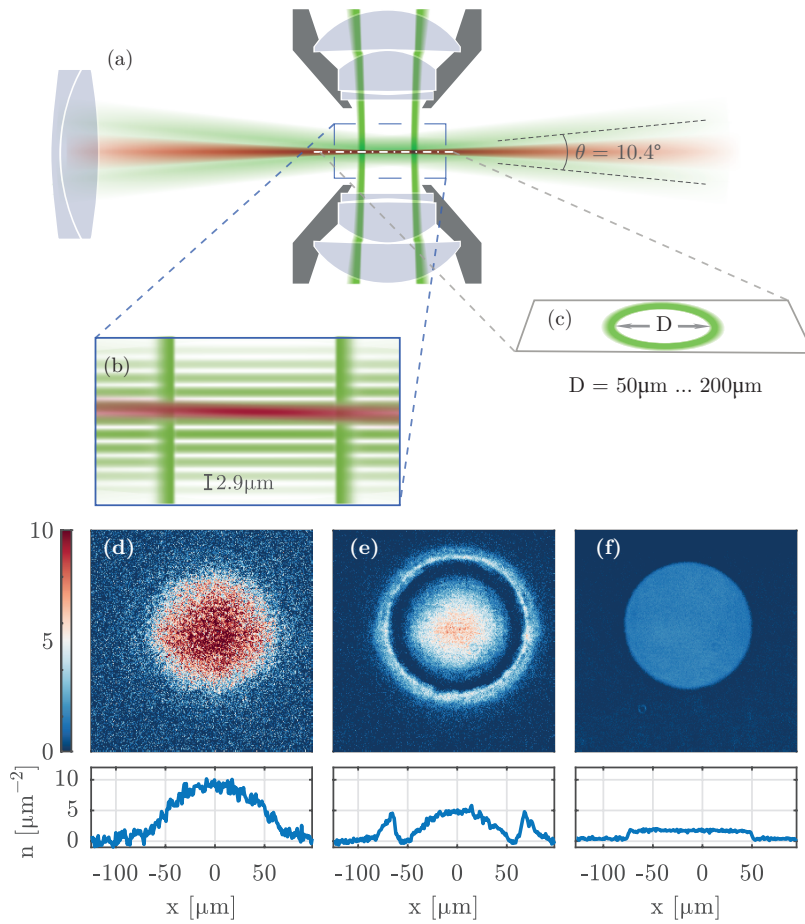


Figure 6.1: Sketch of the experimental setup: The atoms are loaded from a highly elliptic red detuned optical trap (red) into a single nodal plane of a blue detuned optical lattice (light green) which is formed by two laser beams ($\lambda = 532 \text{ nm}$) intersecting under an opening angle of $\theta = 10.4^\circ$ (a,b). The radial confinement is provided by a ring-shaped repulsive potential (dark green) whose diameter D can be adjusted between $50 \mu\text{m}$ and $200 \mu\text{m}$ (c). Panels (d-f) show averaged (20 - 50 images) in situ density profiles and respective central line cuts at different stages of the preparation of a strongly interacting homogeneous Fermi gas at $B = 830 \text{ G}$: After evaporation in the elliptic trap (d), the outer, high entropy region of the cloud is cut away by the repulsive ring potential (e). After further evaporation, the radial magnetic confinement is ramped down to spill the atoms outside the ring and the atoms are transferred into the lattice and we obtain a homogeneous 2D gas (f).

interacting with a 3D scattering length of $a_{3D} = -290 a_0$, where a_0 is the Bohr radius. We perform further evaporative cooling by slowly decreasing the height of the confining ring potential and then ramp to $B = 527 G$, which is close to the zero crossing of the scattering length, to obtain a non-interacting Fermi gas.

6.2 Measurement of the equation of state

As a first benchmark experiment, we measure the density EOS $n_{2D,\uparrow}(\mu, T)$ of this non-interacting Fermi gas. We imprint a potential step, which is generated by a blue detuned laser beam reflected off the surface of a digital micromirror device (DMD) and projected onto the atoms [94]. We then image the resulting density distribution using high-intensity absorption imaging [116, 145]. As shown in Fig. 6.2(a,b), the repulsive potential causes a disk shaped density depletion in the center of the cloud which covers about 10 % of its area. We apply potential steps with different heights V while observing the corresponding density depletion $\Delta n(V) = n_{2D,\uparrow}^{\text{disk}} - n_{2D,\uparrow}^{\text{center}}(V)$, where $n_{2D,\uparrow}^{\text{disk}}$ and $n_{2D,\uparrow}^{\text{center}}$ correspond to the single layer density in the undisturbed and depleted parts of the trap, respectively. We perform such EOS measurements for gases with different densities and temperatures; the resulting datasets are shown in Fig. 6.2.

We calibrate the potential step height V by performing a linear Thomas-Fermi fit to the first four points of the different EOS measurements and take the mean of the resulting values [131]. To extract the temperature and chemical potential, we fit the density depletion with $\Delta n(\mu_0, T, V) = n_{2D,\uparrow}(\mu_0, T) - n_{2D,\uparrow}(\mu_0 - V, T)$ using the theoretical EOS $n_{2D,\uparrow}(\mu, T) = \lambda_{dB}^{-2} \log[1 + \exp(\mu/\beta)]$ for a non-interacting 2D Fermi gas [146]. Here, $\beta = (k_B T)^{-1}$ and the thermal de Broglie wavelength is given by $\lambda_{dB} = \sqrt{2\pi\hbar^2/mk_B T}$, where m is the mass of a ${}^6\text{Li}$ atom. We approximate the chemical potential μ_0 in the outer part of the trap to be constant for all step heights. For our coldest dataset we obtain a temperature of $T/T_F = 0.14 \pm 0.02$, where the Fermi temperature T_F is calculated from T and μ_0 using $T_F = T \log[1 + \exp(\beta\mu_0)]$ ⁴².

We validate these measurements by plotting the dimensionless quantity $n_{2D,\uparrow}\lambda_{dB}^2$ as a function of $\beta\mu$ for each of the different systems (Fig. 6.2(c)) [147]. The different datasets all collapse onto a single curve and are in excellent agreement with the theoretical expectation.

6.3 Observation of Pauli blocking in the momentum distribution

We now go beyond this local probing of density and chemical potential by performing a direct measurement of the momentum distribution of an ideal 2D Fermi gas. We achieve this by mapping the momentum distribution to real space using matter wave focusing [63, 148–150]: We switch off the radial confinement provided by the ring potential and let the system evolve for a time t in a weak harmonic potential in radial direction. After a time-evolution of a quarter of the

⁴² This equation is found by solving the 2D EOS for μ_0 , taking the $T = 0$ limit, yielding $T_F = n_{2D,\uparrow} 2\pi\hbar^2 / (mk_B)$ and reinserting the EOS for $n_{2D,\uparrow}$

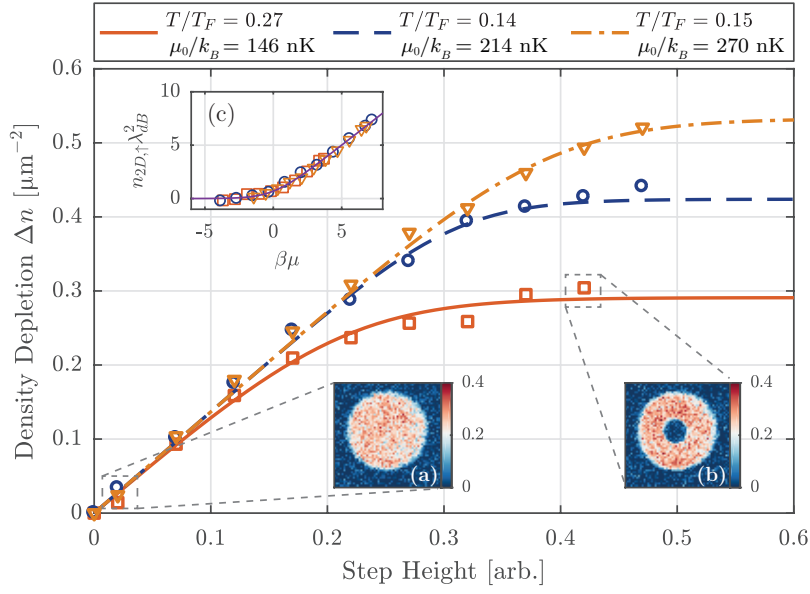


Figure 6.2: Density EOS for non-interacting homogeneous 2D Fermi gases: The EOS is mapped out for different densities and temperatures by imprinting a repulsive potential step onto the atoms. This causes a density depletion Δn in the center of the cloud (a,b). Measuring this density depletion Δn as a function of the step height directly yields the density EOS of the system. By fitting the data with the EOS of a non-interacting Fermi gas we extract the temperature T and chemical potential μ_0 for each dataset. The higher T/T_F for the dataset having the lowest density in the outer ring (red squares) is most likely due to a reduced evaporation efficiency. Using the fit results for T and μ to rescale the data and plotting the dimensionless quantity $n_{2D,\uparrow} \lambda_{dB}^2$ causes the different datasets to collapse onto a single curve (c). The data shows excellent agreement with the prediction for a non-interacting 2D Fermi gas (solid purple line).

radial trap period $\tau = 2\pi/\omega_r$, all particles with momentum $\hbar\vec{k}$ have moved to a position $\vec{r} = \hbar\vec{k}/m\omega_r$. Hence, the momentum distribution $\tilde{n}(\vec{k})$ can be directly extracted from the density distribution $n(\vec{r}, t)$ at $t = \tau/4$ via $\tilde{n}(\vec{k}) = (\hbar/m\omega_r)^2 \cdot n(\vec{r} = \hbar\vec{k}/m\omega_r, \tau/4)$ (Fig. 6.3(b,e,h)).

This technique can also be extended to perform matter wave imaging instead of matter wave focusing by letting the system evolve for $t = \tau/2$ instead of $t = \tau/4$ ⁴³. This causes the initial density distribution to reappear inverted around the center of the trap, i.e. $n(\vec{r}, \tau/2) = n(-\vec{r}, 0)$. Comparing the matter wave imaged distribution at $t = \tau/2$ with the initial distribution provides a measure for the quality of the matter wave lens formed by the radial potential, which can be affected by anharmonicities of the potential. For our experiments, we set the radial magnetic trap frequency to a value of $\omega_r = 2\pi \cdot (33.3 \pm 0.5)$ Hz and ramp down the depth of the z-confinement by a factor of five to minimize the influence of its anti-trapping potential while keeping the atoms in the depth of field. We find that the in situ and matter wave imaged density distributions are virtually indistinguishable (Fig. 6.3(a,c,i)), which shows that for this non-interacting system, our matter wave focusing gives an accurate measurement of the momentum distribution.

To extract the occupation $f(\vec{k}) = A_k \cdot \tilde{n}(\vec{k})$ from the momentum distribution $\tilde{n}(\vec{k})$, we use the k-space area $A_k = 16\pi/D^2$ of a single k-mode in a box potential with diameter D. This allows us to directly observe Pauli blocking in our non-interacting Fermi gas, which manifests itself in a unity occupation of k modes around $k = 0$, followed by a drop in the occupation at the Fermi wave vector k_F (Fig. 6.3(j)).

Next, we quantitatively determine the chemical potential and the temperature of the gas by fitting our data with the Fermi distribution

$$f(k) = \frac{\zeta}{1 + \exp\left[\beta\left(\frac{\hbar^2 k^2}{2m} - \mu_0\right)\right]}.$$

The free parameters of the fit are the temperature T, the chemical potential μ_0 and an overall amplitude ζ which accounts for systematic errors in the determination of $\tilde{n}(\vec{k})$ and A_k . The fit is in excellent agreement with the data (Fig. 6.3(j)) and yields a chemical potential $\mu_0 = k_B(148.8 \pm 2.6)$ nK, a temperature $T = (46.7 \pm 2.2)$ nK and $\zeta = 1.05 \pm 0.06$, where the errors denote 1 σ -confidence intervals of the fit. The dominant sources of systematic errors on the amplitude of $f(k)$ are the 2% uncertainty of the radial trap frequency ω_r , the 7% uncertainty in the density calibration and the 4% uncertainty in the determination of the ring diameter D from the in situ images. The fit results translate to $T/T_F = 0.31 \pm 0.02$, $\mu_0/\hbar\omega_z = 0.250 \pm 0.005$, and a Fermi wave vector $k_F = (1.93 \pm 0.02)$ μm^{-1} . This is in very good agreement both with the Fermi wave vector deduced from the mean density $k_{F,\tilde{n}} = \sqrt{4\pi\tilde{n}_{2D,\uparrow}} = (1.86 \pm 0.08)$ μm^{-1} and the temperature and chemical potential obtained for a similar evaporation depth in the EOS measurement shown in Fig. 6.2 (red solid line)⁴⁴. We note that the fitted temperature is an upper bound, affected by fluctuations in the particle number and the inhomogeneity of the density distribu-

⁴³ In our case this imaging has a magnification of 1. Other magnifications are accessible by switching to a different radial trap frequency after the $\tau/4$ point.

⁴⁴ We chose a low evaporation depth, despite the fact that we achieve our lowest T/T_F at higher Fermi energies, since we want k_F to be small enough that the full momentum distribution is captured by the field of view of the imaging system.

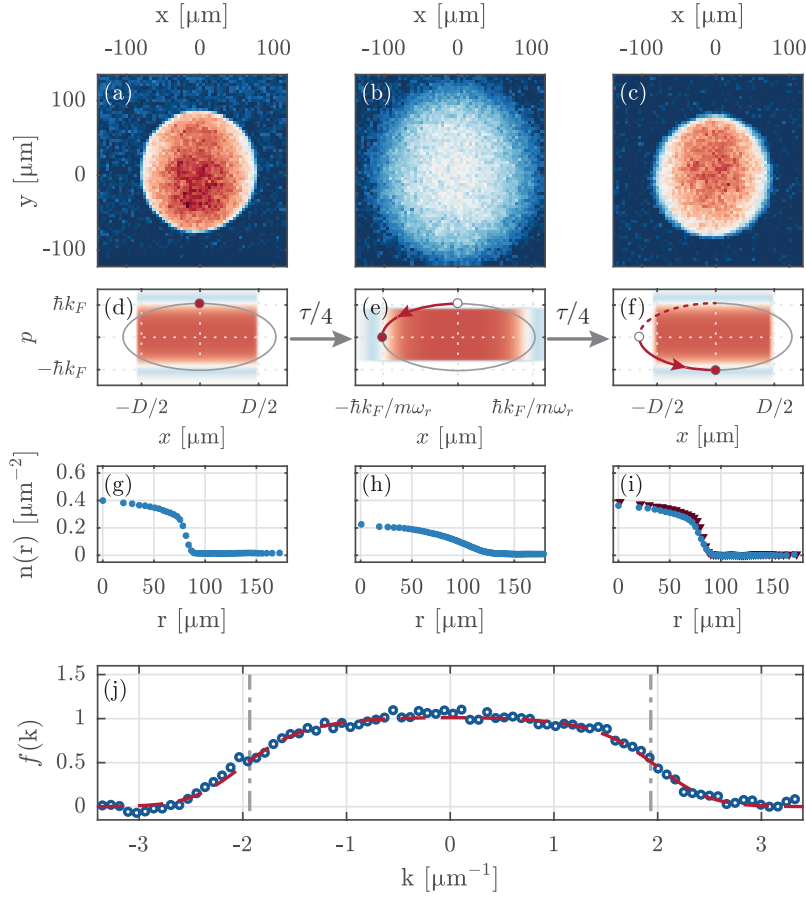


Figure 6.3: Momentum distribution of a non-interacting 2D Fermi gas: To measure the momentum distribution, we switch off the confining ring potential and let the gas evolve in a weak harmonic potential. A free time evolution t for a quarter of the trap period τ performs a rotation in phase space by 90° as sketched in (d,e), causing the momentum distribution of the gas to be mapped into real space. Averaged images (51 - 62 realizations) and corresponding azimuthal averages of the density and momentum distribution are shown in (a,b) and (g,h) respectively. After a free time evolution of half a trap period, the in situ density distribution is mapped back to real space (c); the azimuthal averages at $t = 0$ (red triangles) and $t = \tau/2$ (blue dots) are almost identical (i). A diagonal cut through the momentum distribution (b) reveals the occupation $f(k)$ of the system (j), which shows close to unity occupation around $k = 0$ and drops off at the Fermi wave vector $k_F = (1.93 \pm 0.02) \mu\text{m}^{-1}$ (gray dash dotted lines). A fit with a Fermi distribution (red dashed line) yields a temperature of $T/T_F = 0.31 \pm 0.02$.

tion, which is smaller than 11 % of the mean density. This value includes both the actual density inhomogeneity due to the presence of the harmonic potential used for the matter wave focusing and artifacts due to imperfections of the imaging beam.

When measuring the momentum distribution for varying densities, see Fig. 6.4(a), we observe that the occupation at low momenta saturates to values close to unity for densities ranging from $0.25 \mu\text{m}^{-2}$ to $0.5 \mu\text{m}^{-2}$. This clearly shows Pauli blocking in momentum space [114].

6.4 Measuring $\tilde{n}(\mathbf{k})$ of interacting homogeneous 2D Fermi gases

Finally, we realize an interacting homogeneous 2D Fermi gas close to a broad Feshbach resonance [151] and apply matter wave focusing. We prepare a single-layer attractive 2D Fermi gas at $B = 1020 \text{ G}$ where the ratio of scattering length $a_{3\text{D}}$ to harmonic oscillator length $l_z = \sqrt{\hbar/m\omega_z}$ is $a_{3\text{D}}/l_z = -0.56$. In contrast to previous experiments which measured the pair momentum distribution by converting pairs into deeply-bound molecules [63], we measure the momentum distribution of the individual atoms [152]. This requires a negligible influence of collisions on the time evolution. We achieve this by releasing the gas from the vertical confinement [153, 154] as well as flashing on a light pulse propagating along the z -direction which rapidly ejects atoms in state $|\uparrow\rangle$ [114, 155, 156]. This projects the wave function of atoms in state $|\downarrow\rangle$ onto free particle states and allows us to extract the occupation $f(\mathbf{k})$ of the interacting system using the matter wave focusing technique described above. For our interaction strength, we expect only small deviations in $f(\mathbf{k})$ compared to the non-interacting system since at $T = 0$ the quasiparticle weight Z and the gap Δ are calculated to be $Z \approx 0.9$ [157] and $\Delta \approx 21\%$ [158]. We therefore attribute the reduced central occupation and the broadening of the momentum distribution shown in Fig. 6.4(e) to thermal excitations.

Summary and conclusion

In this chapter, we report on the realization of a homogeneous 2D Fermi gas trapped in a box potential. We locally probe the system by imprinting a step potential using a DMD and thereby measure the EOS of a non-interacting Fermi gas. Furthermore, we apply matter wave focusing to directly observe Pauli blocking in the momentum distribution of a non-interacting 2D Fermi gas. Finally, we demonstrate that the momentum distribution of interacting gases can also be measured and observe a momentum distribution that is qualitatively similar to that of a non-interacting gas for intermediate interactions.

The homogeneous systems presented in this chapter are particularly useful for studying non-equilibrium dynamics of strongly correlated systems, since they allow interaction quenches without triggering mass redistribution, which is unavoidable in harmonic traps. The

combination of such a homogeneous system with non-local probes is ideally suited to observe critical phenomena and exotic phases such as FFLO superfluidity, which are predicted to exist only in narrow regions of the phase diagram. Finally, our measurement of the momentum distribution of an interacting Fermi gas can be extended to analyse momentum correlations [159] and thereby observe Cooper pairs in a fermionic superfluid.

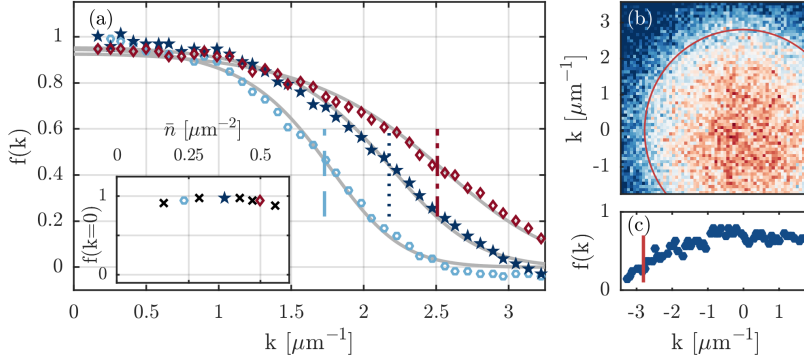


Figure 6.4: Saturation in the occupation of momentum states. The occupation $f(k)$ of non-interacting Fermi gases with in-situ densities of $\bar{n} = 0.24 \mu\text{m}^{-2}$ (light blue hexagons), $0.38 \mu\text{m}^{-2}$ (dark blue stars) and $0.50 \mu\text{m}^{-2}$ (red diamonds) is shown in (a). For low momenta we find a near unity occupation that is independent of the in-situ density (see inset) which is direct evidence of Pauli blocking. The Fermi wave vectors deduced from Fermi fits to the distribution agree well with the $k_{F,\bar{n}} = \sqrt{4\pi\bar{n}_{2D,\uparrow}}$ (vertical lines) calculated from the in-situ density. An image of the momentum distribution of an attractively interacting Fermi gas is shown in panel (b) and a cut through the distribution in panel (c). The Fermi momentum $k_{F,\bar{n}}$ for a non-interacting gas with equal density is indicated by the red circle (b) and the vertical red line (c), respectively.

Part III

AN IDEAL JOSEPHSON JUNCTION IN AN ULTRACOLD
TWO-DIMENSIONAL FERMI GAS

In the following part, I present the main result of this thesis: The first realisation of a Josephson junction in a 2D Fermi gas.

In chapter 7, I will first review the fundamentals of Josephson junctions and provide an overview of experimental realisations from solid state systems to superfluid helium and ultracold quantum gases. In chapter 8, we present our observation of Josephson oscillations in a 2D Fermi gas and show that these Josephson oscillations can be quantitatively understood in an LC oscillator circuit model. In chapter 9, we use this circuit model to probe the current phase relation of our junction and observe the sinusoidal relation $I(\phi) = I_C \sin(\phi)$ of an ideal Josephson junction. Finally, in chapter 10, we show that Josephson oscillations persist in the entire crossover from weakly bound Cooper pairs to strongly bound bosonic dimers and extract the critical current I_C as a novel in-situ probe for the superfluid order parameter in such a two-dimensional quantum gas.

The results presented in chapters 8 to 10 are adopted from

N. Luick, L. Sobirey, M. Bohlen, V.P. Singh, L. Mathey, T. Lompe, and H. Moritz

arXiv:1908.09776 (2019), accepted for publication in Science.

and reprinted here with modifications and additions.

7 | THEORETICAL AND EXPERIMENTAL BACKGROUND OF JOSEPHSON JUNCTIONS

The theory of quantum mechanics revolutionised our understanding of nature by introducing the complex wave function Ψ as the fundamental entity to describe our world on a microscopic scale. While often this wave nature of matter is masked beyond the microscopic level due to loss of coherence, there exist phenomena where quantum effects become apparent even on a macroscopic scale.

One of the most striking macroscopic manifestations of quantum mechanics is the Josephson effect [160, 161], where a current between two superconductors can flow without any applied voltage. In this chapter, I will explain the origin for the Josephson effect and show how it can be realised in a variety of different systems ranging from superconductors to superfluid helium and superfluid quantum gases (s. Fig. 7.1).

7.1 Superconducting Josephson junctions

7.1.1 The Josephson effect: fundamental equations

The fundamental origin for the Josephson effect is the intrinsic phase coherence of superconductors. When a superconductor is cooled below its critical temperature, phase fluctuations are significantly suppressed and a quantum state $\Psi_1 = \sqrt{n_1}e^{i\phi_1}$ with a well-defined phase ϕ_1 emerges, where the amplitude is determined by the condensate density n_1 .

For a *single* superconductor, this phase is an elusive quantity whose specific value leaves $|\Psi_1|^2$ unchanged and therefore has no measurable effect. However, when *two* superconductors are weakly linked to form a Josephson junction, the phase becomes accessible because a difference $\phi = \phi_1 - \phi_2$ between their phases ϕ_1 and ϕ_2 results in a particle current $I(\phi)$ (s. Fig. 7.2). For an ideal Josephson junction this current phase relation takes a sinusoidal form

$$I = I_c \sin(\phi), \quad (7.1)$$

where I_c is the maximal supercurrent that can flow across the junction which is determined by the wave function overlap.⁴⁵ In addition, the phase difference across the junction can be controlled by the applied voltage U

$$U = \frac{\hbar}{2e} \frac{\partial}{\partial t} \phi. \quad (7.2)$$

Equations 7.1 and 7.2 are the fundamental equations that govern the current-voltage characteristics of Josephson junctions as illustrated in

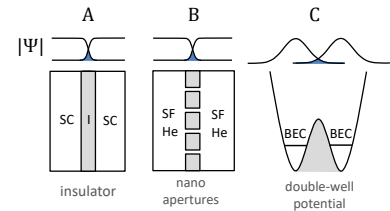


Figure 7.1: Universal Josephson effect. The Josephson effect occurs in a variety of different systems when two quantum states Ψ overlap (blue shaded region). Examples include superconductor-insulator-superconductor junctions (A), nano-apertures coupling two superfluid Helium reservoirs (B) and bosonic Josephson junctions realized by a BEC in a double-well potential (C). These system are discussed in this chapter in section 7.1 (A), 7.2 (B) and 7.3.1 (C).

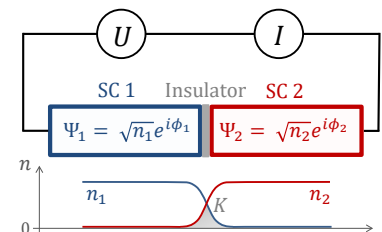


Figure 7.2: A typical superconducting Josephson junction is formed by two superconductors SC1 and SC2 which are separated by a thin insulating material which forms a tunnelling barrier. The wave functions of both superconductors overlap and give rise to a current $I(\phi)$ which is driven by the phase difference $\phi = \phi_1 - \phi_2$ between the superconductors. For an ideal Josephson junction, this current phase relation takes a sinusoidal form $I(\phi) = I_c \sin(\phi)$, where the critical current $I_c \propto K$ is determined by the coupling energy K .

⁴⁵ For a basic derivation of eq. 7.1 and 7.2 see extra 7.1.

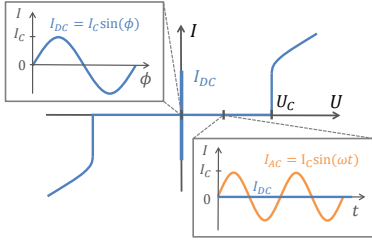


Figure 7.3: Current-voltage characteristics of an ideal Josephson junction.

Fig. 7.3.

- For a vanishing applied voltage $U = 0$, a constant phase difference $\phi(t) = \phi_0$ between the two superconductors is maintained which results in a DC current $I_{DC} = I_c \sin(\phi_0)$ between the two superconductors (*DC Josephson effect*).
- For a small non-zero voltage $U > 0$, the phase difference increases linearly with time $\phi(t) = \phi_0 + \frac{2eU}{\hbar}t$ which gives rise to an AC current $I_{AC} = I_c \sin(\omega t)$ oscillating with a frequency of $\omega = 2eU/\hbar$, while the DC component $I_{DC} = \langle I \rangle_t$ vanishes (*AC Josephson effect*).
- Only when the voltage (current) exceeds some critical value U_c (I_c), a resistive current channel opens which leads to an additional voltage drop $U = RI$ over the junction. For a BCS superconductor the critical voltage $U_c \approx 2\Delta$ is determined by the gap Δ .

Extra 7.1: Derivation of the ideal Josephson equations

The dynamics of an ideal Josephson junction (s. Fig. 7.2) are described by the coupled equations

$$i\hbar \frac{\partial}{\partial t} \Psi_1 = E_1 \Psi_1 + K \Psi_2 \quad (7.3)$$

$$i\hbar \frac{\partial}{\partial t} \Psi_2 = E_2 \Psi_2 + K \Psi_1 \quad (7.4)$$

where Ψ_1 (Ψ_2) is the wave function of superconductor 1 (2) with energy E_1 (E_2) and K is the tunnelling energy determined by the wave function overlap. To derive the ideal Josephson equations 7.1 and 7.2 from these equations we describe both superconductors with complex numbers

$$\Psi_{1,2} = \sqrt{n_{1,2}} \exp(i\phi_{1,2}),$$

where $n_{1,2}$ is the condensate density and $\phi_{1,2}$ is the phase of each superconductor. Using

$$\frac{\partial}{\partial t} \Psi = \frac{1}{2\sqrt{n}} \frac{\partial n}{\partial t} e^{i\phi} + i\sqrt{n} e^{i\phi} \frac{\partial \phi}{\partial t} \quad (7.5)$$

$$= \Psi \left(\frac{1}{2n} \frac{\partial n}{\partial t} + i \frac{\partial \phi}{\partial t} \right) \quad (7.6)$$

we can rewrite eq.7.3 and eq.7.4 as

$$i\hbar \frac{1}{2n_1} \frac{\partial n_1}{\partial t} - \hbar \frac{\partial \phi_1}{\partial t} = E_1 + K \frac{\Psi_2}{\Psi_1} \quad (7.7)$$

$$i\hbar \frac{1}{2n_2} \frac{\partial n_2}{\partial t} - \hbar \frac{\partial \phi_2}{\partial t} = E_2 + K \frac{\Psi_1}{\Psi_2} \quad (7.8)$$

The imaginary part of these equations yields the change in density

$$\frac{\partial n_1}{\partial t} = \frac{2Kn_1}{\hbar} \text{Im} \left(\frac{\Psi_2}{\Psi_1} \right) \quad (7.9)$$

$$= \frac{2Kn_1}{\hbar} \text{Im} \left(\frac{\sqrt{n_2} e^{i\phi_2}}{\sqrt{n_1} e^{i\phi_1}} \right) \quad (7.10)$$

$$= \frac{2K}{\hbar} \sqrt{n_1 n_2} \sin(\phi_2 - \phi_1) \quad (7.11)$$

$$= -\frac{\partial n_2}{\partial t}, \quad (7.12)$$

which using the density $n = n_1 \approx n_2$ and the total current $I = V \partial n / \partial t$ can be expressed as the current phase relation

$$I = I_c \sin \phi, \quad (7.13)$$

where $I_c = 2KnV/\hbar$, $\phi = \phi_2 - \phi_1$ and V is the volume of each superconductor.

The real part of the difference between eq. 7.7 and 7.8 yields

$$\hbar \frac{\partial}{\partial t} \phi = E_1 - E_2, \quad (7.14)$$

which reproduces eq. 7.2 using the voltage $U = (E_1 - E_2)/2e$ between the superconductors.

7.1.2 Technological applications

Josephson junctions are a unique experimental tool at the interface between electronics and quantum mechanics which enable a wide range of applications from fundamental research to the creation of novel quantum devices. Here, I will summarize some of most striking applications of superconducting Josephson junctions and introduce their property as a nonlinear circuit element which provides the framework to understand the dynamics of our Josephson junction in a 2D Fermi gas.

Josephson voltage standard

The fundamental goal of metrology is to define the basic physical units in terms of quantities that can be measured to a high precision. The direct connection between voltage U and frequency $\omega = 2eU/\hbar$ of Josephson junctions provides the basis for such a definition of the unit *volt*.

The Josephson voltage standard is based on the inverse AC Josephson effect, where an externally applied RF voltage $U(t) = U_{DC} + U_{AC} \cos(\omega t)$ results in a DC current at specific multiples $U_{DC} = n\omega\hbar/2e$ (s. extra 7.2). Since the voltage spacing between these current steps is determined only by the applied frequency and the fundamental Josephson constant $K_J = 2e/h = 4.835 \cdot 10^{14} \text{ Hz/V}$, it serves as a robust definition for the voltage as specified in [165].

Since for commonly used RF frequencies on the order of 100 GHz the current steps are separated by only $\sim 0.2 \text{ mV}$, the first single junction voltage references were limited to small voltages on the order of $U_{DC} \sim 1 \text{ mV}$ [166]. This issue could be solved by connecting ~ 1000 junctions in series, which enabled to generate voltages on the order of 1 V as first demonstrated in [164] (s. Fig. 7.4).

Extra 7.2: Driven Josephson junctions

For an externally applied AC voltage $U(t) = U_{DC} + U_{AC} \cos(\omega t)$, the phase according to eq. 7.2 advances as

$$\phi(t) = \phi_0 + \frac{2eU_{DC}}{\hbar}t + \frac{2eU_{AC}}{\hbar\omega} \sin(\omega t). \quad (7.15)$$

Using the Bessel functions of the first kind J_n , the corresponding current $I(\phi(t)) = I_c \sin(\phi(t))$ can be expressed as

$$I = I_c \sum_{n=-\infty}^{\infty} (-1)^n J_n \left(\frac{2eU_{AC}}{\hbar\omega} \right) \sin \left(\phi_0 + \frac{2eU_{DC}}{\hbar}t - n\omega t \right)$$

which yields a DC current when $U_{DC} = n\omega\hbar/2e$.

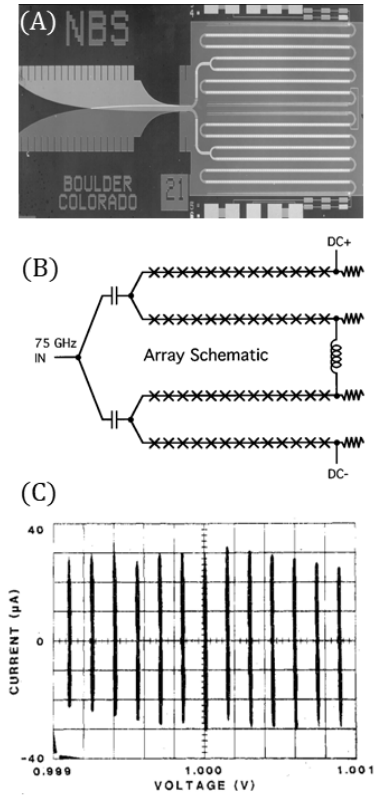


Figure 7.4: (A) Image of an array of 3020 Josephson junctions developed at NIST to generate a voltage of 1 volt [162]. (B) Schematic illustration of the voltage standard. A GHz frequency ω is applied to a series of Josephson junctions to generate constant voltage steps $U_{DC} = n\omega\hbar/2e$ (adapted from [163]). (C) First 1 V Josephson voltage standard for a drive frequency of $\omega = 2\pi \times 72.13506 \text{ GHz}$ for constant voltage steps around $n = 6704$ [164].

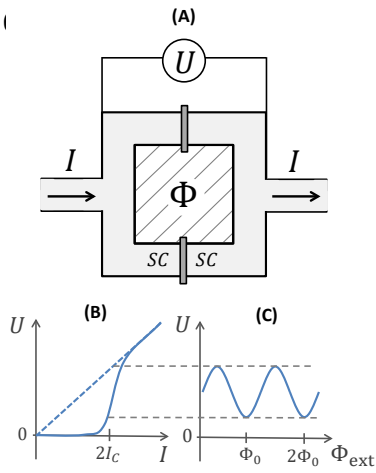


Figure 7.5: Basic principle of a SQUID magnetometer. (A) Schematic of a SQUID. (B) The current-voltage characteristics depends on the applied magnetic flux Φ_{ext} . For $\Phi_{\text{ext}} = n\Phi_0$ the maximal supercurrent is $I_{\text{max}} \sim 2I_c$ (blue solid line), while for $\Phi_{\text{ext}} = (n + 1/2)\Phi_0$ I_{max} is reduced to zero (blue dashed line). (C) Hence, for a current bias of $I = 2I_c$, changes in the external flux Φ_{ext} lead to an oscillation of the voltage U with a period Φ_0 .

Highly-sensitive magnetometers

An important application of Josephson junctions are SQUIDs (*superconducting quantum interference devices*) [167], which enable extremely precise measurements of magnetic fields and thereby provide the basis for various applications ranging from medical imaging [168] to fundamental tests of general relativity [169].

The basic geometry for a DC SQUID is a superconducting loop which encloses a quantised magnetic flux $\Phi = n\Phi_0$ and is split by two Josephson junctions (s. Fig. 7.5). The key idea behind fabricating a magnetometer with such a SQUID is that small changes in an additional externally applied magnetic flux Φ_{ext} have a dramatic influence on its current-voltage characteristics (s. extra 7.3). While for integer multiples of the magnetic flux quantum $\Phi_{\text{ext}} = n\Phi_0$ the maximal supercurrent supported by the SQUID is given by $I_{\text{max}} = 2I_c$, for $\Phi_{\text{ext}} = (n + 1/2)\Phi_0$ the maximal supercurrent vanishes $I_{\text{max}} = 0$. Therefore, when applying a current bias $I_b \approx 2I_c$ to the SQUID the voltage U across the junction oscillates with a period Φ_0 which can be used to precisely determine the applied magnetic field.

Extra 7.3: Current-Voltage characteristics of a SQUID

The dependence of the current-voltage characteristics of the SQUID on the applied flux Φ_{ext} is the result of flux quantisation in combination with the current-phase relation $I(\phi) = I_c \sin(\phi)$ of both Josephson junctions. The magnetic flux inside the loop is quantised to $\Phi = n\Phi_0$ because the single-valuedness of the wave function requires that the phase around the loop can only change by multiples of 2π . Therefore, for a small applied external flux $\Phi_{\text{ext}} < \Phi_0/2$, a screening current inside the loop develops to cancel this external flux and maintain $\Phi = 0$ as required by flux quantisation. When this external flux is increased to $\Phi_{\text{ext}} = \Phi_0/2$, the screening current around

the loop corresponds to a total phase change of $\Delta\phi = \pi$ around the loop and therefore a phase drop of $\pi/2$ over each junction. Hence, the screening current inside the loop equals the maximal supercurrent I_c of each junction. Therefore, any externally applied current has to flow resistively across the SQUID and the maximal supercurrent of the SQUID is reduced to $I_{\text{max}} = 0$ from its maximal value of $I_{\text{max}} = 2I_c$ without any applied field. For larger applied flux $\Phi_{\text{ext}} > \Phi_0/2$, the superconducting screening current cannot maintain a zero-flux state and therefore changes direction and continues to maintain higher flux quanta $\Phi = n\Phi_0$ inside the loop.

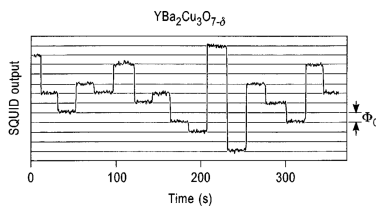


Figure 7.6: Observation of flux quantisation in cuprate superconductors. When an RF SQUID magnetometer made of YBCO was periodically exposed to electromagnetic noise, the magnetic flux was observed to jump between integral numbers of the flux quantum $\Phi_0 = h/2e$. Adapted from [31].

Probing the nature of high-temperature superconductors

Due to their unique intrinsic sensitivity to the phase of the superconducting order parameter, Josephson junctions have served as vital tool for our understanding of high-temperature superconductors.

By fabricating a SQUID with YBCO, flux quantisation to multiples of $\Phi_0 = h/2e$ was observed which clearly demonstrated that the charge carriers of such cuprate superconductor are electron pairs like in conventional BCS type superconductors [31]. Moreover, Josephson junction provided unambiguous evidence for a d-wave order parameter in cuprate superconductors [7, 170]. While ARPES measurements (s. Fig. 7.7) could already provide strong evidence for a strongly

anisotropic pairing gap $\Delta(\mathbf{k})$ approaching zero along the $(k_x, k_x, k_z) = (1, 1, 0)$ -direction [171], such experiments were only sensitive to the amplitude of the superconducting order parameter and therefore could not reveal the characteristic sign change of the proposed $d_{x^2-y^2}$ order parameter.

The fabrication of Josephson junctions connecting cuprate superconductors enabled the first phase-sensitive measurements of the order parameter of high-temperature superconductors [29, 32]. In these measurements, cuprates were connected under a certain relative rotation to each other to provide directional information about the pairing gap $\Delta(\mathbf{k})$.⁴⁶ One of the most direct evidence for the d-wave order parameter was provided by measurements of the critical current in single corner Josephson junctions with an L-shaped tunneling barrier geometry (s. Fig. 7.8) [29]. While for a conventional s-wave symmetry this corner geometry does not affect the critical current, the d-wave symmetry introduced an additional phase shift of π along the loop, which could be directly observed as a vanishing critical current of the junction without any externally applied magnetic field.

Extra 7.4: The nonlinear Josephson inductance

As a prerequisite for the following section, I show that the nonlinear current phase relation $I(\phi)$ of a Josephson junction corresponds to a nonlinear inductance

$$L_J(\phi) = \frac{\hbar}{2e} \frac{1}{\partial I / \partial \phi}. \quad (7.16)$$

The time derivative of the current is given by

$$\dot{I}(\phi) = \frac{\partial I}{\partial \phi} \dot{\phi}, \quad (7.17)$$

which using eq. 7.2 corresponds to a voltage drop

$$U = \frac{\hbar}{2e} \dot{\phi} = \frac{\hbar}{2e} \frac{1}{\partial I / \partial \phi} \dot{I}. \quad (7.18)$$

which reproduces eq. 7.16 using $U = L_J \dot{I}$ to define the Josephson inductance L_J . In particular, for an ideal Josephson junction $I(\phi) = I_c \sin(\phi)$ we get

$$L_J(\phi) = \frac{\hbar}{2e I_c \cos(\phi)}. \quad (7.19)$$

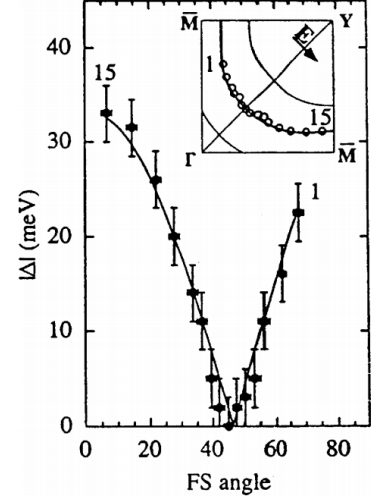


Figure 7.7: ARPES measurement of the superconducting gap in Bi2212. Shown is the measured amplitude of the gap $|\Delta|$ in dependence of the angle to the Fermi surface (FS). The ARPES data is in excellent agreement with a fit using a d-wave order parameter (solid line), but cannot resolve the expected sign change of Δ at an angle of 45° . Adapted from [171].

⁴⁶ Since tunnelling is exponentially suppressed at large distances, the Josephson dynamics is dominated by transport orthogonal to the tunneling barrier and therefore yields directional information.

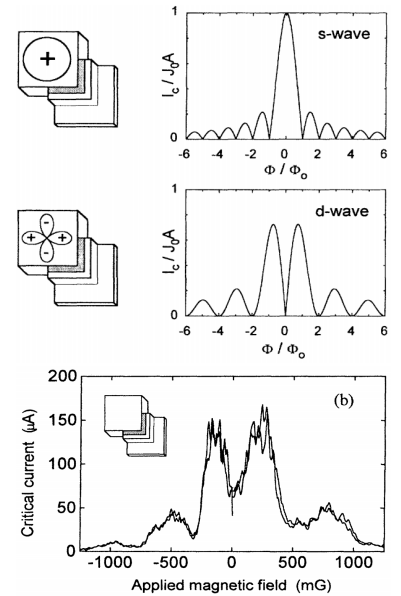


Figure 7.8: Evidence for the d-wave order parameter in YBCO. In contrast to the ARPES measurement shown in Fig. 7.7, a Josephson junction can provide phase sensitive information about the superconducting gap Δ . Using a corner junction geometry, the critical current was observed to have minimum at zero applied magnetic field (lower panel) which yields unambiguous evidence for a d-wave order parameter. Adapted from [29].

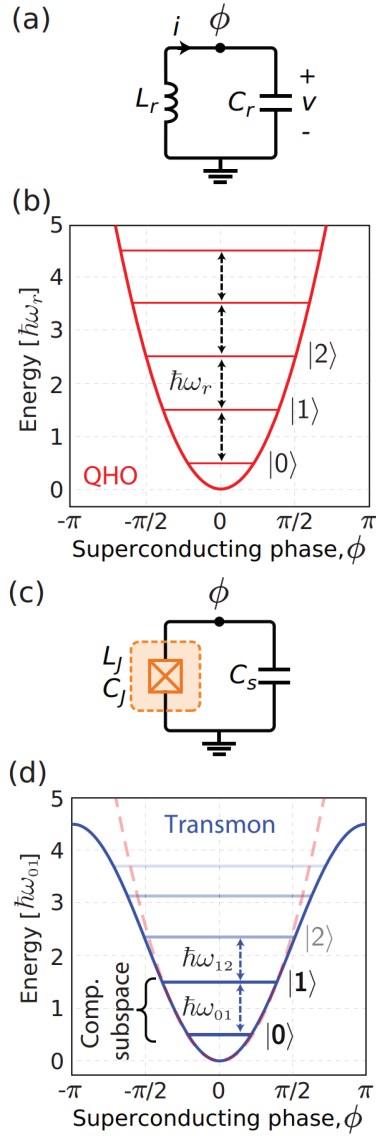


Figure 7.9: Transmon qubits: a non-linear LC oscillator. (a,b) A quantum harmonic oscillator (QHO) circuit formed by a linear inductance L_r connected in series with a capacitance C_r results in equidistant energy levels separated by $\hbar\omega_r$, where $\omega_r = 1/\sqrt{L_r C_r}$. (c,d) Replacing L_r in (a) with a nonlinear Josephson inductance L_J and capacitance C_s lifts the degeneracy of the energy level spacings. This enables individually addressing the $|0\rangle \rightarrow |1\rangle$ transition, which forms the qubit. Adapted from [172].

The nonlinear Josephson inductance: basis for superconducting qubits

Most of the currently regained interest of the scientific community in the fundamental physics of Josephson junctions originates from its potential as a building block to construct a scalable universal quantum computer. While such a quantum computer would be a major scientific revolution with the prospect of efficiently simulating quantum many body systems, the experimental realisation of such a device is technologically extremely challenging.

In contrast to classical computers which are based on bits, quantum computers are based on qubits, described by a coherent superposition state $|\Psi\rangle = \alpha|0\rangle + \beta|1\rangle$ of a two-level system. One of the biggest challenges in building a quantum computer is the realisation of a system with many qubits while ensuring sufficiently long coherence times.

One of the currently most successful approaches to realise such a scalable qubit with long coherence times is the *transmon*, which was originally proposed in [173] and very recently used in the claimed achievement of quantum supremacy using 53 qubits [174].

A transmon qubit can be understood as a nonlinear LC oscillator circuit, which is formed by the nonlinear inductance $L_J(\phi)$ of a Josephson junction and a shunt capacitance C (s. Fig. 7.9). While for a linear inductance L_r such an oscillator circuit would yield equidistant energy levels separated by $\hbar\omega = 1/\sqrt{L_r C}$ (s. Fig. 7.9 a,b), the nonlinearity of the Josephson inductance lifts this degeneracy and thereby enables a specific addressing of the $|0\rangle \rightarrow |1\rangle$ transition, which forms the qubit (s. Fig. 7.9 c,d). More specifically, the Josephson inductance of an ideal junction $L_J(\phi) = \hbar/(I_c \cos(\phi))$ increases for large phases ϕ across the junction in direct correspondence to the nonlinear current phase relation $L_J(\phi) = 1/(\partial I/\partial \phi)$ (s. extra 7.4).

While it is generally desirable to have a large anharmonicity, i.e. a small critical current I_c , to have a large difference between ω_{01} and ω_{12} to prevent addressing higher excited states (s. Fig. 7.9d), for an isolated junction these small currents would imply a greater sensitivity to charge noise. The transmon qubit solves this issue by introducing a large shunt capacitance C in parallel to the Josephson junction and thereby achieves an ideal compromise of an exponentially suppressed charge noise while the anharmonicity only decreases as a power law as shown in [173].

7.2 Superfluid Josephson junctions: the crossover from dissipative phase slips to coherent Josephson dynamics

The Josephson effect is a universal phenomenon that originates when two phase coherent quantum states are weakly linked and is therefore not restricted to superconducting solid state systems. Josephson junctions realised in superfluid ^4He [175] and ^3He [176] are a demonstration for this universality and clearly illustrate how the Josephson effect arises in the limit of two weakly coupled superfluids.

For the experiments described in [175], the weak link was realized with an array of ~ 4000 apertures with a diameter of $d \approx 40$ nm. While for temperatures well below the critical temperature T_c , these apertures are significantly larger than the healing length of the system, by bringing the temperature close to T_c the healing length could be increased as $\xi \propto 1/(T_c - T)^{0.67}$ to reach the weak coupling regime where $\xi \sim d$ (s. extra 7.5). Using this technique a clear transition from a linear to a sinusoidal current phase relation could be observed as the temperature was raised from $T_c - T = 27$ mK to $T_c - T = 0.8$ mK (s. Fig. 7.10). For these measurements, the current $I = dx/dt$ through the aperture was obtained by measuring the displacement $x(t)$ of a diaphragm, while the phase ϕ was reconstructed from a measurement of the pressure P and temperature T of the system.

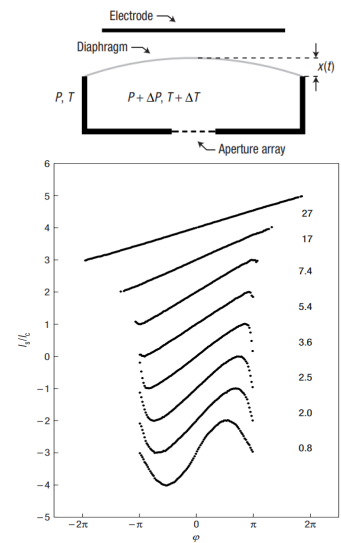
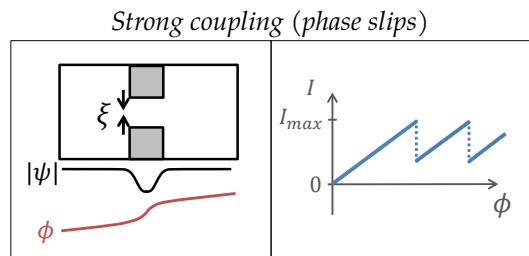
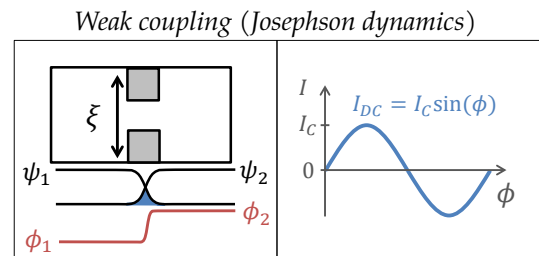


Figure 7.10: Experimental demonstration of the transition from a linear to a sinusoidal current phase relation in superfluid ^4He . Adopted from [175].

Extra 7.5: Transition from strong to weak coupling



When the healing length $\xi < d$ of the superfluid is smaller than the size of the aperture d , the amplitude of the wave function is only slightly suppressed within the constriction and the gradient of the local phase ϕ determines the local velocity $v_s = \hbar \nabla \phi / m$ which results in a linear current $I(\phi) \propto \phi$. As the phase gradient increases, v_s reaches the critical velocity v_c corresponding to $I = I_{\max}$ and a phase slip reduces the current which gives rise to a characteristic sawtooth form.



When the healing length $\xi > d$ is larger than the size of the aperture, the wave functions Ψ_1, Ψ_2 in both reservoirs are exponentially suppressed inside the aperture and the dynamics of the system are determined by the wave function overlap. In this ideal Josephson regime, the current phase relation takes a sinusoidal form $I(\phi) = I_c \sin(\phi)$. In contrast to the strong coupling regime, we obtain coherent Josephson oscillations as the phase increases and do not encounter any discontinuities in the current.

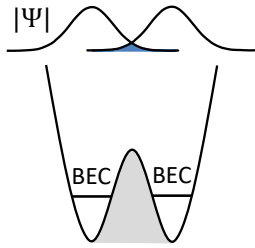


Figure 7.11: A bosonic Josephson junction realised by two weakly coupled BECs in a double-well potential.

⁴⁷ For an extensive review of experimental and theoretical aspects of bosonic Josephson junctions see [180].

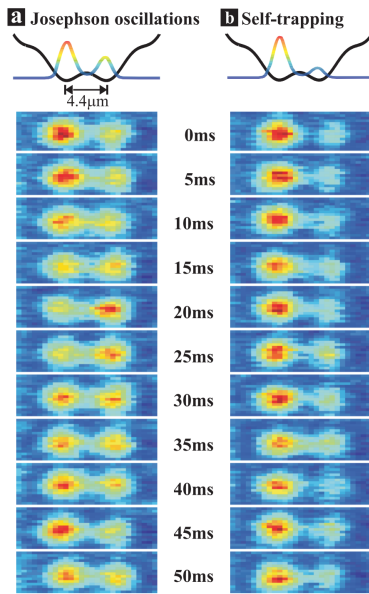


Figure 7.12: Josephson oscillations and self-trapping in a bosonic Josephson junction In the experiment presented in [182], the bosonic Josephson junction was realized with a BEC trapped in a double-well potential. (a) For small initial population differences, coherent Josephson oscillations were observed. (b) For large initial population imbalances, a novel self-trapping regime was observed in which the excess population remains trapped in the left potential well.

7.3 Cold atom Josephson junctions

More recently, Josephson junctions were realized with ultracold atoms which enabled an extensive study of the Josephson effect in novel parameter regimes due to their unique level of control over trapping geometries and interactions between particles. Here, I will briefly review these experimental realisations with ultracold Bose and Fermi gases.

7.3.1 Bosonic Josephson junctions

Well before the first realisation of BECs, it was argued that bringing two condensates close enough together to exchange particles could lead to an oscillation of atoms between the two condensates in direct analogy to a superconducting Josephson junction [177]. Following the realisation of BECs in 1995 [178, 179], such bosonic Josephson junctions⁴⁷ were eventually realised in many different geometries ranging from arrays of Josephson junctions in an optical lattice [181], to isolated double-wells [182–185] to closer analogues of solid state systems such as SQUID geometries [186]. While phase coherence between two BECs had previously been demonstrated with the striking observation of interference patterns obtained from time of flight measurements [187], these Josephson junction experiments provided a complementary in-situ demonstration of phase coherence based on coherent oscillations between trapped BECs. In contrast to their solid analogues, the dynamics of such bosonic Josephson junctions are generally significantly influenced by interactions between particles giving rise to novel self trapping regimes as predicted by Smerzi et al. [188] and first observed in [182, 189].

To understand these Josephson dynamics in cold atom systems it is instructive to consider the groundbreaking experiment presented in [182], where the Josephson junction was for the first time realized with an isolated double-well potential, in which two BECs are weakly coupled (s. Figs. 7.11 and 7.12). This experiment is well-described within a two-mode approximation, in which the the spatial form of the wave function in each well is assumed to be time-independent (s. extra 7.6). This approximation reduces the dynamics of the system to variations in the particle number $N_{1,2}(t)$ and phase $\phi_{1,2}(t)$ in each well. To initialise Josephson dynamics the authors of [182] introduced an initial population imbalance $z_0 = (N_1(0) - N_2(0))/N$, where $N = N_1 + N_2$ is the total atom number in both wells. While for a small imbalance $z \approx 0.3$, coherent oscillations in imbalance and phase could be observed (s. Fig. 7.12a), for larger imbalances $z \approx 0.6$ the population remained trapped in one of the wells (s. Fig. 7.12b).

These dynamics can be understood in direct analogy to eq. 7.1 and 7.2 introduced for the current and voltage in superconducting Josephson junctions by setting the charge $2e \rightarrow 1$ and replacing the voltage $U \rightarrow \mu$ by the difference in chemical potential $\mu = \mu_1 - \mu_2$ between the two wells. An initial population imbalance z_0 corresponds to a chem-

ical potential difference $\mu > 0$ which advances the phase difference $\phi = \phi_1 - \phi_2$ according to

$$\hbar \frac{\partial}{\partial t} \phi = \mu. \quad (7.20)$$

and introduces a current

$$I = I_c \sin(\phi). \quad (7.21)$$

For small initial imbalances $z_0 \ll z_c$ ⁴⁸, the resulting current fully inverts the population imbalance leading to harmonic Josephson oscillations with a frequency

$$\omega = \sqrt{2UNK + 4K^2}/\hbar \quad (7.22)$$

determined by the intra-well interaction parameter $U \propto \mu$ and the coupling energy $K \propto I_c$. For large initial imbalances $z_0 > z_c$, however, we encounter a qualitatively different regime where the phase difference advances so fast that the current rapidly changes direction and cannot invert the initial imbalance. In this *self-trapping* regime, the population imbalance performs small amplitude oscillations around a finite mean imbalance $\langle z \rangle \neq 0$ and the phase difference increases continuously in time. A systematic study of this crossover from coherent oscillations to self-trapping was performed in [185], where a clear reduction of the oscillation frequency ω towards z_c and the predicted increase of the oscillation frequency according to eq. 7.22 from the non-interacting Rabi limit ($\omega = 2K/\hbar$) to the plasma frequency limit⁴⁹ ($\omega = \sqrt{2UNK}/\hbar$) could be observed (s. Fig. 7.13).

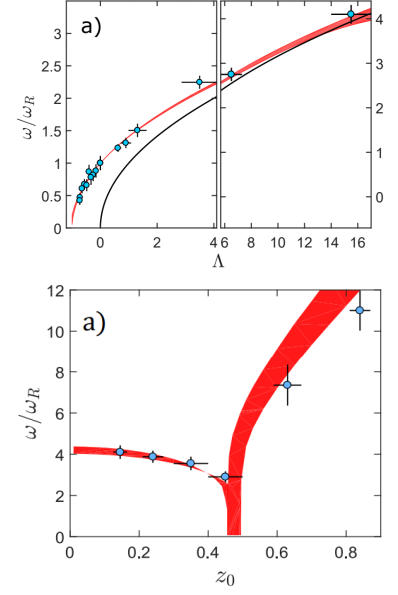


Figure 7.13: Measurement of the Josephson oscillation frequency ω normalised to the non-interacting Rabi frequency $\omega_R = 2K/\hbar$ for varying interaction strengths $\Lambda = \frac{NU}{2K}$ and initial imbalances z_0 . Adapted from [185].

⁴⁸ z_c is the critical imbalance for self-trapping which in the two-mode model is given by $z_c = \frac{2}{UN} \sqrt{2UNK - 4K^2}$ [185].

⁴⁹ The plasma frequency is given by $E_p = \sqrt{E_c E_J}/\hbar$, where $E_c \leftrightarrow U$ is the charge $E_J \leftrightarrow 2NK$ is the coupling energy.

Extra 7.6: Two-mode description of Josephson dynamics

The dynamics of bosonic Josephson junctions can be obtained from a solution of the Gross-Pitaevskii equation (GPE)

$$i\hbar \frac{\partial}{\partial t} \Psi(\mathbf{r}, t) = -\frac{\hbar^2}{2m} \nabla^2 \Psi(\mathbf{r}, t) + (V(\mathbf{r}) + g|\Psi(\mathbf{r}, t)|^2) \Psi(\mathbf{r}, t) \quad (7.23)$$

using the two-mode approximation

$$\Psi(\mathbf{r}, t) = \psi_1(t)\Phi_1(\mathbf{r}) + \psi_2(t)\Phi_2(\mathbf{r}), \quad (7.24)$$

where the time dependent amplitudes $\psi_{1,2}(t)$ in each reservoir are separated from the spatial wave functions $\Phi_{1,2}(\mathbf{r})$. In this two-mode approximation, the dynamics of the Josephson junction are described by the equations

$$i\hbar \frac{\partial}{\partial t} \psi_1 = (E_1 + U_1 N_1) \psi_1 - K \psi_2 \quad (7.25)$$

$$i\hbar \frac{\partial}{\partial t} \psi_2 = (E_2 + U_2 N_1) \psi_2 - K \psi_1 \quad (7.26)$$

where the ground state energies $E_{1,2}$, interaction energies $U_{1,2}$ and coupling energy K can be obtained from the ground state wave functions $\Phi_{1,2}(\mathbf{r})$ for isolated traps.

$$E_{1,2} = \int d^3r \left(\frac{\hbar^2}{2m} |\nabla \Phi_{1,2}|^2 + \nabla |\Phi_{1,2}|^2 V \right)$$

$$U_{1,2} = g \int d^3r (\Phi_{1,2})^4$$

$$K = - \int d^3r \left(\frac{\hbar^2}{2m} \nabla \Phi_1 \nabla \Phi_2 + \Phi_1 \Phi_2 V \right)$$

For more details see [190]. We note that eq. 7.25 and 7.26 reproduce equations 7.3 and 7.4 introduced for superconducting Josephson junctions with an additional interaction dependent term $U_{1,2} N_{1,2}$.

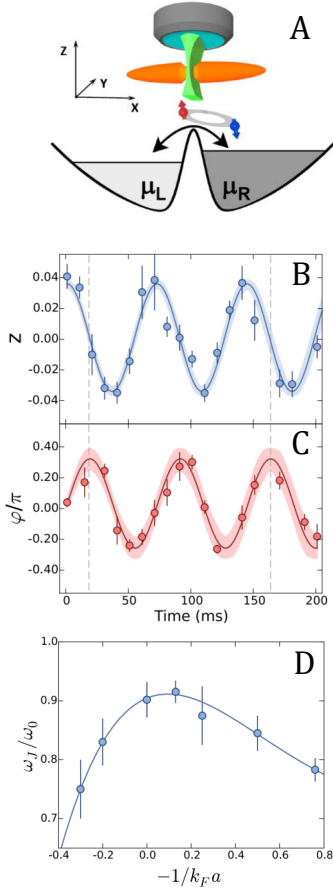


Figure 7.14: Josephson oscillations in a 3D Fermi gas in the BEC-BCS crossover. (A) Schematic of the Josephson junction in a harmonically trapped 3D Fermi gas. (B,C) Josephson oscillations in particle imbalance z (B) and phase difference ϕ (C) for an interaction parameter of $1/k_F a_{3D} \approx 4.3$. (D) Extracted oscillation frequency ω_J in the BEC-BCS crossover. Figures (A-D) adapted from [191].

⁵⁰ For large interaction strengths U , the self-trapping threshold decreases as $z_c \propto 1/\sqrt{U}$ which generally limits Josephson oscillations in the BEC-BCS crossover to very small population amplitudes $z \ll 1$.

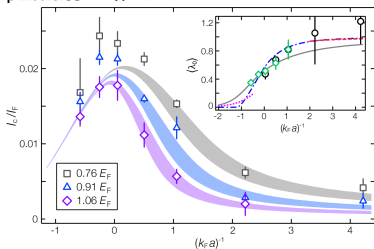


Figure 7.15: Critical current I_c and extracted condensate fraction λ_0 in the 3D BEC-BCS crossover. Figure adapted from [193].

⁵¹ While in principle the condensate fraction can also be determined from the momentum distribution $n(k)$ via time of flight measurements, such a measurement is challenging in the strongly correlated regime due to strong interactions between particles which can alter the imaged momentum distribution.

7.3.2 Fermionic Josephson junctions

More recently, Josephson oscillations were also observed in 3D Fermi gases [191, 192]. In contrast to their bosonic counterparts, such fermionic quantum gases can be used to realise superfluids from deeply bound dimers to weakly bound Cooper pairs and thereby enable a study of the Josephson effect in the entire BEC-BCS crossover. For the experiments presented in [191], the Josephson junction was realised by projecting a potential barrier with a waist of size $w \approx 2 \mu\text{m}$ onto an elongated harmonically trapped 3D Fermi gas - thereby creating two weakly coupled superfluid reservoirs (s. Fig. 7.14 A). After introducing a small initial population imbalance⁵⁰ Josephson oscillations could be observed in the population imbalance z and the phase difference ϕ between the two reservoirs (s. Fig. 7.14 B,C). The frequency ω_J of such Josephson oscillation was measured for varying values of the interaction parameter $1/k_F a_{3D}$ in the BEC-BCS crossover while keeping a constant potential height $V/E_F = 1.2$, where E_F is the Fermi energy of the gas. Most strikingly, the authors of [191] observed a maximum in ω_J close to unitarity ($1/k_F a_{3D} = 0$), which was interpreted in terms of the expected behaviour of the Josephson plasma frequency $\omega_J = \sqrt{E_C E_J}/\hbar$, where the charging energy $E_C \propto \mu$ increases and saturates towards the BCS limit while the coupling energy $E_J = KN_0$ decreases due to a vanishing condensate particle number N_0 in the BCS limit.

This direct link between the Josephson oscillation frequency and the condensate density highlights that Josephson junctions can be used as an in-situ probe for condensation in strongly correlated superfluids.⁵¹ At the time of writing of this thesis, this was experimentally demonstrated in the context of the first realisation of the DC Josephson effect in a quantum gas [193]. By dragging a potential barrier through a superfluid 3D Fermi gas at various speeds, the authors of [193] could directly extract the critical current I_c in the crossover from BEC to BCS superfluidity. As recently explained in [194], this Josephson critical current can be approximated as $I_c \propto n_c \sqrt{|\mu|} t(\mu)$, where n_c is the condensate density, μ is the chemical potential and t is the single particle tunnelling amplitude. Therefore, by calculating t and μ , the condensate density could be extracted from the measured values of I_c and the expected decrease of the condensed fraction towards the BCS limit could be observed (s. Fig. 7.15). Furthermore, by changing experimental parameters of the potential barrier, the authors of [193] verified the robustness of their extraction of the condensate density and thereby established Josephson junctions as a powerful tool to probe strongly correlated superfluid order parameters.

Two-dimensional structures are present in almost all known superconductors with high critical temperatures, but the role of the reduced dimensionality is still under debate. Recently, ultracold quantum gases have been established as ideal model systems to study such strongly correlated fermionic 2D systems [47, 72, 74, 76, 120–122, 124]. However, while pair condensation of fermions has been reported [63], fermionic superfluidity in 2D has not been directly observed. Here, we report on the first realisation of a Josephson junction in an ultracold 2D Fermi gas, which unambiguously shows phase coherence and provides strong evidence for superfluidity.

For our experiments we use a homogeneous Fermi gas of ^6Li atoms in a spin-balanced mixture of the lowest two hyperfine states, trapped in a box potential [96]. A strong vertical confinement with trap frequency $\omega_z/2\pi = 8.8(2)$ kHz ensures that the gas is kinematically 2D with the chemical potential μ and temperature T being smaller than the level spacing $\hbar\omega_z$. We create a Josephson junction by using a narrow repulsive potential barrier with a $1/e^2$ waist of $w = 0.81(6)$ μm to split the system into two homogeneous 2D pair condensates connected by a weak link (s. Fig. 8.1). We imprint a relative phase ϕ_0 between the two sides of the junction by illuminating one half of the system with a spatially homogeneous optical potential for a variable time between 0 and 20 μs . We then let the system evolve for a time t and extract the population imbalance $\Delta N = (N_L - N_R)$ and the phase difference ϕ between the two sides using either *in situ* or time of flight imaging. A typical Josephson oscillation of a molecular condensate at a magnetic field of $B = 731$ G⁵² and a barrier height of $V_0/\mu = 1.08(5)$ featuring the characteristic $\pi/2$ phase shift between imbalance and phase is shown in Fig. 8.1. The oscillations are weakly damped with a relative damping of $\Gamma/\omega = 0.07$, which according to a full numerical simulation of our system can be explained by phononic excitations in the bulk and the nucleation of vortex-antivortex pairs in the junction (Fig. 8.2).⁵³

To understand these Josephson oscillations, we use a simple circuit model commonly used to describe superconducting Josephson junctions [192, 195, 196]. In this model, we describe our junction as a nonlinear Josephson inductance L_J which is connected in series to a linear bulk inductance L_B and a capacitance C (Fig. 8.3C), where the bulk inductance L_B characterises the inertia of the gas and the capacitance C its compressibility. For vanishing Josephson inductance, the model reduces to a linear resonator with frequency $\omega_s = 1/\sqrt{L_B C} = 2\pi v_s/2l_\perp$, which corresponds to the frequency of a sound mode propagating with the speed of sound v_s across the length l_\perp of the sys-

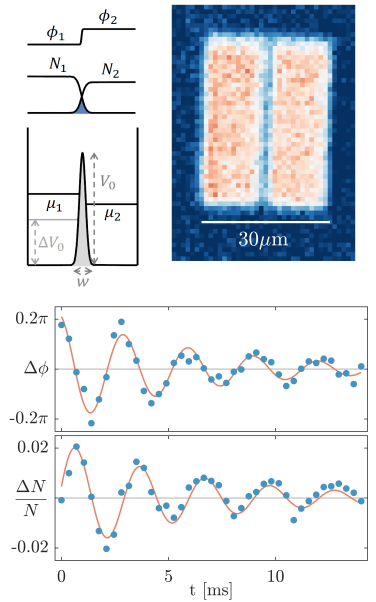


Figure 8.1: Observation of Josephson oscillations in a 2D Fermi gas. (A) Sketch of a Josephson junction consisting of two homogeneous Fermi gases with chemical potential μ_L, μ_R , particle number N_L, N_R and phase ϕ_L, ϕ_R separated by a tunnelling barrier with width w and height V_0 . (B) Absorption image of our Josephson junction in a 2D Fermi gas. (C,D) Time evolution of the phase difference $\Delta\phi$ (C) and relative particle number difference $\Delta N/N$ (D) between the left and right side of the box after imprinting a relative phase difference of $\phi_0 \approx \pi/4$. The red lines are the result of a damped sinusoidal fit.

⁵² This corresponds to an interaction strength of $\ln(k_F a_{2D}) = -2.4$

⁵³ Remarkably, achieving this low damping requires a temperature of $T/T_F \lesssim 0.03$ (Fig. 8.2), which is far below the predicted critical temperature $T_c/T_F \approx 0.1$ for 2D superfluidity at this interaction strength [62, 63].

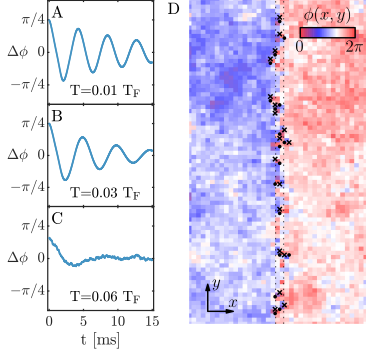


Figure 8.2: Simulated temperature dependence of Josephson oscillations. (A-C) Time evolution of the simulated $\Delta\phi$ for $V_0/\mu \approx 1.0$ and a phase imprint of $\pi/4$ at three different temperatures. (D) Simulated phase evolution of one sample of the ensemble, 3.9 ms after a phase imprint of $\pi/4$, for $n = 2.25 \mu\text{m}^{-2}$ and $T/T_F \approx 0.03$. The barrier height is $V_0/\mu \approx 2$ and its width of $0.85 \mu\text{m}$ is denoted by the two vertical dotted lines. The dots and the crosses represent vortices and antivortices, respectively. The box dimensions are $20 \times 40 \mu\text{m}^2$.

tem. Introducing a barrier with height V_0 adds a nonlinear inductance L_J to the system and reduces the oscillation frequency ω . Due to the nonlinearity of the current phase relation, this L_J depends on the phase difference $\phi(t)$ across the junction, but for small phase excitations there is a linear regime where $L_J(\phi(t))$ can be approximated by a time-independent Josephson inductance $L_{J,0}$ and the oscillation frequency is given by $\omega = 1/\sqrt{(L_B + L_{J,0})C}$.

To confirm that our physical system is described by this model, we prepare a gas of deeply bound dimers, perform measurements of the oscillation frequency in the linear regime as a function of the barrier height for different system sizes (Figs. 8.3A and B), and extract the Josephson inductance $L_{J,0}$ (Fig. 8.3C). Since our system has a uniform density, the bulk inductance is given by the simple expression $L_B = 8m l_\perp / \pi^2 n l_\parallel$, where n is the density per spin state, m is the mass of a ${}^6\text{Li}$ atom, and l_\perp (l_\parallel) is the diameter of the box perpendicular (parallel) to the barrier. Consequently, the Josephson inductance $L_{J,0}(\omega) = L_B(\omega_s^2/\omega^2 - 1)$ can be extracted from the frequency difference between the Josephson oscillations and the sound mode. While the oscillation frequency is strongly dependent on the size of the box due to the change in the bulk inductance L_B and the capacitance C , the measured Josephson inductance $L_{J,0}$ should depend only on the coupling between the two reservoirs. As can be seen from Fig. 8.3C, all measurements of $L_{J,0}$ versus barrier height collapse onto a single curve regardless of the system size, which confirms that our Josephson junction can be described by an LC circuit model. For the barrier heights used in our experiments we also find very good agreement with a full numerical simulation of our system (s. section 8.3).

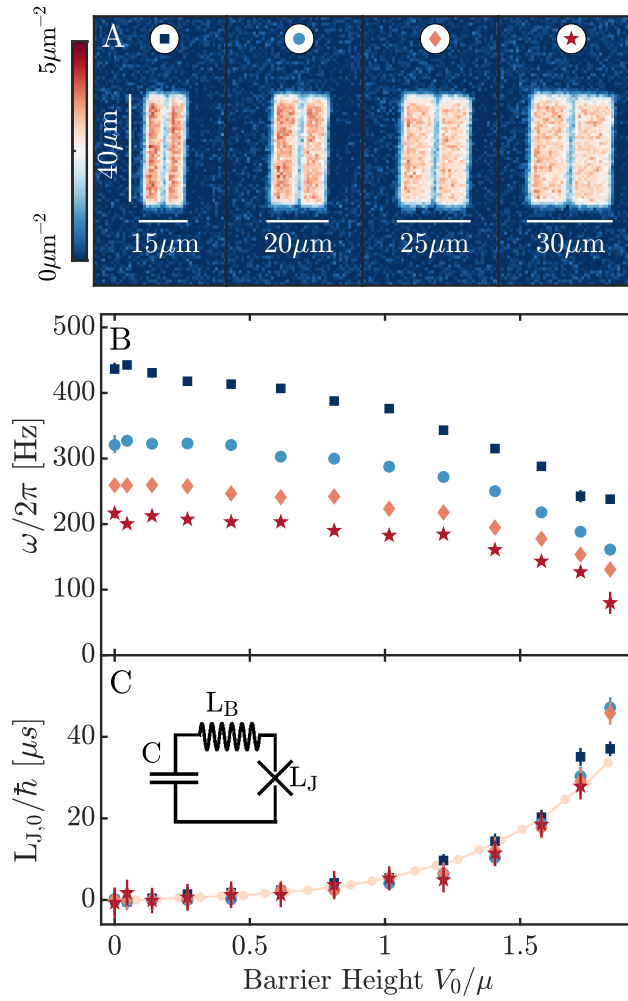


Figure 8.3: **Extracting the Josephson inductance.** (A) Absorption images of cold atom Josephson junctions. The width of the barrier is held fixed at a waist of $w = 0.81(6)\mu\text{m}$, while the size l_\perp of the system is increased. (B) Oscillation frequency as a function of barrier height V_0 for different system sizes, where the error bars denote the 1σ fit error. The inductance L_B and capacitance C of the bulk system are proportional to the length l_\perp of the box and therefore the oscillation frequency decreases with increasing system size for $V_0 = 0$. For nonzero values of V_0 , the barrier adds a nonlinear Josephson inductance L_J to the system and the oscillation frequency decreases as a function of barrier height. (C) Josephson inductance $L_{J,0}(V_0)$ extracted from the frequency measurements using an LC circuit model. The Josephson inductances for all system sizes collapse onto a single curve, which shows that the inductance of the junction depends only on the height of the barrier and validates our LC circuit model. We obtain the calibration of the barrier height V_0 by matching the data to a full numerical simulation (dotted line) explained in section 8.3. The data is obtained by averaging 20 (A) and 7 (B, C) individual measurements.

8.1 Experimental methods

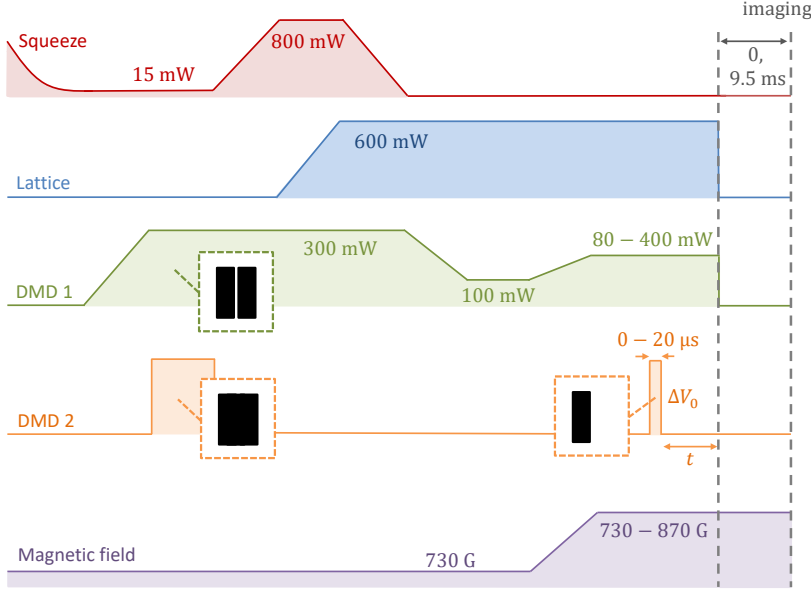


Figure 8.4: **Overview of the experimental cycle to create Josephson junctions in a 2D Fermi gas.** We use DMD1 illuminated with 532 nm light to project a repulsive box potential with a narrow potential barrier (green dashed box) onto our gas after evaporation in the squeeze. Additionally, we use DMD2 illuminated with 532 nm light to project a repulsive box potential without the barrier (left orange dashed box) to push away residual atoms still trapped outside the box. To bring our system into the 2D regime, we increase the squeeze power to compress the gas and transfer it into a single layer of a repulsive optical lattice. Since the compressing is expected to heat the gas, we reduce the power of light which illuminates DMD1 to reduce the height of the box potential and evaporatively cool our system. Next, we tune the magnetic field to a value between 730 G and 870 G while adjusting the DMD1 power to keep the height of the tunnelling barrier relative to the chemical potential V_0/μ constant. To initialise Josephson oscillations, we change the pattern displayed on DMD2 to a step potential (right orange dashed box) and briefly illuminate the DMD for a time between 0 and 20 μ s to imprint an initial relative phase ϕ_0 between 0 and 0.7π . Finally, we let the gas evolve for a varying time t between 0 and 15 ms and image the gas in-situ to extract the particle number $N_L(t)$, $N_R(t)$ in each reservoir or after a time of flight of 9.5 ms to extract the phase difference $\phi(t)$ between the two reservoirs.

In the following section, I provide a more detailed description of our experimental methods to create a Josephson junction, control the phase difference and determine the temperature of our gas. An overview of our experimental sequence to create a Josephson junction is shown in Fig. 8.4.

8.1.1 Creation of a homogeneous 2D Fermi gas

We start our preparation of a Josephson junction by preparing a homogeneous 2D Fermi gas following the scheme described in [96]. We start by evaporatively cooling a spin mixture of ${}^6\text{Li}$ atoms in the $|F = 1/2, m_F = 1/2\rangle$ and $|F = 1/2, m_F = -1/2\rangle$ hyperfine states in a highly elliptical opti-

cal dipole trap at a magnetic field close to the 832 G Feshbach resonance of ${}^6\text{Li}$. We then ramp to a magnetic field of 730 G and project our box potential onto the atoms using a digital micromirror device (DMD⁵⁴) illuminated with blue-detuned ($\lambda = 532$ nm) light, which we refer to as DMD 1. Additionally, we briefly ramp up a second DMD (DMD 2), also illuminated with 532 nm light, that covers a larger area to push away residual atoms still trapped outside of the box. Finally, we load the atoms into a single node of an optical standing wave potential with a lattice spacing of approximately $3\ \mu\text{m}$ and a trap frequency of $\omega_z = 2\pi \cdot 8.8(2)$ kHz and thereby bring the atoms into the 2D-regime. For all measurements, the chemical potential is well below the trap frequency ($\mu < 0.7\ \hbar\omega_z$) and we can therefore parametrise the interaction strength by an effective 2D scattering length $a_{2D} = l_z \sqrt{\pi/0.905} \exp(-\sqrt{\pi/2} \cdot l_z/a_{3D})$ [83], where $l_z = \sqrt{\hbar/m\omega_z}$ is the harmonic oscillator length and a_{3D} is the 3D scattering length.

8.1.2 Creation of a Josephson junction

We create a Josephson junction by using a narrow repulsive potential barrier with a $1/e^2$ waist of $w = (0.81 \pm 0.06)\ \mu\text{m}$ to split the system into two homogeneous 2D pair condensates connected by a weak link (Fig. 8.3 A, B). To create the box potential and the tunnelling barrier, we image DMD 1 directly onto the atoms using a high resolution microscope. The DMD has a pixel size of $7.56\ \mu\text{m}$ and is demagnified by a factor of 75 by the imaging system, so that each DMD pixel has a width of $0.1\ \mu\text{m}$ in the image plane, which is much smaller than the resolution of the imaging system. For narrow barriers with a width $W \lesssim 10$ pixel, we can therefore adjust the height of the barrier by changing the width of the barrier on the DMD image. We characterise the tunnelling barrier by using a second high resolution microscope to image the intensity distribution in the plane of the atoms (Fig. 8.5) for all barrier widths W used in our experiments. From these images, we obtain a calibration of the relative change of the barrier height as a function of W as well as a determination of the barrier width w , which is independent of W for $W \leq 11$ pixel (deviation $< 10\%$).

8.1.3 Phase control and calibration

We imprint an initial relative phase ϕ_0 between the two sides of the junction by briefly illuminating one half of the system for a variable time t between 0 and $20\ \mu\text{s}$ with a spatially homogeneous optical potential ΔV_0 which is created by imaging DMD2 onto the atom plane. The time t is much shorter than the Fermi time \hbar/E_F , which ensures an almost pure phase excitation of $\phi_0 = \Delta V_0 t/\hbar$. To calibrate the imprinted phase ϕ_0 we perform matter wave imaging [96, 197] and observe the relative phase difference between the reservoirs in the displacement of the pair condensation peak. We calibrate this procedure by measuring the periodic displacement of the momentum peak as a

⁵⁴ Texas Instruments DLP6500FYE

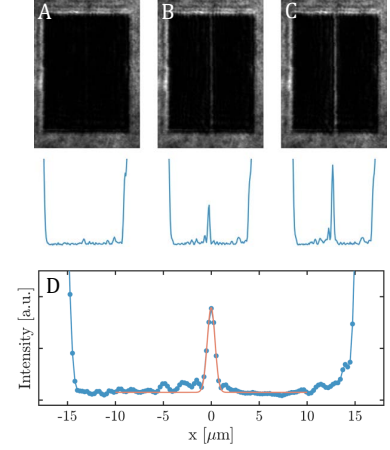
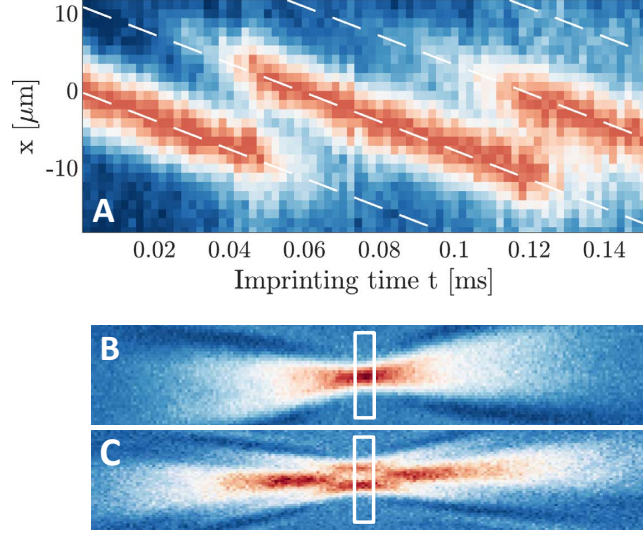


Figure 8.5: Calibration of the barrier. (A-C) Images of optical potentials used to create Josephson junctions and corresponding intensity slices (blue lines) for a box size of $30\ \mu\text{m} \times 40\ \mu\text{m}$ and varying barrier height controlled by the barrier width of 0 pixel (A), 4 pixels (B), and 8 pixels (C) displayed on DMD 1. The projected barriers are broadened by the finite resolution of the imaging system used to project the image onto the atoms. (D) From a Gaussian fit (red line) to the linesum of barrier image (B), we determine a $1/e^2$ waist of $w = 0.81(6)\ \mu\text{m}$.

Figure 8.6: Calibration of phase imprinting. (A) We vary the time t for which the imprinting potential is switched on and measure the shift in the position of the central momentum peak (white dashed line). From its periodic displacement, we obtain the height of the optical potential $\Delta V_0 = h \cdot 16.0(5)$ kHz. Each column represents a horizontal line sum through the in-focus part (white rectangular boxes in (B) and (C)) of the imaged momentum distribution obtained via matter wave focusing. The data shown is obtained by averaging over 38 realisations. (B,C) Exemplary imaged momentum distributions are shown for imprinted phases of (B) $\phi_0 = 0$ for $t = 0$ ms and (C) $\phi_0 \approx \pi$ for $t \approx 50$ ms which both feature a central part which is in focus and, horizontally separated, the imaging broadened part of the cloud which is out of focus.



⁵⁵ We define ΔV_0 as the potential experienced by a pair of atoms, which has two times the polarisability and therefore experiences twice the optical dipole potential as a single atom.

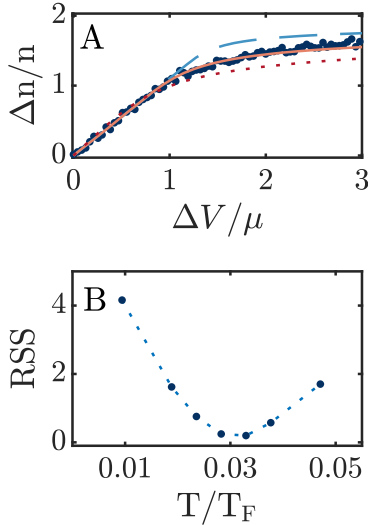


Figure 8.7: Equation of state. (A) Density difference Δn (dark blue dots) created by a potential step ΔV , compared to numerical simulations performed at $T/T_F = 0.019$ (dashed blue line), $T/T_F = 0.033$ (solid red line) and $T/T_F = 0.047$ (dotted dark red line). (B) Residual sum of squares between the numerical simulations performed at different temperatures and the measured EOS. The dashed blue line is a guide to the eye. The best agreement between our measured equation of state and the simulation is achieved at a temperature of $T/T_F = 0.03$.

function of the time for which the imprinting potential is switched on. From the measurement shown in Fig. 8.6, we obtain $\Delta V_0 = h \cdot 16.0(5)$ kHz for the potential height⁵⁵ and a displacement $\Delta x = 5.5(3)\mu\text{m}/\pi$.

8.1.4 Thermometry

We note that performing thermometry of our homogeneous Fermi gas is challenging, since, in contrast to harmonic traps, there is no low density region where the gas is thermal. This makes it very difficult to observe and fit the thermal fraction of the cloud.

We obtain an estimate of the temperature of the system by performing a time of flight measurement after DMD 1 has been ramped on and the atoms have been loaded into the lattice, but without pushing away the low density wing of atoms outside the box with DMD 2. This measurement yields a temperature of $T/T_F \approx 0.03$, where $T_F = E_F/k_B$ is the Fermi temperature of a system with Fermi energy $E_F = \hbar^2 k_F^2 / 2m = \hbar^2 4\pi n / 2m$ using the density n inside the box potential. However, it is *a priori* unclear whether the atoms inside and outside the box potential are fully thermalised, so a better method to perform thermometry is to measure the density equation of state $\mu(n, T)$ of a molecular condensate and compare it to a full numerical simulation (s. Fig. 8.7). To measure the equation of state $\mu(n, T)$ we apply the potential step used for the phase imprinting and measure the density difference Δn between the two sides for varying potential depths ΔV .

To determine the temperature of our system we compare the measured $\Delta n(\Delta V)$ of the bosonic system with interaction strength $\ln(k_F a_{2D}) = -2.9$ with simulated curves for different temperatures obtained using the c-field method described in section 8.3. The discrepancy between the measurement and the numerical simulations is minimised for a temperature of $T \approx 0.03 T_F$ (Fig. 8.7) which agrees well with the time of flight measurement described above.

8.2 Understanding the Josephson dynamics in an LC circuit model

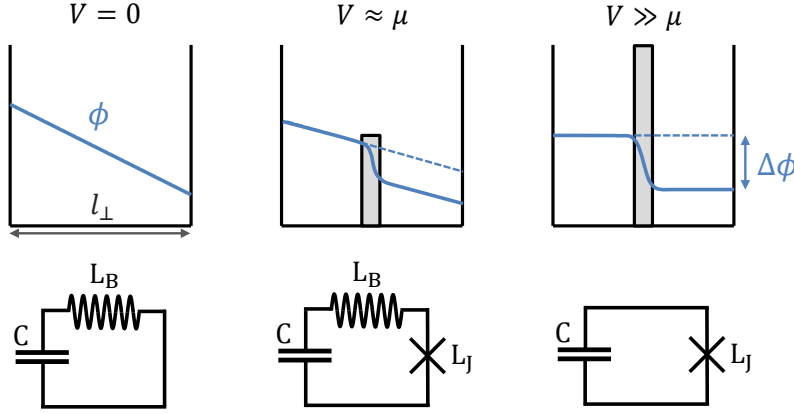


Figure 8.8: Illustrating the different regimes of Josephson dynamics: Without a barrier ($V = 0$) the dynamics are described by a sound wave propagating with the speed of sound v_s between the boundaries of the box with size l_\perp which gives rise to large phase gradients. For very large barrier heights ($V \gg \mu$), the dynamics of the system are dominated by the current $I = I_c \sin(\phi)$ through the barrier and can be understood in a simple two mode model as two weakly linked states with a spatially constant phase in each reservoir. In the intermediate regime, where $V \approx \mu$, the dynamics of the system are both influenced by the barrier and the bulk superfluids which we can understand as a LC circuit in which a nonlinear Josephson inductance $L_J = \hbar/(I_c \cos(\phi))$ is connected in series to a linear bulk inductance L_B and a capacitance C .

The dynamics of our Josephson junction are determined by the bulk dynamics of the two superfluid reservoirs and the tunnelling dynamics in the vicinity of the barrier. These dynamics cannot be captured in the simple two-mode picture introduced in section 7.3.1, because for the barrier depths $V \gtrsim \mu$ and system sizes l_\perp used in our experiments, the spatial form of the wave functions is expected to vary in time, since phase gradients that develop during oscillations do not have sufficient time to fully equilibrate over the reservoirs.

Therefore, to describe the dynamics of our junction we introduce an LC circuit model commonly used to describe superconducting Josephson junctions [192, 195, 196], which isolates the Josephson dynamics in the direct vicinity of the barrier from the superfluid reservoirs.

In our LC circuit model, we describe our junction as a nonlinear Josephson inductance L_J which is connected in series to a linear bulk inductance L_B and a capacitance C (Fig. 8.3F), where the bulk inductance L_B characterises the inertia of the gas and the capacitance C its compressibility. In this circuit, the current $I = \frac{1}{2} \frac{d(\Delta N)}{dt}$ is the instantaneous particle current across the junction determined by the change in the particle number imbalance $\Delta N = N_L - N_R$. The voltage over the capacitor is given by $U_C = \Delta N/2C$, where $\Delta N/2$ corresponds to the charge of the capacitor. The voltage across the junction $U_J = L_J \frac{dI}{dt}$ is related to the phase difference ϕ via the Josephson-Anderson relation $U_J = \hbar \frac{d\phi}{dt}$ and hence the junction has an inductance of $L_J(\phi) = \hbar / \frac{dI(\phi)}{d\phi}$ as derived in extra 7.4. According to Kirchhoff's law, the voltages across the capacitor, the bulk inductance and the junction add to zero and therefore the LC circuit is described by the differential equation

$$\frac{\Delta N}{C} + (L_B + L_J(\phi)) \frac{\partial^2(\Delta N)}{\partial t^2} = 0. \quad (8.1)$$

For small phase excitations, $L_J(\phi)$ can be approximated by a constant, phase independent inductance $L_{J,0}$ and Eq. 8.1 yields harmonic oscillations with frequency $\omega = \frac{1}{\sqrt{(L_B + L_{J,0})C}}$. For a vanishing barrier,

the oscillations correspond to a phononic excitation propagating between the boundaries of the box at the speed of sound v_s across the length l_\perp of the system. In the circuit model, this corresponds to $L_J = 0$ and the frequency is given by $\omega_s = \frac{1}{\sqrt{L_B C}} = 2\pi \frac{v_s}{2l_\perp}$. Hence, we can calculate $L_{J,0}$ from the ratio of the oscillation frequencies

$$L_{J,0} = L_B \left(\frac{\omega_s^2}{\omega^2} - 1 \right). \quad (8.2)$$

For our homogeneous box system, the speed of sound $v_s = \sqrt{\frac{n}{m} \frac{\partial \mu}{\partial n}}$ and the capacitance $C = \frac{1}{2} \frac{\partial N}{\partial \mu_B} = \frac{1}{4} \frac{\partial N}{\partial \mu} = \frac{1}{8} l_\perp l_\parallel \frac{\partial n}{\partial \mu}$ are related to each other by the compressibility $\kappa = \frac{\partial \mu}{\partial n}$, where $\mu_B = 2\mu$ is the chemical potential of a gas of bosonic dimers. Therefore, we can simply calculate the bulk inductance $L_B = 1/\omega_s^2 C = 8m l_\perp / \pi^2 n l_\parallel$ and thereby obtain the Josephson inductance $L_{J,0}$ without using the equation of state $\mu(n)$, where n is the density per spin state, m is the mass of a ${}^6\text{Li}$ atom, and l_\perp (l_\parallel) is the diameter of the box perpendicular (parallel) to the barrier.

8.3 Comparison with numerical simulations

The following section describes numerical simulations of our Josephson junction which were developed by Vijay Singh and Ludwig Mathey and are described in more detail in [198].

The dynamics of a 2D bosonic Josephson junction are simulated with the c-field method that was used in Ref. [199]. Our homogeneous 2D system is described by the Hamiltonian

$$\hat{H}_0 = \int d\mathbf{r} \left[\frac{\hbar^2}{2M} \nabla \hat{\psi}^\dagger(\mathbf{r}) \cdot \nabla \hat{\psi}(\mathbf{r}) + \frac{g}{2} \hat{\psi}^\dagger(\mathbf{r}) \hat{\psi}^\dagger(\mathbf{r}) \hat{\psi}(\mathbf{r}) \hat{\psi}(\mathbf{r}) \right], \quad (8.3)$$

where $\hat{\psi}$ and $\hat{\psi}^\dagger$ are the bosonic annihilation and creation operators, respectively. The interaction g is given by $g = \tilde{g} \hbar^2 / M$, where \tilde{g} is the dimensionless interaction and M the mass of a ${}^6\text{Li}_2$ molecule. Here, \tilde{g} is determined by $\tilde{g} = \tilde{g}_0 / (1 - \frac{\tilde{g}_0}{2\pi} \ln(2.09 k_F \ell_d))$, with $\tilde{g}_0 = \sqrt{8\pi} a_s / \ell_d$ [80], where a_s is the molecular s-wave scattering length, $\ell_d = \sqrt{\hbar / (M \omega_z)}$ is the harmonic oscillator length in the transverse direction, and k_F is the Fermi wave vector. Analogous to the experiments, 2D clouds of ${}^6\text{Li}_2$ molecules confined in a box of dimensions $L_x \times L_y$ are considered. The space is discretised with a lattice of size $N_x \times N_y$ and a discretisation length $l = 0.5 \mu\text{m}$. Within the c-field representation, the operators $\hat{\psi}$ in Eq. 8.3 and the equations of motion are described by complex numbers ψ . The initial states are sampled in a grand canonical ensemble with chemical potential μ and temperature T via a classical Metropolis algorithm. The system parameters, such as the density n , \tilde{g} , and T are chosen in accordance with the experiments. To simulate the Josephson junction, the term $\mathcal{H}_{\text{ex}} = \int d\mathbf{r} V(\mathbf{r}) n(\mathbf{r})$ is added, where $n(\mathbf{r})$ is the density at the location $\mathbf{r} = (x, y)$. The barrier potential $V(\mathbf{r})$ is given by

$$V(\mathbf{r}) = V_0 \exp(-2(x - x_0)^2 / w^2), \quad (8.4)$$

where V_0 is the barrier height and w the width. The potential is centered at the location $x_0 = L_x/2$. Analogous to the experiments, a waist of $w = 0.85 \mu\text{m}$ and a barrier height V_0/μ in the range $0 - 2$ is chosen, where $\mu = gn$. This splits the system in x -direction into two equal 2D clouds, which we refer to as the left and right reservoir. Subsequently, a fixed value of the phase is imprinted on one of the reservoirs, which creates a phase difference $\Delta\phi = \phi_L - \phi_R$, where ϕ_L (ϕ_R) is the mean value of the phase of the left (right) reservoir. The sudden imprint of phase results in oscillations of $\Delta\phi$ and the density imbalance $\Delta N = N_L - N_R$, where N_L (N_R) is the number of molecules in the left (right) reservoir. We analyse the time evolution of ΔN and $\Delta\phi$ for system parameters close to the ones used in the experiments. Fig. 8.2 A-C shows simulations of $\Delta\phi(t)$ at three different temperatures of $T/T_F \approx 0.01, 0.03$, and 0.06 for $n = 2.25 \mu\text{m}^{-2}$, $\tilde{g} = 1.8$ and a system size of $L_x \times L_y = 20 \times 40 \mu\text{m}^2$. The damping of the oscillations increases with temperature. To quantify this observation, we fit $\Delta\phi(t)$ with a damped sine function $f(t) = A_0 e^{-\Gamma t} \sin(\omega t + \theta)$, where A_0 is the amplitude, ω is the oscillation frequency, Γ is the damping, and θ is the phase shift. The determined ratio of Γ/ω is $0.05, 0.09$, and 0.45 for $T/T_F \approx 0.01, 0.03$, and 0.06 , respectively. As the experimentally observed damping is on the order of $\Gamma/\omega \approx 0.07$, this suggests an experimental temperature on the order of $T/T_F \lesssim 0.03$, which is consistent with the results from measurements of the momentum distribution and the equation of state shown in Fig. 8.7. To obtain a calibration of the experimental barrier height, the system is simulated for a wide range of barrier heights V_0 and the simulated and extracted Josephson inductances are matched by fitting the calibration factor between the width W of the barrier on the DMD and the simulated barrier height V_0 .

To understand the mechanism for the thermal damping of the oscillations, we examine the phase evolution of a single sample of our ensemble. Figure S 8.2D shows the phase $\phi(x, y)$ at a point in time which is 3.9 ms after a phase imprint of $\pi/4$ for the same n , \tilde{g} and box size as above, and $T/T_F \approx 0.03$. At this time the system exhibits distinct values of the mean phase for the left and right reservoir and a strong phase gradient across the barrier. As expected for a 2D system, the phase is weakly fluctuating within the reservoirs due to thermal phonons. In addition to the phonons, we identify the nucleation of vortex-antivortex pairs as an additional mechanism of dissipation. The phase winding around a lattice plaquette of size $l \times l$ is calculated using $\sum_{\square} \delta\phi(x, y) = \delta_x\phi(x, y) + \delta_y\phi(x + l, y) + \delta_x\phi(x + l, y + l) + \delta_y\phi(x, y + l)$, where the phase differences between sites is taken to be $\delta_{x/y}\phi(x, y) \in (-\pi, \pi]$. The calculated phase winding is shown in Fig. 8.2D. A vortex and an antivortex are identified by a phase winding of 2π and -2π , respectively. The vortex pairs are nucleated mainly inside the barrier in the regions of low densities. Both the phonons and vortices lead to the damping of oscillations shown in Fig. 8.2 A-C.

The fundamental property of Josephson junctions is a nonlinear current-phase relation $I(\phi)$, which arises when two phase coherent quantum states are weakly linked. While in principle the explicit form of $I(\phi)$ depends on the microscopic details of the link and the coupled quantum states[30], for an ideal Josephson junction the current-phase relation takes a simple sinusoidal form $I(\phi) = I_C \sin(\phi)$, where the critical current I_C is a direct measure for the wave function overlap.

For superfluid helium, such ideal Josephson junctions could be realized with nano-aperture arrays which enabled a striking demonstration of the transition from a linear to a sinusoidal current-phase relation in the crossover from a strong to a weak link (s. Fig. 7.10). While more recently superfluid Josephson junctions were also extensively studied with ultracold quantum gases, the characteristic nonlinear current-phase relation could not be observed. So far, the only available measurement of the current-phase relation in a cold atom Josephson junction is consistent with the linear form $I(\phi) \propto \phi$ expected in the strong coupling limit (s. Fig. 9.2) [200].

In this chapter, we report on the observation of a sinusoidal current-phase relation in a cold atom Josephson junction. To probe the current-phase relation of our junction we measure the frequency of Josephson oscillations as a function of the phase difference across the junction. Our result shows that the critical current of our junction is determined by the wave function overlap and can therefore be used as a probe for the order parameter in our 2D fermionic superfluid as presented in chapter 10.

9.1 Probing the current-phase relation of an ideal Josephson junction

To probe the current-phase relation of our Josephson junction we excite Josephson oscillations with large phase amplitudes ϕ_0 (s. Fig. 9.3). In this regime, the nonlinear current-phase relation leads to anharmonic oscillations with an increased oscillation period $T(\phi_0)$. One possibility to extract the current-phase relation from such anharmonic oscillations would be to obtain the instantaneous current $I(\phi(t))$ and relating it to the corresponding phase difference $\phi(t)$ (s. Fig. 9.1). However, this approach has the significant drawback that obtaining $I(\phi(t))$ requires numerical differentiation of $\Delta N(t)$, which is extremely sensitive to noise.

Hence, we use the information contained in the shift of the fundamental frequency $\omega(\phi_0) = 2\pi/T(\phi_0)$ to probe the current-phase relation. We achieve this by imprinting a variable initial phase difference

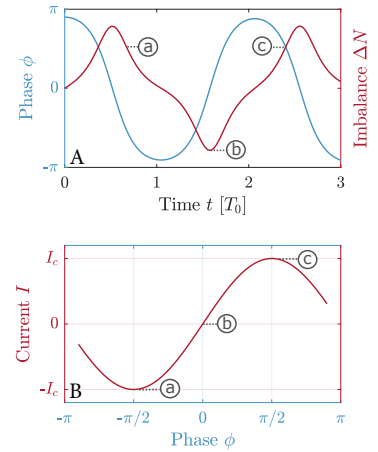


Figure 9.1: (A) Simulated Josephson oscillations in imbalance ΔN (red) and phase difference ϕ (blue) for a large phase amplitude of $\phi_0 = 0.9\pi$, where we assumed an ideal current-phase relation $I(\phi) = I_C \sin(\phi)$ and the limit of a deep barrier $L_J \gg L_B$. The oscillations are anharmonic with an increased oscillation period $T \approx 2T_0$ compared to its small amplitude value T_0 . (B) The current-phase relation determines the instantaneous current $I(\phi(t)) = \frac{1}{2} \frac{d}{dt} \Delta N(t)$ as illustrated in (A) and (B) for $\phi = -\pi/2$ (a), $\phi = 0$ (b), and $\phi = \pi/2$ (c).

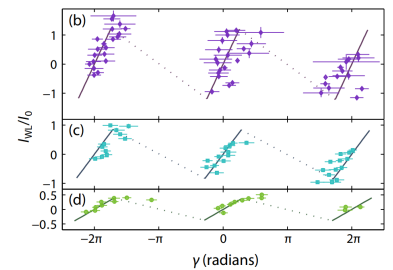


Figure 9.2: Measurement of the current-phase relation in a 3D Bose gas. A weak link was rotated through a ring-shaped BEC and the corresponding current I_{WL} and phase drop γ over the link were extracted from interference measurements. Since the size of the weak link ($\sim 6 \mu\text{m}$) is large compared to the healing length of the gas ($\xi \sim 0.3 \mu\text{m}$), a linear form of $I_{WL}(\gamma)$ was observed for potential heights of the weak link of $V_0 = 0.45\mu$ (b), $V_0 = 0.6\mu$ (c), and $V_0 = 0.7\mu$ (d). Adapted from [200].

$\phi_0 = 0 - 0.7\pi$ across the barrier and measuring the reduction of the fundamental frequency $\omega(\phi_0)$ as a function of ϕ_0 (s. Fig 9.3D). To extract the nonlinear response of the current from our measurements of $\omega(\phi_0)$, we first use eq. 8.2 to calculate the corresponding Josephson inductance⁵⁶

$$L_{J,0}(\phi_0) = L_B \left(\frac{\omega_s^2}{\omega^2(\phi_0)} - 1 \right). \quad (9.1)$$

We then apply the relation $\partial I / \partial \phi = \hbar / L_J$ to $L_{J,0}(\phi_0)$ to obtain an effective current

$$I_0(\phi_0) = \int_0^{\phi_0} \frac{\hbar}{L_{J,0}(\phi'_0)} d\phi'_0 \quad (9.2)$$

by integrating⁵⁷ over the values of the imprinted phase ϕ_0 .

While this effective current is different from the instantaneous current, we can directly relate the effective current-phase relation $I_0(\phi_0)$ and the instantaneous current-phase relation $I(\phi)$. In particular, we show that for an ideal Josephson junction I_0 follows a rescaled current-phase relation⁵⁸

$$I_0(\phi_0) \approx 2I_C \sin(\phi_0/2). \quad (9.3)$$

We find that our measurement is in excellent agreement with this sinusoidal current-phase relation, indicating that our junction is an ideal Josephson junction [30, 200]. This implies that the current across the junction is indeed a supercurrent, driven by the phase difference between two superfluids.

⁵⁶ It is important to note that this inductance $L_{J,0}(\phi_0)$ only depends on the phase amplitude ϕ_0 and is therefore different from the instantaneous inductance $L_J(\phi(t))$ which changes during anharmonic oscillations. Instead, $L_{J,0}(\phi_0)$ can be understood as a time averaged quantity which can be obtained by averaging $L_J(\phi(t))$ over an oscillation period T .

⁵⁷ The integral expression 9.2 for $I_0(\phi_0)$ is evaluated by performing a Riemann sum over all experimentally determined values of $\frac{\hbar}{L_{J,0}(\phi'_0)}$ for which $\phi'_0 \leq \phi_0$

⁵⁸ Eq. 9.3 is derived for $L_J \gg L_B$ in extra 9.1 and numerically validated in the experimentally relevant regime of $L_J \gtrsim L_B$ in section 9.3.1.

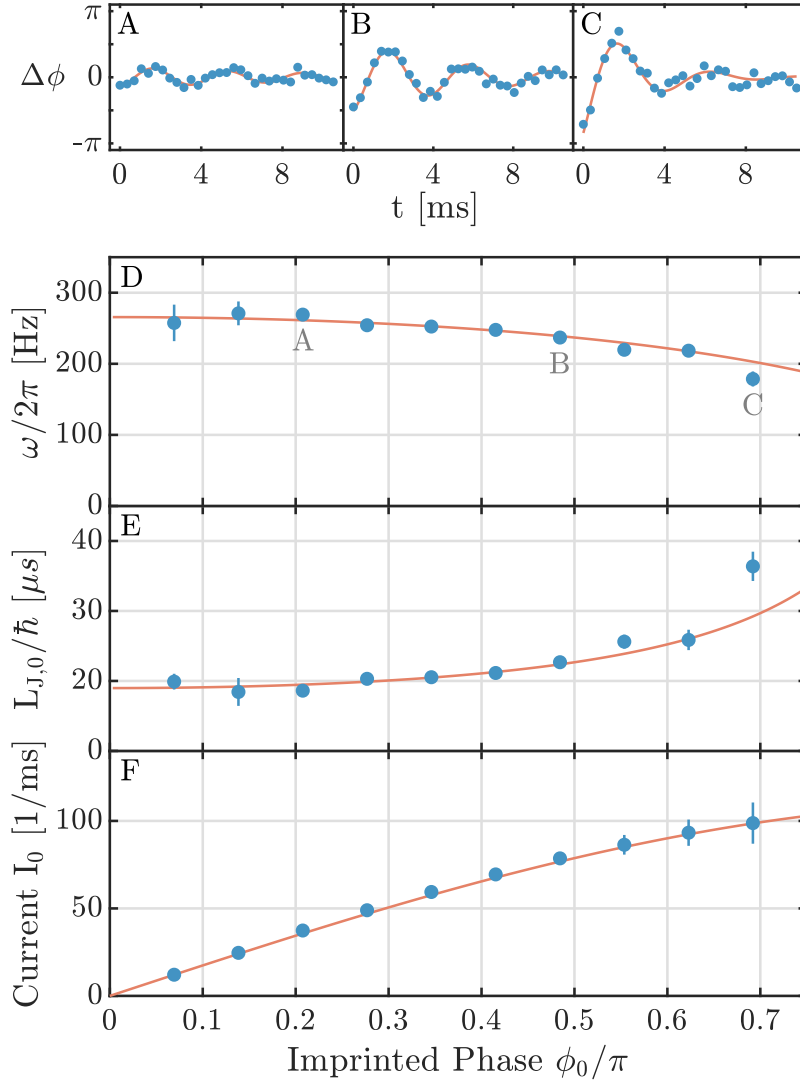


Figure 9.3: **Current-phase relation.** Josephson oscillations through a tunnelling barrier with height $V_0/\mu = 1.51(8)$ at initial phase imprints of $\phi_0 = 0.14\pi$ (A), 0.42π (B) and 0.62π (C). The amplitude of the oscillations increases for stronger phase imprints, while the frequency is reduced. (D) Oscillation frequency as a function of imprinted phase, where the error bars denote the 1σ fit error. (E) Inductance of the junction calculated from the measured oscillation frequencies. (F) Effective current I_0 through the junction obtained by performing a Riemann sum over the measured values of $L_{J,0}$ shown in (E) according to $\partial I/\partial\phi = \hbar/L_J$. Our data is in excellent agreement with the rescaled current-phase relation $I_0 = 2I_C \sin(\phi_0/2)$ expected for an ideal Josephson junction (red solid lines), where the initial slope I_C is determined from the first three data points. Each data point in (A, B, C) is obtained by averaging 20 individual measurements.

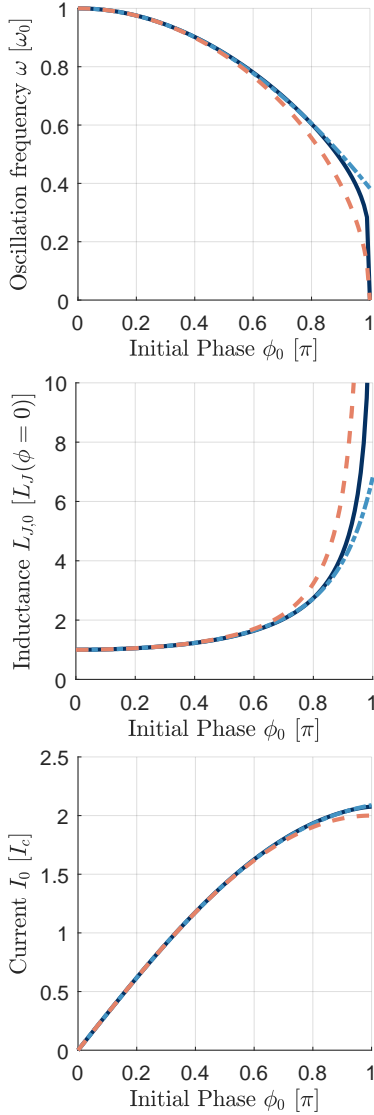


Figure 9.4: Illustration of our method to probe the current-phase relation for an ideal Josephson junction. Equivalent to a mathematical pendulum, the oscillation period increases as $T(\phi_0) = T_0 \frac{2}{\pi} K(\sin(\phi_0))$, where $K(k) = \int_0^{\pi/2} \frac{du}{\sqrt{1-k^2 \sin^2 u}}$ is the complete elliptic integral of the first kind. The corresponding shift in the fundamental frequency $\omega(\phi_0) = 2\pi/T(\phi_0)$ (black solid line) can be well approximated by $\omega = \omega_0(1 - \phi_0^2/16)$ (blue dash-dotted line) and $\omega = \sqrt{\cos(\phi_0/2)}$ (orange dashed line). We calculate the corresponding Josephson inductance $L_{J,0} = \frac{\hbar}{I_c} (\omega_0/\omega)^2$ and the effective current I_0 according to eq. 9.9. For phase excursions $\phi_0 \leq 0.7\pi$, the effective current is well-approximated by $I_0 = 2I_c \sin(\phi_0/2)$.

Extra 9.1: Derivation of the effective current-phase relation $I_0(\phi_0)$

To understand how a measurement of the Josephson oscillation frequency $\omega(\phi_0)$ as function of the imprinted phase ϕ_0 can be used to probe the current-phase relation $I(\phi)$, it is instructive to consider an ideal Josephson junction in the limit of a dominating barrier (s. Fig. 8.8).

In this limit, the dynamics of the junction are described by the differential equation

$$U_J + U_C = \hbar \dot{\phi} + \frac{\Delta N}{2C} = 0 \quad (9.4)$$

, which after differentiation and using $I(\phi) = \frac{1}{2} \frac{d}{dt} \Delta N$ can be expressed as

$$\hbar \ddot{\phi} + \frac{I(\phi)}{C} = 0. \quad (9.5)$$

Using $I(\phi) = I_c \sin(\phi)$ we can express eq. 9.5 as

$$\ddot{\phi} + \omega_0^2 \sin(\phi) = 0, \quad (9.6)$$

, where $\omega_0 = 1/\sqrt{L_J(0)C}$ and $L_J(0) = \hbar/I_c$. Eq. 9.6 is equivalent to the equation of motion of a mathematical pendulum with linear oscillation frequency ω_0 (s. Fig. 9.5). As shown in Fig. 9.4 the frequency decreases to second order in the phase amplitude ϕ_0 as

$$\omega(\phi_0) \approx \omega_0(1 - \phi_0^2/16) \approx \omega_0 \sqrt{\cos(\phi_0/2)}. \quad (9.7)$$

Since for an ideal Josephson junction $2 \frac{\partial I(\phi/2)}{\partial \phi} \Big|_{\phi_0} = I_c \cos(\phi_0/2)$ we can directly express eq. 9.7 in terms of the derivative $\partial I/\partial \phi$ as

$$\omega^2(\phi_0) \approx \omega_0^2 \frac{1}{I_c} 2 \frac{\partial I(\phi/2)}{\partial \phi} \Big|_{\phi_0}. \quad (9.8)$$

Therefore, the current-phase relation can finally be reconstructed by integrating over the phase ϕ_0 ,

$$2I\left(\frac{\phi_0}{2}\right) \approx \int_0^{\phi_0} I_c \frac{\omega^2(\phi'_0)}{\omega_0^2} d\phi'_0 = \int_0^{\phi_0} \frac{\hbar}{L_{J,0}(\phi'_0)} d\phi'_0 \equiv I_0(\phi_0), \quad (9.9)$$

where we expressed the integrand in terms of the Josephson inductance $L_{J,0}(\phi'_0) = \frac{\hbar}{I_c} \left(\frac{\omega_0}{\omega(\phi'_0)}\right)^2$ for a system with vanishing bulk inductance.

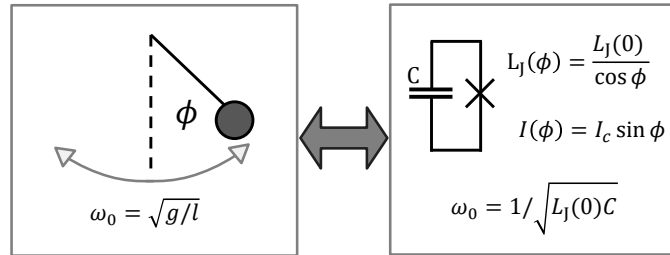


Figure 9.5: Analogy between a nonlinear LC circuit and a mathematical pendulum. Eq. 9.6 describes both the oscillation of the phase difference ϕ of an ideal Josephson junction in series with a capacitance C and a mathematical pendulum with excursion angle ϕ .

9.2 Estimate of higher order contributions

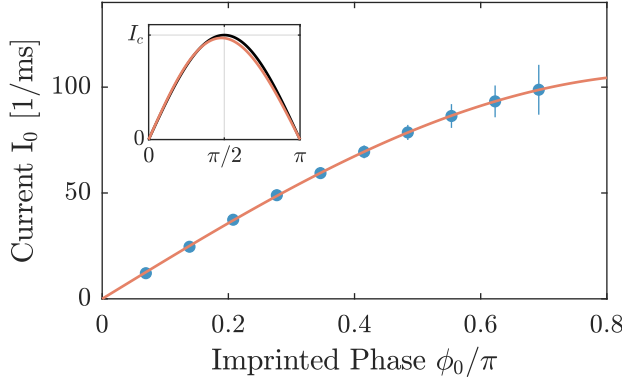


Figure 9.6: Higher order contributions to the current-phase relation. We fit our extracted current I_0 from Fig. 9.3F (blue dots) with eq. 9.11 to account for contributions to the current-phase relation up to second order $I_{2\phi}(\phi) = I_1 \sin(\phi) + I_2 \sin(2\phi)$ and obtain a ratio of the second order current to the first order current of $I_2/I_1 = 0.03$ (red line). The corresponding instantaneous current $I_{2\phi}$ for this value of I_2/I_1 (inset, red line) agrees well the ideal sinusoidal form with $I_2 = 0$ (inset, black line).

To further support our observation of a sinusoidal current-phase relation, we compare our data shown in Fig. 9.3 F with a more general current-phase relation

$$I_{2\phi}(\phi) = I_1 \sin(\phi) + I_2 \sin(2\phi), \quad (9.10)$$

where the current I_1 (I_2) corresponds to the first (second) order contribution to the critical current [30].⁵⁹ In this case, the extracted current I_0 obtained from 9.9 is also expected to follow a simple rescaled form⁶⁰

$$I_0(\phi_0) \propto \sin(A\phi_0/2). \quad (9.11)$$

Here the additional scaling parameter A is given by

$$A^2 = \frac{1 + 8I_2/I_1}{1 + 2I_2/I_1}, \quad (9.12)$$

and interpolates between $A = 1$ for $I_2/I_1 = 0$ and $A = 2$ for $I_2/I_1 \gg 1$.

We fit our data to eq. 9.11 and obtain $A = 1.09(1)$ (s. Fig. 9.6). This corresponds to a contribution of the second harmonic current of $I_2/I_1 = 0.03$, which is well within the uncertainty of our measurement.

Numerical simulation of the current-phase relation

Finally, we note that achieving this sinusoidal current-phase relation requires a barrier deep in the tunnelling regime which is fulfilled for our barrier depth of $V_0/\mu \approx 1.5$. To estimate the effect of a reduced barrier depth on the current-phase relation, the Josephson dynamics of our system are simulated for barrier depths $1.25 \leq V_0/\mu \leq 2.5$ using the numerical method described in chapter 8.3. We find good agreement with a sinusoidal current-phase relation for barrier depths $V_0/\mu \geq 1.75$ which agrees with our experimental value within the systematic errors of our barrier depth calibration. For lower barrier depths, we observe deviations from this ideal Josephson regime as expected from higher contributions to the current-phase relation described by eq. 9.10.

⁵⁹ As described in [30] the current-phase relation can generally be expressed in a Fourier series as $I(\phi) = \sum_{n \geq 1} I_n \sin(n\phi) + J_n \cos(n\phi)$ with n -th order coefficients I_n and J_n . The coefficients J_n vanish if time-reversal is not broken.

⁶⁰ For a derivation of eq. 9.11 see section 9.3.2.

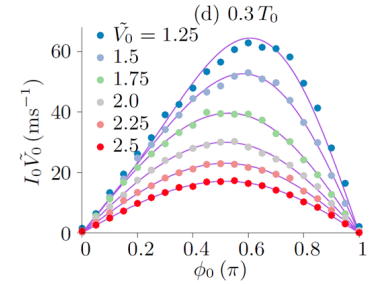
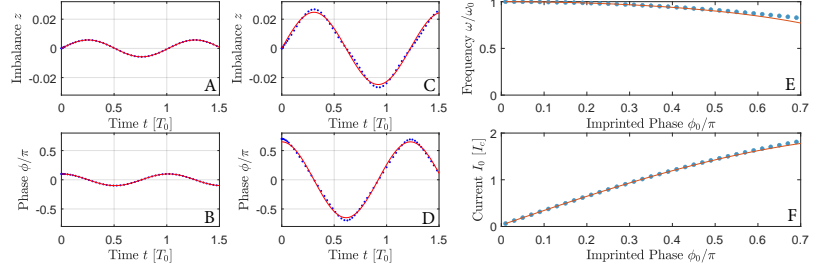


Figure 9.7: The current-phase relation in dependence on the barrier depth. The current-phase relation is extracted from a numerical simulation of a junction with parameters comparable to the ones used in our experiments with a density of $n = 2.25/\mu\text{m}^2$, interaction parameter $\tilde{g} = 1.8$ and temperature $T/T_0 = 0.3$. Here T_0 is the critical temperature corresponding to a critical phase space density of $n\lambda_c^2 = \ln(380/\tilde{g})$ [90]. We observe a transition from the ideal Josephson regime for high barrier depths $\tilde{V}_0 = V_0/\mu \gtrsim 1.75$ to the onset of higher order contributions for barrier depths $\tilde{V}_0 \lesssim 1.5$. Adapted from [198].

9.3 Methods

9.3.1 Numerical validation of our scheme to probe the current-phase relation

Figure 9.8: Numerical validation of our scheme to probe the current-phase relation We numerically solve eq. 9.13 for $L_{J,0}/L_B = 1.3$ for initial phases $0 \lesssim \phi_0 \leq 0.7\pi$. (A,B) For a small initial phase $\phi_0 = 0.1\pi$, we observe harmonic oscillations in imbalance z (A) and phase difference ϕ (B) with oscillation period $T = T_0$. (C,D) For a large initial phase $\phi_0 = 0.7\pi$, the oscillations in imbalance z (C) and phase difference ϕ (D) are anharmonic with an increased oscillation period $T > T_0$. (E) We determine the frequency $\omega = 2\pi/T$ of oscillations for initial phase differences $0 \lesssim \phi_0 \leq 0.7\pi$ using a harmonic fit to the simulated data (red lines in (A-D)). (F) We obtain the effective current $I_0(\phi_0)$ by calculating the inductance $L_{J,0}(\omega)$ for each initial phase ϕ'_0 and evaluating the integral $I_0(\phi_0) = \int_0^{\phi_0} d\phi'_0 \hbar/L_{J,0}(\phi'_0)$ according to eq. 9.2. We find that the extracted current I_0 agrees well with the rescaled current-phase relation $I_0(\phi_0) = 2I_c \sin(\phi_0/2)$ (red lines in (E) and (F)) expected for an ideal Josephson junction, which validates our experimental scheme to probe the current-phase relation for the parameters used in our experiment.



In the previous section we have described our extraction scheme for the current-phase relation $I_0(\phi_0)$ that is based on frequency measurements. It works for an isolated Josephson junction and produces a simple rescaled current-phase relation. Here, I will show that this extraction scheme is also suitable for the case of a Josephson junction in series with a bulk inductance which describes our experiment better. In particular, I will show that for an ideal Josephson junction in series with a linear bulk inductance, we extract the rescaled current-phase relation given by eq. 9.9 up to small corrections on the order of 2%. To do this we rewrite the general differential equation 8.1 for our system as

$$\Delta N + \frac{1}{\omega_s^2} \left(1 + \frac{L_J(\phi)}{L_B} \right) \frac{\partial^2(\Delta N)}{\partial t^2} = 0. \quad (9.13)$$

We numerically simulate the dynamics of Eq. 8.1 for a range of initial phase excursion ϕ_0 with the characteristics of an ideal Josephson junction $L_J = \hbar/(I_c \cos(\phi))$ and $L_{J,0}/L_B = 1.3$ which is the value of $L_{J,0}/L_B$ for the system that was used for the measurements in Fig. 9.3. In analogy to our measurement routine, we fit the resulting anharmonic oscillations for each value of ϕ_0 to extract the fundamental oscillation frequency $\omega(\phi)$ and extract the corresponding current-phase relation $I_0(\phi_0)$ according to eq. 9.2. We find that for initial phase excitations $\phi_0 \lesssim 0.7\pi$, eq. 9.3 and the numerically extracted current-phase relation $I_0(\phi_0)$ agree within 2% (s. Fig. 9.8)⁶¹. Hence, we compare our data shown in Fig. 9.3 to eq. 9.3.

9.3.2 Derivation of the the generalized rescaled current-phase relation to estimate the contribution of higher harmonics

In the previous section we have shown that the experimentally determined determined effective current I_0 for our system with $L_B/L_J = 1.3$ is expected to follow a simple rescaled form $I_0 = 2I_c \sin(\phi_0/2)$ for a sinusoidal current-phase relation $I(\phi) = I_c \sin(\phi)$. Here, we will

⁶¹ We note that for systems with dominant bulk inductance $L_B > L_J$, the deviation between extracted current-phase relation $I_0(\phi_0)$ and the simple rescaled expression 9.2 increases. Hence, our direct probing of the current-phase relation $I(\phi)$ only works in our experimentally accessed regime of $L_J > L_B$.

generalise this result and show that for a more general current-phase relation $I(\phi) = I_1 \sin(\phi) + I_2 \sin(2\phi)$ the extracted current I_0 also follows a simple rescaled form

$$I_0(\phi_0) \propto \sin(A\phi_0/2), \quad (9.14)$$

where the scaling parameter A is determined by the ratio of I_2/I_1 .

To do this, we generalise eq. 9.5 for an arbitrary current-phase relation $I(\phi)$

$$\ddot{\phi} + \frac{1}{\hbar C} I(\phi) = 0. \quad (9.15)$$

To second order, the current-phase relation can be expressed as [30]

$$I(\phi) = I_1 \sin(\phi) + I_2 \sin(2\phi), \quad (9.16)$$

where the current $I_{1/2}$ corresponds to the first/second order contribution to the critical current. Therefore, the differential equation 9.15 reduces to

$$\ddot{\phi} + \omega_1^2 \sin(\phi) + \omega_2^2 \sin(2\phi) = 0, \quad (9.17)$$

where $\omega_{1,2}^2 = I_{1,2}/\hbar C$. We determine the oscillation period T of the anharmonic oscillations described by eq. 9.17 which is of the general form

$$\ddot{\phi} = F(\phi), \quad (9.18)$$

with

$$F(\phi) = -\omega_1^2 \sin(\phi) - \omega_2^2 \sin(2\phi). \quad (9.19)$$

As described in [201] the oscillation period T normalised to 2π to second order in the amplitude ϕ_0 is given by

$$T \approx T_0 + T_2 \phi_0^2, \quad (9.20)$$

where $T_0 = 2\pi$, $T_2 = \frac{\pi}{12} \left(10 \left(\frac{F_2}{F_1} \right)^2 + 9 \frac{F_3}{F_1} \right)$ and $F_1 = -\omega_1^2 - 2\omega_2^2$, $F_2 = 0$, $F_3 = \omega_1^2/6 + 4\omega_2^2/3$ are the Taylor coefficients of

$$F(\phi) = \sum_{j=1}^{\infty} F_j \phi_0^j. \quad (9.21)$$

Inserting the value for T_2 , we obtain

$$T \approx 2\pi + \frac{\frac{1}{6}\omega_1^2 + \frac{4}{3}\omega_2^2}{\omega_1^2 + 2\omega_2^2} \phi_0^2. \quad (9.22)$$

Using $(\omega_2/\omega_1)^2 = I_2/I_1$, we get the following expression for the oscillation period

$$T/T_0 \approx 1 + \frac{1}{16} A^2 \phi_0^2 \quad (9.23)$$

and for the fundamental oscillation frequency

$$\omega(\phi)/\omega_0 \approx 1 - \frac{1}{16} A^2 \phi_0^2, \quad (9.24)$$

where

$$A^2 = \frac{1 + 8\frac{I_2}{I_1}}{1 + 2\frac{I_2}{I_1}}. \quad (9.25)$$

Therefore, we finally get

$$(\omega(\phi)/\omega_0)^2 \approx 1 - \frac{1}{8}A^2\phi_0^2 \approx \cos(A\phi_0/2) \quad (9.26)$$

and obtain

$$I_0(\phi_0) \propto \sin(A\phi_0/2), \quad (9.27)$$

which generalises eq. 9.9 to account for second order contributions to the current-phase relation.

The superfluid and coherence properties of a quantum system depend dramatically on its dimensionality. While 3D superfluids display long-range coherence where the phase of the order parameter $\Psi(\mathbf{r})$ remains correlated over the whole system, reducing the dimensionality increases phase fluctuations and thereby prevents such long-range order for any non-zero temperature [11, 12]. While in 1D quantum systems these phase fluctuations dominate for any finite temperature and prevent superfluidity altogether, in 2D systems BKT theory predicts that for sufficiently low temperatures the formation of vortex antivortex pairs can significantly suppress long-range phase fluctuations and thereby enable superfluidity [13, 14].⁶²

One of the most striking experimental demonstrations of the BKT transition was provided by Bishop and Reppy [202] in a thin superfluid ^4He film, where the predicted jump of the superfluid density from $n_s = 4/\lambda_{\text{dB}}^2$ to $n_s = 0$ [89] could be observed as the temperature of the system was increased above T_c (s. Fig. 10.1). However, since such superfluid helium films do not enable access to the local phase of the superfluid order parameter, the characteristic change in the decay of g_1 from algebraic to exponential at the phase transition from superfluid to normal could not be observed in these experiments.

Ultracold atoms offer the unique possibility to directly measure correlation functions of the superfluid order parameter to provide insight into the nature of the BKT transition. So far, measurements of phase coherence in 2D quantum gases were based on time of flight measurements. In their pioneering work, Hadzibabic et al. [144] used the interference between 2D Bose gases to gain information about phase coherence in such ultracold 2D superfluids as suggested in [203] (s. Fig. 10.2). In particular, the authors of [144] observed a transition from quasi long-range phase coherence at low temperatures to enhanced phase fluctuations at high temperatures, while the transition was accompanied by the proliferation of free vortices - a striking demonstration of the microscopic origin for the BKT transition. More recently, evidence for the BKT transition could also be obtained in strongly interacting 2D Fermi gases by extracting the first order correlation function $g_1 = \text{FT}(\tilde{n}(\mathbf{k}))$ from the momentum distribution $\tilde{n}(\mathbf{k})$ (s. Fig. 10.3). While these measurements could demonstrate a transition from an algebraic to an exponential decay of phase coherence, the algebraic scaling exponent η could only be extracted as a trap-averaged quantity over an inhomogeneous density distribution. This complicated a quantitative interpretation of their results and yielded a scaling exponent of $\eta \approx 1.4$ at the critical temperature T_c - an increase by a factor of ~ 5 from the value of $\eta = 1/4$ expected for uniform systems.

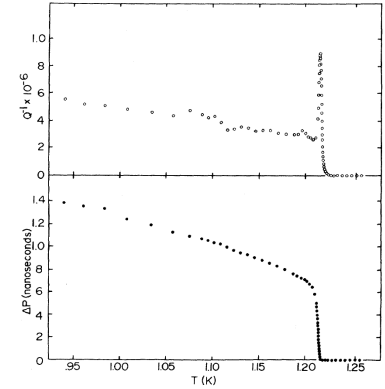


Figure 10.1: Observation of the superfluid jump in a thin helium film. In the experiment by Bishop and Reppy [202], 2D ^4He films are adsorbed on a Mylar substrate which is wound as a spiral on the axis of a torsional oscillator. The period shift ΔP and inverse dissipation Q^{-1} of this oscillator are measured for temperatures T around the critical temperature T_c . For $T < T_c$ the superfluid decouples from the substrate which results in abrupt changes of both ΔP and Q^{-1} thereby providing direct evidence for the predicted superfluid jump of the superfluid density at T_c [89]. Adapted from [202].

⁶² For more details on the BKT transition, see the review article by Hadzibabic and Dalibard [81] or chapter 3.2 of this thesis.

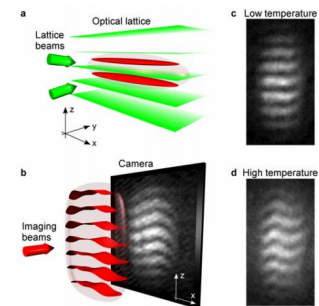


Figure 10.2: Study of the BKT transition in an ultracold 2D Bose gas. (a) Two 2D Bose gases are trapped in an optical lattice potential which creates a tight confinement along the z -axis. (b) After switching off the lattice, the clouds expand and interfere. The resulting interference patterns directly reveal the spatial coherence properties of each 2D cloud [203]. For low temperatures the straight interference pattern demonstrates quasi-long-range phase coherence (c), while for high temperatures the waviness of the fringes show enhanced phase fluctuations in the gas (d). Adapted from [144].

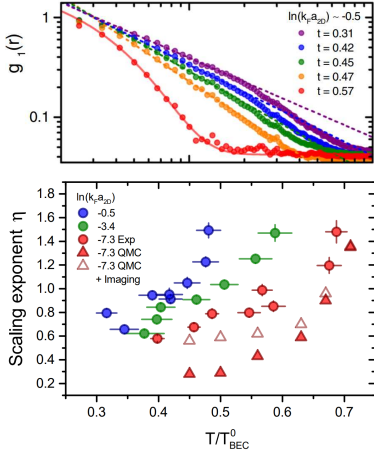


Figure 10.3: Phase correlations in a harmonically trapped 2D Fermi gas. As presented in [78], $g_1 = \text{F.T.}(\tilde{n}(\mathbf{k}))$ was reconstructed from the momentum distribution $\tilde{n}(\mathbf{k})$ obtained from matter wave focusing. The scaling exponent η was extracted from g_1 for various interaction strengths and temperatures, but was significantly influenced by the imaging system and the inhomogeneous density distribution. Adapted from [78].

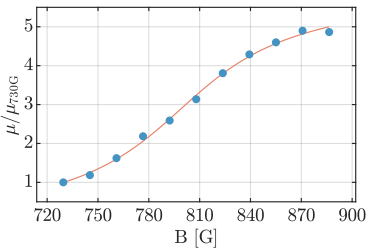


Figure 10.4: Chemical potential in the BEC-BCS crossover. Relative change of the chemical potential of our system for different magnetic fields, normalized to the chemical potential at a field of 730 G. The chemical potential is extracted from the initial slope of the EOS measurements shown in Fig. 8.7. The red line is a heuristic fit we use to keep V_0/μ constant during our measurements across the crossover (Fig. 10.5).

In addition, these measurements required a quench of the system to the weakly-interacting bosonic limit, since interactions during time of flight would otherwise alter the imaged momentum distribution - in particular in the strongly interacting regime.

In this chapter, we show that our Josephson junction can be used as a novel in-situ probe for phase coherence in strongly correlated 2D superfluids. We observe Josephson oscillations in the entire crossover from weakly bound Cooper pairs to deeply bound molecules and use our LC circuit model to extract the corresponding critical current of our junction in the 2D BEC-BCS crossover. For our ideal Josephson junction this critical current is directly linked to the condensate density n_c and the algebraic scaling exponent η , which we extract in the bosonic limit of our 2D Fermi gas. Our results provide a starting point to demonstrate the algebraic decay of phase coherence from the system size scaling of Josephson dynamics in a 2D quantum gas.

10.1 Results

10.1.1 Observation of Josephson oscillations and critical current in the 2D BEC-BCS crossover

Following our observation of a sinusoidal current phase relation presented in the previous chapter, we can finally use our Josephson junction as a probe for 2D superfluidity in the strongly correlated regime. To do this we prepare Josephson junctions in homogeneous 2D Fermi gases with various interaction strengths ranging from $\ln(k_F a_{2D}) \approx -3$ to $\ln(k_F a_{2D}) \approx 2$. To remain in the ideal Josephson regime, we maintain a constant $V_0/\mu = 1.4(2)$ by adjusting the barrier height V_0 for each interaction strength according to a reference measurement of the chemical potential μ (s. Fig. 10.4). Subsequently, we imprint a small initial phase difference of $\phi_0 \approx \pi/4$ and observe Josephson oscillations over a wide range of interaction strengths, indicating the presence of superfluidity in the entire crossover from tightly bound molecules to weakly bound Cooper pairs (s. Fig. 10.5).

To quantify the effect of interactions on our system we apply our LC circuit model to extract the critical current I_C from the frequency of the Josephson oscillations. We observe that, within the uncertainty of our measurement, the critical current stays nearly constant with a tendency towards smaller values of I_C when approaching the BCS side of the resonance.

10.1.2 Extracting the condensate density from the critical current in the bosonic limit

Since the critical current I_C for our ideal Josephson junctions is determined by the wave function overlap, we can use it to measure the condensate density n_c of our 2D Fermi gas. Very recently, such a measurement of the condensate density based on Josephson critical cur-

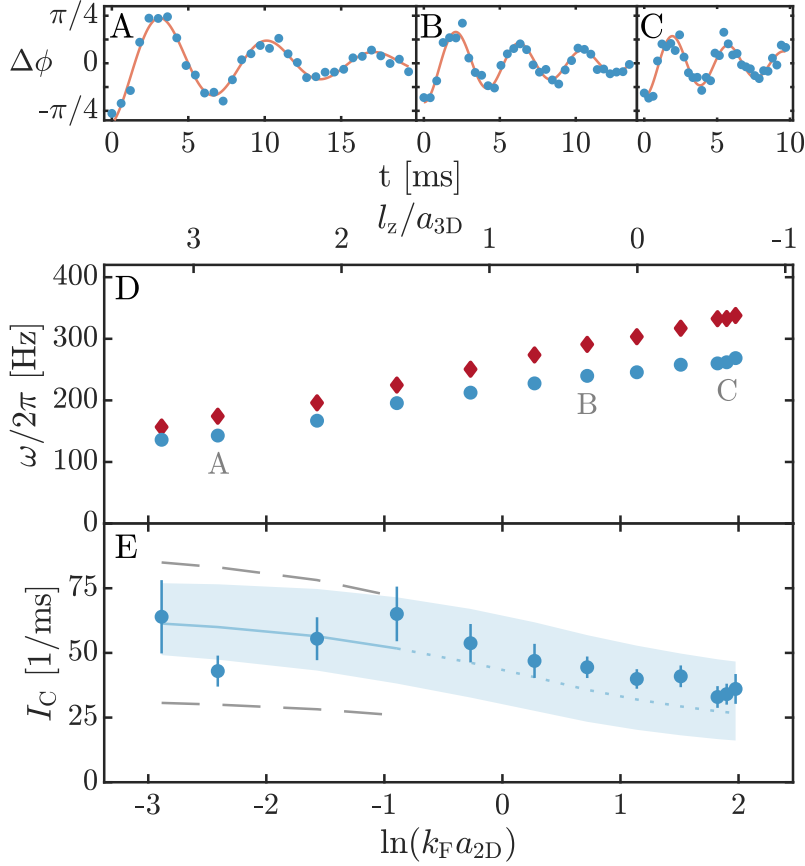


Figure 10.5: **Interaction dependence of the critical current.** Josephson oscillations for interaction strengths of $\ln(k_F a_{2D}) = -2.4$ (A), $\ln(k_F a_{2D}) = 0.7$ (B) and $\ln(k_F a_{2D}) = 1.9$ (C), where k_F is the Fermi wave vector and a_{2D} is the 2D scattering length as defined in [63]. The measurements are performed in the linear regime with constant density $n = 1.21(9)\mu\text{m}^{-2}$ and relative barrier height $V_0/\mu = 1.4(2)$. (D) Oscillation frequency for sound (red diamonds) and Josephson (blue dots) oscillations as a function of the 2D interaction parameter $\ln(k_F a_{2D})$. The frequency increase of the bare sound mode when going from the molecular to the BCS regime reflects the interaction dependence of the chemical potential. (E) Critical current of the junction extracted from the frequency difference between the sound mode and the Josephson oscillations. The error bars denote the 1σ fit error. The blue line is the critical current $I_C \propto n_c t_{k=0}$ calculated for a condensate fraction of $n_c/n = 0.72$ and a tunnelling amplitude $t_{k=0}$ obtained from a mean field calculation of the transmission through the barrier (s. section 10.2.2). To calculate the tunnelling amplitude we approximate our junction with a rectangular barrier with a width $b = 0.81\mu\text{m}$, which is a reasonable approximation for the Gaussian barrier used in the experiment. The shaded region denotes the systematic uncertainty resulting from the 15% uncertainty in V_0/μ . The dashed grey lines indicate the upper ($T = 0$) and lower ($T = T_c$) bound for the critical current obtained from our theory. While it is unclear how far into the strongly correlated regime our bosonic theory is quantitatively accurate, it reproduces the qualitative behaviour of our data across the entire BEC-BCS crossover. Each data point in (A, B, C) is obtained by averaging 42 individual measurements.

rents was performed in a 3D Fermi gas, where the expected decrease of the condensate fraction from the BEC to the BCS regime could be observed [193].

The key challenge to obtain the condensate density n_c from such a measurement of the critical current is a calculation of the tunnelling amplitude through the barrier. Following the theoretical work in [194], the authors of [193] expressed the critical current $I_C \propto n_c \sqrt{\mu} |t|(\mu)$ in terms of the chemical potential μ and the single particle tunnelling amplitude $|t|(\mu)$ for this energy μ and experimentally verified the validity of this expression for various barrier parameters. Motivated by this work on 3D systems [194], we derive an analytic expression for the critical current

$$I_C \approx \frac{2n_c A t_{\mathbf{k}=0}}{\hbar}, \quad (10.1)$$

of our 2D Josephson junction in the bosonic limit including phase fluctuations and mean field contributions to the tunnelling amplitude $t_{\mathbf{k}=0}$ inside the barrier (s. section 10.2.2) [194].

We use this theory to determine the condensate fraction from the measured critical current for interaction strengths $\ln(k_F a_{2D}) \leq -0.9$ and obtain $n_c/n = 0.72(8)_{\text{stat.}} \left(\begin{smallmatrix} +0.1 \\ -0.2 \end{smallmatrix} \right)_{\text{sys.}}$, where the systematic error arises from the 15% uncertainty in V_0/μ . For our homogeneous 2D system, Berezinskii-Kosterlitz-Thouless theory relates the condensate fraction $n_c/n \approx (l_\perp/\xi)^{-\eta}$ to the algebraic decay of phase coherence over the finite size l_\perp of the box, where ξ is the healing length of the condensate and η is the algebraic scaling exponent [81, 204]. Our measured critical current therefore corresponds to a scaling exponent of $\eta = 0.08(3)_{\text{stat.}} \left(\begin{smallmatrix} +0.07 \\ -0.04 \end{smallmatrix} \right)_{\text{sys.}}$, which agrees well with the scaling exponent $\eta \approx \frac{1}{4} \frac{T}{T_c} \approx 0.075$ expected for our temperature of $T/T_F \approx 0.03$ [62, 78, 81, 205]

10.1.3 System size scaling

Since we estimate the scaling exponent η from a single measurement of the critical current, there could in principle be small corrections to this value due to boundary effects of our box system or non-universal short range physics.⁶³ To explicitly show the algebraic scaling

$$I_c(L) \propto (1/L)^\eta \quad (10.2)$$

and avoid these corrections one could perform a measurement of the critical current as a function of system size L . Very recently, this expected algebraic scaling of the critical current was explicitly shown using full numerical simulations [198] of a system with comparable parameters to the ones used for our measurements shown in Fig. 10.5. In particular, the extracted value for η from the scaling of the critical current agrees well with our experimentally determined value in the bosonic limit (s. Fig. 10.6). This confirms that the Josephson critical current can be used to measure phase coherence in 2D superfluids.

⁶³ The short range behaviour of $g_1(r) = (r_0^2/(r_0^2 + r^2))^{\eta/2}$ can be expressed with a certain cutoff r_0 which for a 2D Bose gas was shown to be well approximated by $r_0 \approx \xi$, where ξ is the healing length of the gas [206].

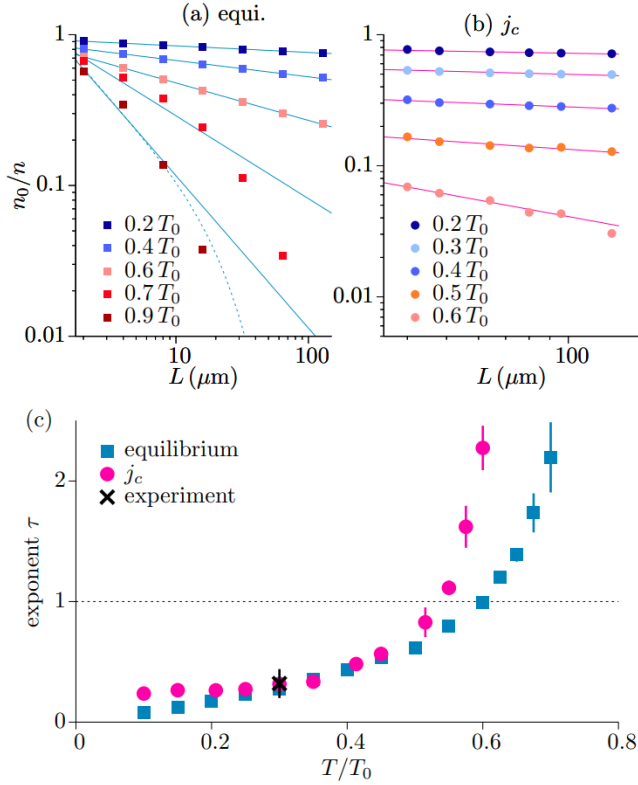


Figure 10.6: Algebraic scaling of the critical current. (a,b) The condensate fraction n_0/n of a 2D Bose gas with density $n \approx 2.25/\mu\text{m}^2$, interaction parameter $\tilde{g} = 1.8$ and varying size $L = 2 \mu\text{m}$ to $L = 128 \mu\text{m}$ is (a) determined directly from the equilibrium system and (b) extracted from the critical current I_c according to eq. 10.7 for a barrier of size $w/\xi = 2.9$ and averaged over multiple barrier heights from $V_0/\mu = 1.2$ to $V_0/\mu = 2$. For both (a) and (b), the condensate fraction decays algebraically with system size over a wide range of temperatures $T/T_0 = 0.2$ to $T/T_0 = 0.6$. The extracted scaling exponent $\tau = 4\eta$ from the critical current agrees well with the equilibrium value for a wide range of temperatures and with our experimentally determined value of η at a temperature of $T/T_0 \approx 0.3$ (black cross). Adapted from [198].

10.2 Methods

10.2.1 Equation of state

To keep our relative barrier height V_0/μ constant during our measurements of the critical current over the crossover, we need to measure the chemical potential μ as a function of interaction strength. We do this by following the approach established by Ref. [75]. We therefore define our chemical potential as $\mu = \mu_0 + \epsilon_B/2$, where μ is the chemical potential per atom and the contribution of the two-body binding energy ϵ_B is subtracted from the bare chemical potential μ_0 . We use DMD 2 to introduce a potential offset ΔV between the two sides of the box and measure the resulting density difference Δn (s. Fig. 8.7). For sufficiently small temperatures, the Thomas-Fermi approximation predicts $E_F = c \cdot \mu$, and we can obtain $\mu/E_F = 1/c$ from the linear slope of $\Delta n(\Delta V)$. The relative change in the measured chemical potential for different magnetic fields is shown in Fig. 10.4.

10.2.2 Derivation of the critical current in a phase fluctuating condensate

Here, we derive the analytic expression 10.7 for the critical current I_C of our 2D Josephson junction in the bosonic limit including phase fluctuations.⁶⁴

Generally, we can express the current between the left and right

⁶⁴ The analytic expressions for the critical current I_C and the tunnelling amplitude $t_{\mathbf{k}=0}$ presented in the following sections were derived by Ludwig Mathey. For more details see [198].

reservoir

$$\mathbf{I} = -\frac{i}{\hbar} \left(\sum_{\mathbf{k}} t_{\mathbf{k}} (a_1^\dagger(\mathbf{k}) a_r(\mathbf{k}) - a_r^\dagger(\mathbf{k}) a_1(\mathbf{k})) \right) \quad (10.3)$$

via the tunnelling amplitudes $t_{\mathbf{k}}$ and the bosonic creation and annihilation operators acting on the left and right reservoir. In the phase-density representation, neglecting density fluctuations, the annihilation operators are given by

$$a_{l/r}(\mathbf{k}) = \int \frac{d^2\mathbf{r}}{\sqrt{A}} \exp(-i\mathbf{k}\mathbf{r}) \sqrt{n_{l/r}} \exp(i\phi_{l/r} + i\delta\phi_{l/r}(\mathbf{r})) \quad (10.4)$$

where $A = L^2$ is the area of a box of size L , n_l (n_r) is the density, ϕ_l (ϕ_r) is the phase, and $\delta\phi_l$ ($\delta\phi_r$) is the fluctuation of the phase in the left (right) reservoir. To calculate the expectation value $\langle \mathbf{I} \rangle$, we insert eq. 10.4 in eq. 10.3 and assume independent Gaussian fluctuations of the phase in both reservoirs $\langle e^{i\delta\phi_{l/r}(\mathbf{r})} \rangle = e^{-\frac{1}{2} \langle \delta\phi_{l/r}^2(\mathbf{r}) \rangle}$. For a 2D system, we can further approximate the phase fluctuations to lowest order as $\langle \delta\phi_{l/r}^2(\mathbf{r}) \rangle = \eta \log(L/r_0)$, where $\eta = \frac{Mk_B T}{2\pi\hbar^2 n_s} = 2 \frac{n}{n_s} \frac{T}{T_F}$ is the algebraic scaling exponent and $r_0 \approx \xi$ is a short range cutoff on the order of the system's healing length ξ . To lowest order in k , we obtain

$$\langle \mathbf{I} \rangle = \frac{2nAt_{\mathbf{k}=0}}{\hbar} \left(\frac{L}{r_0} \right)^{-\eta} \sin \phi, \quad (10.5)$$

where $\phi = \phi_r - \phi_l$ is the phase difference across the barrier. This result reproduces the ideal current phase relation $I(\phi) = I_C \sin(\phi)$, where the critical current I_C is reduced by a factor of $\left(\frac{L}{r_0}\right)^{-\eta}$. Therefore, the critical current I_C is directly related to the algebraic decay of phase coherence in a 2D superfluid. Using the the condensate density

$$n_c \approx n(L/r_0)^{-\eta} \quad (10.6)$$

of a finite size 2D gas as defined in ref. [81] we finally get the critical current

$$I_C \approx \frac{2n_c A t_{\mathbf{k}=0}}{\hbar}. \quad (10.7)$$

10.2.3 Calculating the tunnelling amplitude

We calculate the tunnelling amplitude $t_{\mathbf{k}=0}$ for a rectangular potential barrier of width d and height V_B , centered around $x = 0$, with the following mean field ansatz

$$\psi(x) = \begin{cases} -\frac{1}{\sqrt{L}} \tanh((x + \delta)/(\sqrt{2}\xi)) & x < -d/2 \\ B \exp(-\kappa(x + d/2)) & x > -d/2, \end{cases} \quad (10.8)$$

with

$$\delta = \frac{d}{2} - \frac{\xi}{\sqrt{2}} \operatorname{arcsinh}\left(\frac{\sqrt{2}}{\kappa\xi}\right) \quad (10.9)$$

$$B = \frac{1}{\sqrt{L}} \tanh\left(\frac{1}{2} \operatorname{arcsinh}\left(\frac{\sqrt{2}}{\kappa\xi}\right)\right) \quad (10.10)$$

where $\xi = \hbar/\sqrt{2M\mu_B}$ is the healing length for a gas of bosons with mass M and chemical potential μ_B . Outside the barrier ($x < -d/2$), $\psi(x)$ is the exact solution to the Gross-Pitaevskii equation. Inside the barrier ($x > -d/2$), we obtain the approximative solution by minimising the energy

$$E = \frac{B^2}{2\kappa} \left(\frac{\hbar^2 \kappa^2}{2M} + V_B - \mu_B \right) + \frac{g}{2} \frac{B^4}{4\kappa} \quad (10.11)$$

which yields the characteristic decay exponent $\kappa = \sqrt{k_0^2 + k_B^2}$ with $k_0^2 = 2M(V_B - \mu_B)/\hbar^2$ and $k_B^2 = MgB^2/2\hbar^2$. Using the continuity of the wave function and its derivative at $z = -d/2$ we further get

$$\kappa^2 = k_0^2 + \frac{MgB^2}{2\hbar^2} = \frac{n}{2\xi^2} \left(1 - \frac{B^2}{n} \right)^2 \frac{1}{B^2} \quad (10.12)$$

and obtain

$$B^2 = \frac{n}{1 + k_0^2 \xi^2 + \sqrt{1/2 + 2k_0^2 \xi^2 + (k_0^2 \xi^2)^2}} \quad (10.13)$$

$$= n \frac{\mu_B}{V + \sqrt{V_B^2 - \mu_B^2/2}}. \quad (10.14)$$

Therefore, we finally obtain the tunnelling energy

$$t_{\mathbf{k}=0} = \frac{1}{L} \frac{\hbar^2 \kappa}{m} \frac{\mu_B}{V_B + \sqrt{V_B^2 - \mu_B^2/2}} \exp(-\kappa d), \quad (10.15)$$

which we insert into eq. 10.7 to obtain the critical current I_C .

We note that eq. 10.7 which relates the critical current to the condensate density has previously been derived for a 3D system [207] and was found to quantitatively describe the behaviour across the 3D BEC-BCS crossover for high barriers ($V \gg \mu$) [194]. Our derivation of the critical current extends the validity of this relation in the bosonic limit to $V \gtrsim \mu$ by including the mean field contribution to the tunnelling amplitude inside the barrier. Following the same reasoning and assumptions given in [194], it seems plausible that eq. 10.7 is quantitatively accurate beyond the bosonic case discussed above, but verifying this is beyond the scope of this work. A more detailed discussion of eq. 10.7 and its derivation is given in [198].

In this thesis, we have presented experiments with ultracold 2D Fermi gases which significantly advance their capability to simulate strongly correlated 2D superfluids.

As the main result, we have for the first time observed Josephson oscillations in an ultracold 2D Fermi gas which clearly shows phase coherence and provides strong evidence for superfluidity. We create our Josephson junction by connecting two homogeneous reservoirs through a narrow tunnelling barrier and initialise oscillations by controlling the initial phase difference between the reservoirs. This system enables us to study the Josephson effect between strongly correlated 2D superfluids in a clean and well-controlled environment.

We quantitatively understand the Josephson oscillations in an LC circuit model and extract the Josephson inductance L_J and critical current I_C of our junction from measurements of the oscillation frequency. To verify the validity of this circuit model we tune the size of the two reservoirs and show that the extracted Josephson inductance is only determined by the properties of the tunnelling barrier. Furthermore, our ability to control the phase difference between the reservoirs enables us to probe the current phase relation $I(\phi)$ of our junction. We measure the oscillation frequency as a function of phase difference across the junction and find that our junction follows the sinusoidal current phase relation $I(\phi) = I_C \sin(\phi)$ of an ideal Josephson junction. Finally, we tune the interaction strength of our 2D Fermi gas and observe that Josephson oscillations and hence our signature for superfluidity persists in the entire crossover from deeply bound dimers to weakly bound Cooper pairs. From these oscillations we determine the critical current I_C which for our ideal junction is only determined by the wave function overlap of the coupled superfluids. Thereby, we realise a novel probe for the order parameter of strongly correlated 2D superfluids which enables us to extract the condensate density and the BKT scaling exponent in the bosonic limit.

Our realisation of a Josephson junction was enabled by various experimental advances in the preparation, manipulation and characterisation of ultracold 2D Fermi gases, which were achieved during the course of this thesis. In particular, we improved our vacuum system and the cooling setup to achieve sufficiently low temperatures for 2D superfluidity. Furthermore, we implemented tailored optical potentials to create junction and box potentials and control the local phase of our system, and developed new methods to accurately determine the density and momentum distribution of our 2D Fermi gas. This unique level of control not only enabled our realisation of Josephson junctions, but will also provide the basis for various upcoming measurements to gain further insight into strongly correlated 2D superfluids.

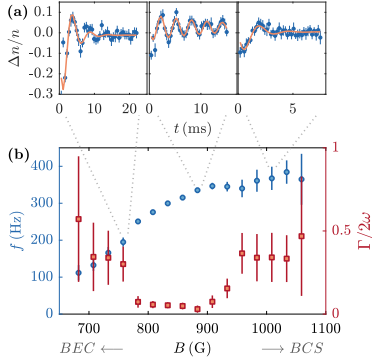


Figure 11.1: Sound propagation in a strongly interacting 2D Fermi gas. (a) Oscillations in the relative density imbalance $\Delta n/n = 2(n_t - n_b)/(n_t + n_b)$ in homogeneous 2D Fermi gases at magnetic offset fields of $B = 758$ G, $B = 883$ G and $B = 1009$ G, where n_t (n_b) denotes the density in the top (bottom) half of the box. Solid orange lines represent damped sinusoidal fits. (b) The oscillation frequency f continuously increases from the BEC to the BCS limit, while the damping rate Γ shows a pronounced minimum in the strongly correlated regime. Figure adapted from Bohlen et al. [208].

11.1 Outlook

11.1.1 Sound propagation and quantum limited damping in a 2D Fermi gas

These measurements were recently published in

M. Bohlen, L. Sobirey, N. Luick, H. Biss, T. Enss, T. Lompe, and H. Moritz, arXiv:2003.02713 (2020), under review in Physical Review Letters

and will be presented in detail in the PhD thesis of Markus Bohlen [209].

Our realisation of a Josephson junction in a 2D Fermi gas illustrates how transport measurements can be used as a tool to gain insight in strongly correlated quantum matter. Recently, we conducted a separate set of transport measurements in which we study the propagation and damping of sound modes in strongly interacting 2D Fermi gases [208].

For these measurements we use the methods developed in the context of our realisation of a Josephson junction described in chapter 8 and follow an approach similar to the one described in [210]: We prepare a homogeneous 2D Fermi gas trapped in a rectangular box potential, briefly apply a potential offset to one half of the system and observe the resulting density wave propagating between the boundaries of our box. We measure the frequency f and damping rate Γ of such density oscillations by determining the population difference Δn between the two halves of the box as a function of the time t after the potential offset was applied (s. Fig. 11.1).

While for a Josephson junction the oscillation frequency provides access to the wave function overlap of the coupled superfluids (s. chapter 10), without a potential barrier $f = v_s/2l_\perp$ is only determined by the speed of sound v_s and the size l_\perp of the box along the propagation direction of the sound mode. We extract v_s for various interaction strengths in the crossover from bosonic dimers to weakly bound Cooper pairs and compare it to the calculated value of $v_s = \sqrt{\frac{n}{m} \frac{\partial \mu}{\partial n}}|_s$ which we determine from a static measurement of the equation of state $\mu(n)$ (s. Fig. 8.7). We find excellent agreement between the dynamic and static measurement to determine v_s which suggests that our sound mode is well-described as a pure density wave at constant entropy [211].

Finally, we analyse the damping rate Γ of sound modes from which we extract the sound diffusion constant $D_s = k_0^2/\Gamma$, where $k_0 = \pi/l_\perp$ is the wave vector of the sound wave. We observe a minimum of $D = 1.8(2)\hbar/m$ in the strongly correlated regime which approaches the universal quantum bound of $D = \hbar/m$ expected for a perfect fluid [212]. This result suggests that scale invariance, which is broken for our strongly interacting 2D Fermi gas, is in fact not required for quantum limited transport.

11.1.2 Observation of superfluidity in a strongly-correlated 2D Fermi gas

These measurements were recently published in

*L. Sobirey, N. Luick, M. Bohlen, H. Biss, H. Moritz, T. Lompe,
arXiv:2005.07607 (2020), submitted to Science*

and will be presented in detail in the PhD thesis of Lennart Sobirey [214].

A hallmark manifestation of superfluidity is frictionless flow, where particles with a velocity smaller than a critical velocity v_c can flow through the system without dissipation. Whilst this thesis was written, we have performed measurements of v_c in a 2D Fermi gas to provide direct evidence for superfluidity in this system and thereby complement the demonstration of phase coherence provided by our realisation of Josephson junctions.

To measure v_c we follow an approach similar to the one described in [57, 215] by dragging a weak lattice potential with varying velocities v through the gas and determining the onset of dissipation.⁶⁵ We observe frictionless flow for small lattice velocities $v < v_c$ and a sharp onset of heating above v_c , thereby providing definitive evidence for superfluidity in a 2D Fermi gas (s. Fig. 11.2). We measure the critical velocity as a function of interaction strength and find that the gas is superfluid throughout the entire 2D BEC-BCS crossover with a maximum of v_c in the strongly correlated regime around $\ln(k_F a_{2D}) \approx 0$.

In contrast to previous measurements of v_c in ultracold quantum gases, we also see a decrease of dissipation for larger velocities $v > v_c$. This is due to the fact that our lattice creates excitations with a specific wave vector $k_0 = 2\pi/L$ determined by the lattice spacing L and therefore probes the excitation spectrum of the system at a constant k_0 (s. Fig. 11.2B). Our ability to tune the lattice spacing L therefore enables us to probe the excitation spectrum $\epsilon(k)$ of the gas at various wavevectors k . In particular, we observe that in the bosonic limit the critical velocity is found at low wave vectors $k_0 \ll k_F$ corresponding to phononic excitations, while on the BCS side the lowest-lying excitations are found at $k_0 = 2k_F$ determined by pair breaking excitations.

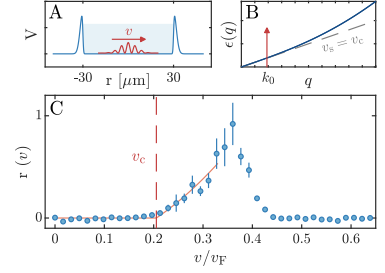


Figure 11.2: Measuring the critical velocity of a 2D Fermi gas. (A) Sketch of our experimental method to measure the critical velocity v_c . We prepare a homogeneous 2D Fermi gas trapped in a box potential (blue) and drag a weak attractive lattice potential (red) through the gas with a tunable phase velocity v . (B) Sketch of the Bogoliubov excitation spectrum $\epsilon(q)$. The lattice potential with spacing L probes the excitation spectrum at a specific wave vector $k_0 = 2\pi/L$ (red arrow). (C) We measure the response $r(v)$ of a 2D Fermi gas with interaction parameter $\ln(k_F a_{2D}) = -0.8$ for $k_0 \approx 0.15k_F$ and various lattice velocities v and observe a sharp increase of the response above a critical velocity v_c signalling the onset of dissipation. The response $r(v) = \tilde{n}(\mathbf{k} = 0, v = 0)/\tilde{n}(\mathbf{k} = 0, v) - 1$ is determined from the occupation of low momentum modes in the momentum distribution $\tilde{n}(\mathbf{k})$. Figure adapted from Sobirey et al. [213].

⁶⁵ Another approach to measure v_c in cold gases - in direct analogy to Landau's original thought experiment [216] - is to drag a small potential, realised i.e. by a tightly focused laser beam, through the gas. This was done to show superfluidity in 3D Bose gases [217], 2D Bose gases [218], and more recently in our measurement of the critical velocity v_c in the 3D BEC-BCS crossover [59].



CALIBRATING HIGH-INTENSITY ABSORPTION IMAGING

In this chapter, we report on a novel technique for the calibration of high intensity absorption imaging, which is published in

K. Hueck, N. Luick, L. Sobirey, T. Lompe, H. Moritz, L. Clark, and C. Chin, Opt. Express 25, 8670 (2017)

and reprinted here with minor modifications. I contributed to the conception and conduction of all measurements presented here, including the the writing of the publication.

abstract

Absorption imaging of ultracold atoms is the foundation for quantitative extraction of information from experiments with ultracold atoms. Due to the limited exposure time available in these systems, the signal-to-noise ratio is largest for high intensity absorption imaging where the intensity of the imaging light is on the order of the saturation intensity. In this case, the absolute value of the intensity of the imaging light enters as an additional parameter making it more sensitive to systematic errors. Here, we present a novel and robust technique to determine the imaging beam intensity in units of the effective saturation intensity to better than 5%. We do this by measuring the momentum transferred to the atoms by the imaging light while varying its intensity. We further utilize the method to quantify the purity of the polarization of the imaging light and to determine the correct imaging detuning.

A.1 Introduction

Ultracold atoms have added a completely new toolset to the study of quantum many-body systems by allowing direct imaging of density and momentum distributions. This led to the observation of striking features such as the bimodal momentum distribution signifying the onset of Bose-Einstein condensation [178, 179] or vortex lattices in rotating superfluids[219, 220]. Ultracold atoms have also been used for precision measurements such as the extraction of the equation of state [58, 147] from an accurate measurement of the density distribution of the system. The most common method to measure such density distributions is absorption imaging: the atoms are illuminated with a short pulse of resonant light and the shadow cast by the atoms is imaged onto a camera. The fraction of light transmitted through the system decreases exponentially according to the Beer-Lambert law, provided the atomic transition is not saturated. In this case the density distribution integrated along the imaging direction n_{2D} can be ex-

tracted from a relative measurement which compares images with and without atoms. Hence, no knowledge of the absolute intensities is required.

However, absorption imaging with intensities well below the saturation intensity has clear limitations. One prominent issue is the imaging of optically dense clouds, where the number of photons transmitted through the sample and hence the signal-to-noise ratio becomes very small. This can either be solved by using techniques such as phase contrast imaging [221] or by simply saturating the transition so that more photons are transmitted [145, 147, 222]. Imaging in the saturated regime is also helpful when a high spatial resolution is desired. To this end, it is essential to minimize the motion of atoms caused by the recoil from scattered photons during the imaging pulse. The motional blurring is minimized by utilizing short imaging times with high intensities.

For absorption imaging with higher intensities a new scale appears: the saturation intensity I_{sat} . This implies that the column density can no longer be determined from a purely relative measurement of two intensities. Rather, the absolute intensities transmitted with and without atoms present have to be known in order to extract an atomic density. However, determining the imaging beam intensity I at the position of the atoms is prone to systematic errors. Additionally, imperfect polarization of the imaging light can lead to a reduced scattering cross-section and hence an increased effective saturation intensity I_{sat}^{eff} .

Here, we present a novel technique which allows for a precise and robust calibration of high intensity absorption imaging. It is based on measuring the momentum transferred to the atoms by the imaging pulse which is directly proportional to the number of scattered photons. The beam intensity I for which the transferred momentum and hence the photon scattering rate is equal to half its maximum value corresponds to the effective saturation intensity I_{sat}^{eff} . Measuring the momentum transfer also allows to determine the polarization purity of the imaging light at the position of the atoms as well as the detuning Δ .

The manuscript is organized as follows: In section two a brief review of strong saturation imaging is given and section three describes the experimental setup. In the fourth section, we describe our method to measure the momentum transfer and apply it to determine I/I_{sat}^{eff} , the correct detuning and the polarization purity of the imaging beam. In section five we summarize the results.

A.2 High intensity imaging

Here, we provide a short summary of the theory of resonant saturated absorption imaging. When the saturation of an optical transition becomes relevant, the Beer-Lambert law is modified to

$$\frac{dI(x, y, z)}{dz} = -n(x, y, z)\sigma_{eff} \frac{1}{1 + I(x, y, z)/I_{sat}^{eff}} I(x, y, z), \quad (\text{A.1})$$

where n is the atom density and $I(x, y, z)$ the intensity at position (x, y) of the imaging light propagating along the z -direction [145]. $\sigma_{eff} = \frac{\sigma_0}{\alpha}$ and $I_{sat}^{eff} = \alpha I_{sat}^0$ are the effective cross-section and effective saturation intensity. Here, a parameter $\alpha > 1$ was introduced to capture effects of non-perfect polarization or magnetic field orientation which reduces the cross-section and saturation intensity in a two-level system from its ideal values $\sigma_0 = \frac{3\lambda^2}{2\pi}$ and $I_{sat}^0 = \frac{\pi}{3} \frac{hc\Gamma}{\lambda^3}$ [223]. Here, h is Planck's constant, c the speed of light, λ is the wavelength and Γ the natural linewidth of the imaging transition. Integration of Eq. (A.1) along z then yields the optical column density

$$\text{od}(x, y) = \sigma_{eff} n_{2D}(x, y) = \sigma_{eff} \int_{-\infty}^{\infty} n(x, y, z) dz = \underbrace{-\ln\left(\frac{I_{out}(x, y)}{I_{in}(x, y)}\right)}_{\text{Log-Term}} + \underbrace{\frac{I_{in}(x, y) - I_{out}(x, y)}{I_{sat}^{eff}}}_{\text{Lin-Term}}, \quad (\text{A.2})$$

with I_{in} and I_{out} being incident and transmitted intensities, respectively. When the intensities are small compared to the saturation intensity the linear term can be neglected and we recover the simple Beer-Lambert law which only depends on relative intensities. However, for higher intensities the linear term becomes significant and the intensities have to be known in units of the effective saturation intensity.

Furthermore, the intensities $I_{in}(x, y)$ and $I_{out}(x, y)$ read out from a pixel (i, j) of the camera are given in units of count rates, which will be denoted $C_{in}(i, j)$ and $C_{out}(i, j)$ in the following. The count rate is related to the intensity by

$$C = \frac{IA_{pix}/M^2}{hc/\lambda} \times T \times QE \times G, \quad (\text{A.3})$$

where A_{pix} is the area of a camera pixel, M the magnification of the imaging system, T the transmission through the imaging system, QE the quantum efficiency and G the conversion factor between counts and photo-electrons of the camera. Expressing Eq. (A.2) in counts C leads to

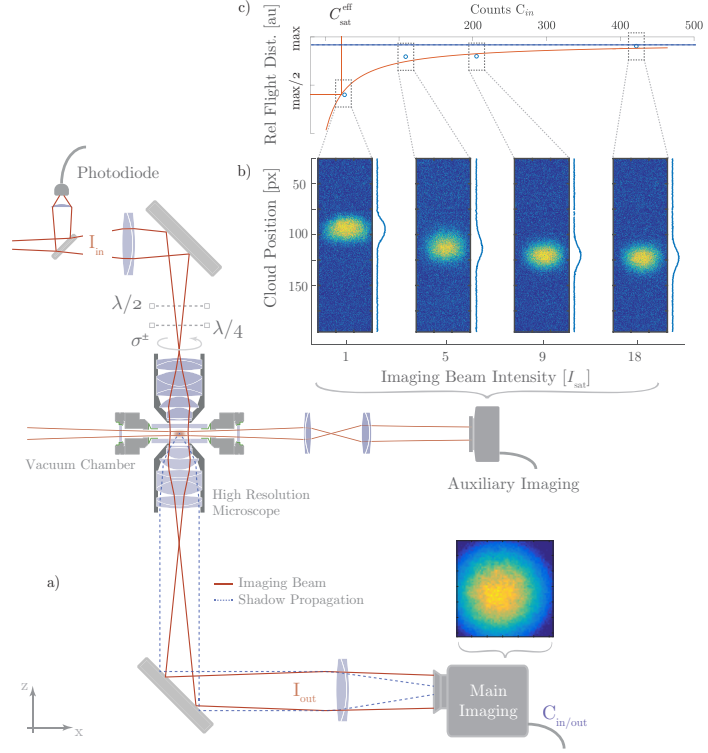
$$\sigma_{eff} n_{2D}(i, j) = -\ln\left(\frac{C_{out}(i, j)}{C_{in}(i, j)}\right) + \frac{C_{in}(i, j) - C_{out}(i, j)}{C_{sat}^{eff}}. \quad (\text{A.4})$$

It becomes apparent that with an independent measurement of C_{sat}^{eff} there is no need to know T , QE and G . The problem hence reduces to finding the number of counts C_{sat}^{eff} on the camera corresponding to the effective saturation intensity and the effective cross-section σ_{eff} . Knowledge of σ_{eff} is also necessary for low intensity imaging.

A.3 Experimental setup

The experimental setup is designed to produce, manipulate and image two-dimensional superfluids of ^6Li atoms with high spatial resolution [140]. The imaging system along the z -direction has a numerical aperture of 0.62 and thus a very limited depth of field of about

Figure A.1: Sketch of the experimental setup: a) Absorption imaging of a cloud of ultracold atoms trapped inside a vacuum chamber. Imaging of the cloud is possible along two axes, the main axis (z-axis) and an auxiliary imaging axis (x-axis). By flashing on the main imaging beam, the atoms accelerate in z-direction. After some time of flight their position is recorded with the auxiliary imaging. b) Density distributions after $80 \mu\text{s}$ time of flight imaged along the auxiliary imaging direction. The flight distances shown in c) are extracted from the images and plotted as a function of the intensity of the imaging pulse, which is measured on the main imaging camera. From the saturation of the flight distance we can determine the count rate on the main imaging camera which corresponds to the effective saturation intensity.



$2 \mu\text{m}$. Hence, short imaging pulses are required to minimize the motion along the optical axis as well as the random walk in xy -plane during the imaging process in order to avoid motion blurring. In our ${}^6\text{Li}$ experiment we typically use $5 \mu\text{s}$ imaging pulses with a saturation parameter $s_0 = 1$. This causes motional blurring of about $1.5 \mu\text{m}$ [221]. Under this condition it is therefore advantageous to use high intensity imaging to maximize the number of scattered photons, since the signal-to-noise ratio in absorption imaging is typically limited by photon shot noise. The quantization axis for the atoms is given by a magnetic field parallel to the optical axis. Therefore, the absorption cross-section on the ${}^2\text{S}_{1/2}, F=1/2$ to ${}^2\text{P}_{3/2}, F=3/2$ imaging transition is maximal for circularly polarized light.

The imaging laser light is generated by a frequency stabilized narrow linewidth diode laser which is frequency shifted by an acousto-optical deflector (AOD) in double pass configuration. This AOD setup enables chirping the imaging frequency with high ramp rates exceeding $5 \text{ MHz}/\mu\text{s}$ using a direct digital synthesis (DDS) frequency source. The imaging light intensity is controlled via a sample and hold feedback loop.

For the measurements presented in the following, we work with about 60×10^3 atoms per spin state in the two lowest hyper fine states of ${}^6\text{Li}$ at a magnetic offset field of 950 G . The atoms are magnetically trapped in the radial direction (trapping frequencies $\nu_x \approx \nu_y \approx 27 \text{ Hz}$). The tight confinement in z -direction is realized by a highly elliptic dipole trap featuring a trapping frequency of about 0.5 kHz . In order to avoid multiple scattering effects during the calibration measurements the optical density $\text{od}(x, y)$ along the z -direction as well as

the atomic density $n(x, y, z)$ is chosen to be low. We note that optically thin samples $od(x, y) < 1$ are only required for calibration. Once the effective saturation count rate C_{sat}^{eff} is known, optically thick samples can be imaged by using high intensities to saturate the imaging transition. However, to avoid collective scattering effects during the imaging, the condition that the inter-particle spacing $1/n(x, y, z)$ has to be larger than the imaging wavelength λ still has to be fulfilled [224].

A.4 Method

A.4.1 Previous work

There exist two closely related approaches to determine I_{sat}^{eff} or C_{sat}^{eff} in the literature [145, 225, 226], which rely on taking absorption images of clouds with constant atom numbers while scanning over a wide range of imaging intensities I_{in} . For an assumed value of $\alpha = \frac{\sigma_0}{\sigma^{eff}}$ the total atom number $N(I_{in}, \alpha)$ for each intensity can be determined by evaluating Eq. (A.2) or (A.4) for all pixels and integrating over the atomic density distribution.

Ries et al. [225] and Horikoshi et al. [226] determine C_{sat}^{eff} by requiring $N(I_{in}, \alpha)$ to be independent of I_{in} . α is still a free parameter and has to be determined by an independent measurement, e.g. by comparing the measured equation of state to a theory prediction [226].

Reinaudi et al. [145] calculate the intensity of the imaging beam I_{in} at the position of the atoms from measurements of the imaging beam power and the transmission of the imaging system. The parameter α is found by requiring $N(I_{in}, \alpha)$ to be independent of I_{in} .

A.4.2 This work

The method described in this work neither requires a power measurement of the imaging beam nor a constant atom number during the calibration process. The basic principle is depicted in Fig. A.1. We accelerate the cloud of atoms in z -direction by illuminating it with a short pulse from the main imaging beam after the dipole traps are switched off. The momentum transferred to each atom during the pulse is proportional to the number of scattered photons. Subsequently, the transferred momentum is determined by recording the flight distance of the accelerated cloud after some time of flight with an auxiliary imaging system along an orthogonal direction. The momentum transferred to the atoms saturates with increasing intensity I_{in} since the resonant photon scattering rate γ saturates according to

$$\gamma(s) = \frac{\Gamma}{2} \frac{s_0}{1 + s_0}. \quad (\text{A.5})$$

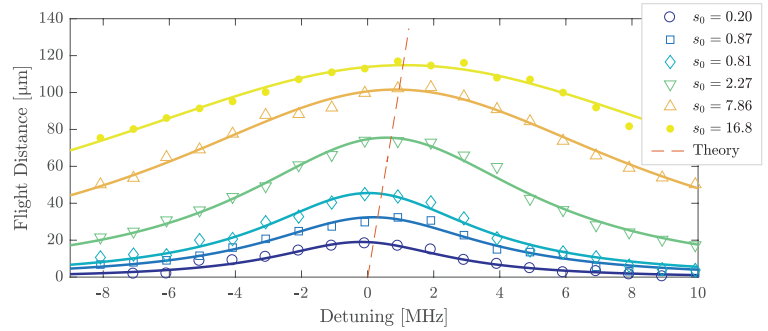
Here, Γ is the natural linewidth of the imaging transition and $s_0 = \frac{I_{in}}{\Gamma_{sat}^{eff}} = \frac{C_{in}}{C_{sat}^{eff}}$ denotes the on resonant saturation parameter which is given by the ratio of the imaging beam intensity to the effective saturation

intensity. The intensity for which the atoms traveled half their maximum flight distance corresponds to I_{sat}^{eff} . Hence, the magnification of the auxiliary imaging system drops out of the determination of the effective saturation intensity and therefore does not need to be known. Note that Eq. (A.5) only holds true if the imaging beam is resonant with the atoms.

A.4.3 Detuning determination

To determine the resonance frequency we apply imaging pulses with different detunings and maximize the transferred momentum to the atoms. A $1\ \mu\text{s}$ long pulse of imaging light along the z -direction is ap-

Figure A.2: Flight distance vs. laser detuning: The resonance frequency of the imaging laser is found by varying the detuning and thereby maximizing the flight distance of the atoms after illumination with a $1\ \mu\text{s}$ long imaging pulse. A Lorentzian fit (solid lines) to the data gives the center frequency as well as the width of the imaging transition, which shows power broadening for high intensities. The saturation parameter $s_0 = I/I_{sat}^{eff}$ for the different curves is extracted from the fits. The red dashed line indicates the theoretically expected position of the maxima which are affected by the accumulated Doppler shift during the imaging pulse. The x-axis is offset by the fitted resonance frequency.



plied to accelerate the atom cloud and after $80\ \mu\text{s}$ time of flight, the position of the atom cloud is recorded using the auxiliary imaging. Then, the center of mass of the atom cloud is found by performing a Gaussian fit to the recorded density profile. The resulting center positions are plotted in Fig. A.2 for different detunings and imaging intensities. The functional form is expected to be captured by a Lorentzian curve resembling the resonance behavior of the atomic transition. A fit of the form

$$z(\nu_L, s) = z_0 + \eta \frac{\Gamma}{2} \frac{s_0}{1 + s_0 + \left(\frac{2\Delta}{\Gamma}\right)^2} \quad (\text{A.6})$$

yields the detuning $\Delta = \nu_L - \nu_A$ between the atomic resonance frequency ν_A and the laser frequency ν_L . Here, η is the conversion from position difference on the camera to the scattering rate and is left as a fit parameter as well as the saturation parameter s_0 , and z_0 is the initial position of the atoms and Γ the linewidth of the imaging transition. As shown in Fig. A.2 the results are well described by Eq. (A.6). For higher saturation parameters s_0 the resonance is blue-shifted since the atoms accumulate a Doppler shift during the acceleration (see section A.4.4). However, for imaging intensities $s_0 \leq 1$ and illumination times $t \leq 1\ \mu\text{s}$ the shift of the fitted detuning is smaller than the fitting error. The fitting error of the detuning is typically below 200 kHz which is less than 4% of the linewidth of the ${}^6\text{Li}$ D2 line.

Our method has two clear advantages over the common method

of finding the resonant laser frequency by maximizing the apparent atom number as determined by Eq. (A.2). It is independent of fluctuations in the atoms number. Furthermore, it is not influenced by effects such as lensing in a dense atom cloud imaged off-resonance which can systematically shift the apparent atom number maximum away from the correct resonance frequency.

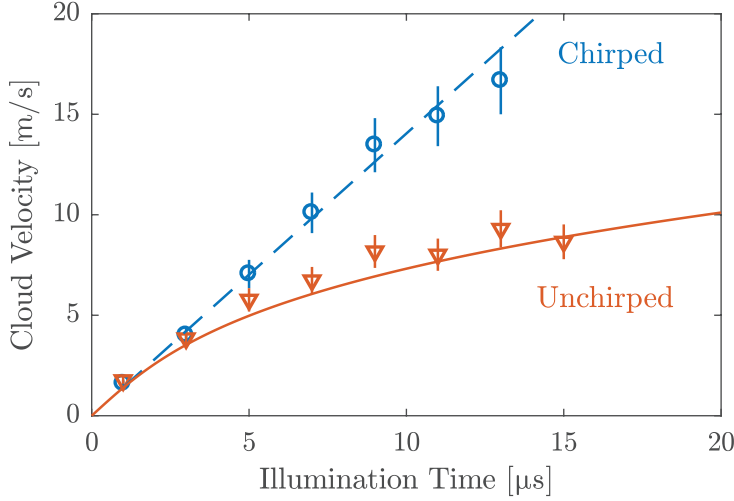


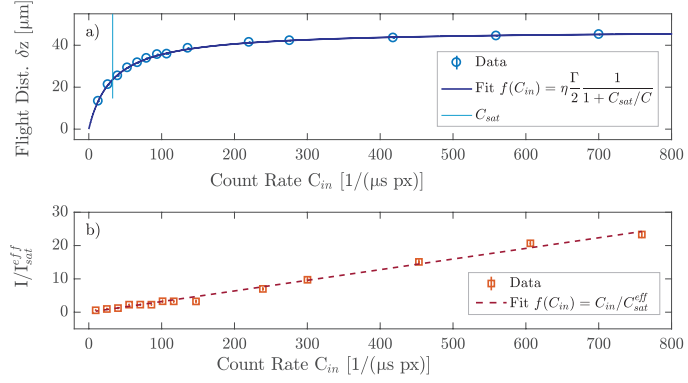
Figure A.3: Chirp efficiency: Velocity of the atom cloud after accelerating it with the z-imaging beam with different illumination times at $I_{in} = 3.75I_{sat}^{eff}$. The effect of chirping the imaging beam frequency to compensate for the Doppler shift is clearly visible. In the unchirped case (red triangles), the scattering rate decreases with illumination time and therefore the increase in cloud velocity becomes nonlinear. In the chirped case (blue open circles) acceleration is constant. The lines indicate the theoretically expected cloud velocity for the unchirped (red solid) and chirped case (blue dashed). The error bars indicate the systematic error estimated for the magnification of the auxiliary imaging.

A.4.4 Doppler shift compensation

For ${}^6\text{Li}$ the small mass causes the atoms to acquire a significant Doppler shift of $\Gamma/2$ in only $2.5 \mu\text{s}$ when imaging with saturation intensity. To be able to scatter more photons and hence increase the signal-to-noise ratio we compensate for the Doppler shift by performing a frequency chirp on the imaging laser frequency during the imaging. To find the chirp rate m which exactly compensates for the Doppler shift we adjust the chirp rate such that we maximize the momentum transferred by the imaging pulse to the atoms. A typical chirp rate required for ${}^6\text{Li}$ is on the order of $1.5 \text{ MHz}/\mu\text{s}$ for $I/I_{sat}^{eff} = 1$.

We verify the found chirp rate by accelerating the cloud of atoms with an imaging beam pulse with varying lengths up to $15 \mu\text{s}$ and an intensity of $I_{in} = 3.75I_{sat}^{eff}$. The velocity of the cloud after the acceleration is determined from position measurements after two different times of flight. The experimental result as well as a theory calculation is shown in Fig. A.3. Without chirping the laser frequency the atoms are Doppler shifted out of resonance during the illumination, the scattering rate decreases and the increase in velocity becomes nonlinear (red triangles). In the chirped case (blue circles) this effect vanishes and the increase in velocity scales linearly with the illumination time, which indicates a constant photon scattering rate. In both cases the accumulated velocity is in excellent agreement with the theoretical expectation (dashed and solid lines).

Figure A.4: Determination of the effective saturation count rate C_{sat}^{eff} . The difference in position for two times of flight ($\Delta t = 10 \mu s$) is shown as a function of imaging beam intensity and hence C_{in} . The velocity of the cloud saturates for higher imaging beam intensities and the saturation counts are determined by fitting Eq. (A.5) to the data. The resulting effective saturation count rate is $C_{sat,k}^{eff} = (32.7 \pm 0.6) (\text{px } \mu s)^{-1}$. b) The saturation parameter s_0 extracted from a Lorentzian fit to the power broadened spectra presented in Fig. A.2 is plotted as a function of the count rate C_{in} on the main camera. The error bars represent the Lorentzian fit error. A linear fit to the data yields $C_{sat,s}^{eff} = (31.5 \pm 1.3) (\text{px } \mu s)^{-1}$.



A.4.5 Effective saturation count rate

Here, we present two independent methods to determine the effective saturation count rate C_{sat}^{eff} . For both methods we utilize the measurement of momentum transferred from the imaging beam to the atoms. The first method is based on the saturation of the photon scattering rate for higher imaging beam intensities, while the second relies on the power broadening of the optical transition. Both methods feature errors below 5% and are in agreement to each other. Furthermore, the first method has also been used successfully in an experiment using ultracold ^{133}Cs [147].

For the first method the position difference after two times of flight of the atom cloud is measured for a pulse duration of $5 \mu s$ and different imaging beam intensities (see Fig. A.4 upper panel). Two different times of flight are used in order to determine the mean velocity of the cloud after the momentum transfer. This ensures, that only relative times and flight distances are compared and potential timing offsets cancel out. Fitting the measured flight distance using Eq. (A.6) with the detuning fixed to $\Delta = 0$ and $C_{sat,k}^{eff}$ and η as free parameters yields the saturation count rate for the system to high precision. In addition, the fitted value for η can also be used to extract the magnification of the auxiliary imaging system.

For the second method, C_{sat}^{eff} is determined from the power broadening of the imaging transition. To do this we use the fitted saturation parameters s_0 from the detuning measurements shown in Fig. A.2. We plot the values for s_0 against their corresponding counts C_{in} on the main camera in the lower panel of Fig. A.4. A linear fit to the values for s_0 directly results in $C_{sat,s}^{eff}$. In the following we use the mean value $C_{sat}^{eff} = (C_{sat,s}^{eff} + C_{sat,k}^{eff})/2$ of the two measurements.

A.4.6 Polarization purity

Since we image on a σ^- -transition along the magnetic field axis, any deviation from perfectly circularly polarized light reduces the effective absorption cross-section. To check the purity of the polarization we use the orthogonal polarization σ^+ , for which σ_{eff} should be zero.

First, we adjust for σ^+ -polarization by minimizing the residual acceleration at a high beam intensity of $I^+ = 25I_{sat}^{eff}$. This residual acceleration is directly proportional to the number of scattered photons. We then set the polarization back to σ^- and find the value of the imaging beam intensity I^- for which we scatter the same amount of photons. The purity of the polarization is now simply given by the ratio of the two intensities $p = I^-/I^+$. This results in a lower bound for the polarization purity of $p > 99.6\%$. This includes a possible mismatch between the magnetic field axis and the propagation direction of the imaging light. Hence, it is valid to approximate $\alpha = 1$.

A.4.7 Validation

Finally, we validate the effective saturation count rate C_{sat}^{eff} against the experiment. For that, we take density images of identically prepared clouds with different imaging beam intensities and extract atom numbers according to Eq. (A.4) using the previously determined values of C_{sat}^{eff} and α . If C_{sat}^{eff} was determined correctly, Eq. (A.4) should result in constant densities regardless the imaging beam intensity used. We find the extracted atom number to be independent of I_{in} as can be seen in the upper panel in Fig. A.5. This validates our method of determining C_{sat}^{eff} .

Furthermore, we evaluate the signal-to-noise ratio of the absorption images by evaluating the single pixel standard deviation for 70 subsequently taken images (Fig. A.5, lower panel, blue triangles). The signal-to-noise ratio is maximized for intensities around $I_{in} \approx 1.5I_{sat}^{eff}$.

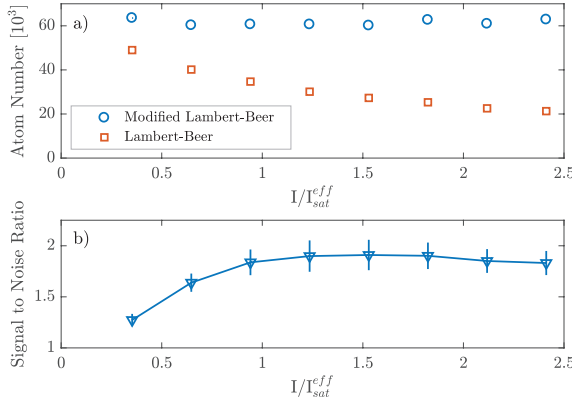


Figure A.5: Proof of validity and optimization of signal-to-noise ratio: a) Extracted atom number as a function of imaging beam intensity using the modified (blue circles) and unmodified (red squares) Beer-Lambert law. Each data-point is an average of about ≈ 70 measurements. The error-bars are smaller than the size of the symbols. When evaluating the data with the modified Beer-Lambert law the atom number does not depend on the imaging intensity. This validates our method to determine the value of the effective saturation intensity I_{sat}^{eff} . For low imaging intensities the result from the unmodified Beer-Lambert law approaches the correct atom number. b) The signal-to-noise ratio evaluated on a single pixel basis is maximized for intensities of $I = 1.5I_{sat}^{eff}$. The blue line is a guide to the eye.

A.5 Conclusion

In this work we have presented a novel technique to calibrate all parameters necessary to measure atomic densities using high intensity absorption imaging. These parameters include the detuning Δ , the effective saturation count rate C_{sat}^{eff} , the polarization purity p and hence α and finally the chirp rate required to compensate for Doppler shifts during the imaging. This allows for an intensity independent determi-

nation of the atomic column density n_{2D} . Thus, the intensity can freely be set to a value maximizing the signal-to-noise ratio. The presented method only relies on relative measurements of the momentum transferred to the atoms by illuminating them with a resonant laser beam which makes it robust against systematic errors. This makes the presented method a valuable tool for precision measurements of ultracold gases, especially as it is easily adapted to other experiments using different atomic species.

BIBLIOGRAPHY

- ¹P. W. Anderson: *More is different*, "Science" vol. 177, no. 4047, 393–396 (1972) (cited on page 3).
- ²J. G. Bednorz and K. A. Müller: *Possible high T_c superconductivity in the Ba- La- Cu- O system*, "Zeitschrift für Physik B Condensed Matter" vol. 64, no. 2, 189–193 (1986) (cited on page 3).
- ³A. Schilling, M. Cantoni, J. Guo, and H. Ott: *Superconductivity above 130 K in the Hg–Ba–Ca–Cu–O system*, "Nature" vol. 363, no. 6424, 56–58 (1993) (cited on page 3).
- ⁴A. Drozdov, P. Kong, V. Minkov, S. Besedin, M. Kuzovnikov, S. Mozaffari, L. Balicas, F. Balakirev, D. Graf, V. Prakapenka, et al.: *Superconductivity at 250 K in lanthanum hydride under high pressures*, "Nature" vol. 569, no. 7757, 528 (2019) (cited on page 3).
- ⁵M.-K. Wu, J. R. Ashburn, C. Torng, P. H. Hor, R. L. Meng, L. Gao, Z. J. Huang, Y. Wang, and a. Chu: *Superconductivity at 93 K in a new mixed-phase Y-Ba-Cu-O compound system at ambient pressure*, "Physical Review Letters" vol. 58, no. 9, 908 (1987) (cited on page 3).
- ⁶H. Maeda, Y. Tanaka, M. Fukutomi, and T. Asano: *A new high-T_c oxide superconductor without a rare earth element*, "Japanese Journal of Applied Physics" vol. 27, no. 2A, L209 (1988) (cited on page 3).
- ⁷C. Tsuei and J. Kirtley: *Pairing symmetry in cuprate superconductors*, "Reviews of Modern Physics" vol. 72, no. 4, 969 (2000) (cited on pages 3, 4, 62).
- ⁸W. Qing-Yan, L. Zhi, Z. Wen-Hao, Z. Zuo-Cheng, Z. Jin-Song, L. Wei, D. Hao, O. Yun-Bo, D. Peng, C. Kai, et al.: *Interface-induced high-temperature superconductivity in single unit-cell FeSe films on SrTiO₃*, "Chinese Physics Letters" vol. 29, no. 3, 037402 (2012) (cited on page 3).
- ⁹J.-F. Ge, Z.-L. Liu, C. Liu, C.-L. Gao, D. Qian, Q.-K. Xue, Y. Liu, and J.-F. Jia: *Superconductivity above 100 K in single-layer FeSe films on doped SrTiO₃*, "Nature Materials" vol. 14, no. 3, 285 (2015) (cited on page 3).
- ¹⁰Y. Cao, V. Fatemi, S. Fang, K. Watanabe, T. Taniguchi, E. Kaxiras, and P. Jarillo-Herrero: *Unconventional superconductivity in magic-angle graphene superlattices*, "Nature" vol. 556, no. 7699, 43 (2018) (cited on pages 3, 6).
- ¹¹N. D. Mermin and H. Wagner: *Absence of ferromagnetism or anti-ferromagnetism in one-or two-dimensional isotropic Heisenberg models*, "Physical Review Letters" vol. 17, no. 22, 1133 (1966) (cited on pages 3, 18, 87).
- ¹²P. C. Hohenberg: *Existence of long-range order in one and two dimensions*, "Physical Review" vol. 158, no. 2, 383 (1967) (cited on pages 3, 18, 87).

- ¹³J. M. Kosterlitz and D. J. Thouless: *Ordering, metastability and phase transitions in two-dimensional systems*, “Journal of Physics C: Solid State Physics” vol. 6, no. 7, 1181 (1973) (cited on pages 3, 18, 87).
- ¹⁴V. Berezinsky: *Destruction of long range order in one-dimensional and two-dimensional systems having a continuous symmetry group. I. Classical systems*, “Zh. Eksp. Teor. Fiz.” vol. 32, 493–500 (1970) (cited on pages 3, 18, 87).
- ¹⁵V. Berezinsky: *Destruction of Long-range Order in One-dimensional and Two-dimensional Systems Possessing a Continuous Symmetry Group. II. Quantum Systems*. “Zh. Eksp. Teor. Fiz.” vol. 61, 610 (1972) (cited on page 3).
- ¹⁶Y. Uemura: *Bose-Einstein to BCS crossover picture for high-Tc cuprates*, “Physica C: Superconductivity” vol. 282, 194–197 (1997) (cited on page 3).
- ¹⁷Y. Uemura: *Superfluid density of high-Tc cuprate systems: implication on condensation mechanisms, heterogeneity and phase diagram*, “Solid state communications” vol. 126, no. 1-2, 23–38 (2003) (cited on page 3).
- ¹⁸J. Bardeen, L. N. Cooper, and J. R. Schrieffer: *Theory of superconductivity*, “Physical Review” vol. 108, no. 5, 1175 (1957) (cited on page 3).
- ¹⁹P. A. Lee, N. Nagaosa, and X.-G. Wen: *Doping a Mott insulator: Physics of high-temperature superconductivity*, “Reviews of modern physics” vol. 78, no. 1, 17 (2006) (cited on page 4).
- ²⁰P. W. Anderson, P. Lee, M. Randeria, T. Rice, N. Trivedi, and F. Zhang: *The physics behind high-temperature superconducting cuprates: the ‘plain vanilla’ version of RVB*, “Journal of Physics: Condensed Matter” vol. 16, no. 24, R755 (2004) (cited on page 4).
- ²¹P. W. Anderson: *The resonating valence bond state in La₂CuO₄ and superconductivity*, “science” vol. 235, no. 4793, 1196–1198 (1987) (cited on pages 4, 5).
- ²²E. Gull and A. Millis: *Ten years of Nature Physics: Numerical models come of age*, “Nature Physics” vol. 11, no. 10, 808 (2015) (cited on pages 4, 5).
- ²³J. Hubbard: *Electron correlations in narrow energy bands*, “Proceedings of the Royal Society of London. Series A. Mathematical and Physical Sciences” vol. 276, no. 1365, 238–257 (1963) (cited on page 4).
- ²⁴S. Yamada, T. Imamura, and M. Machida: *16.447tflops and 159-billion-dimensional exact-diagonalization for trapped fermion-hubbard model on the earth simulator*, “SC’05: Proceedings of the 2005 ACM/IEEE Conference on Supercomputing”, 44–44 (2005) (cited on page 4).
- ²⁵C. Jia, B. Moritz, C.-C. Chen, B. S. Shastry, and T. Devereaux: *Fidelity study of the superconducting phase diagram in the two-dimensional single-band Hubbard model*, “Physical Review B” vol. 84, no. 12, 125113 (2011) (cited on page 4).

- ²⁶Z. Jiang, K. J. Sung, K. Kechedzhi, V. N. Smelyanskiy, and S. Boixo: *Quantum algorithms to simulate many-body physics of correlated fermions*, "Physical Review Applied" vol. 9, no. 4, 044036 (2018) (cited on page 4).
- ²⁷M. Troyer and U.-J. Wiese: *Computational complexity and fundamental limitations to fermionic quantum Monte Carlo simulations*, "Physical Review Letters" vol. 94, no. 17, 170201 (2005) (cited on page 4).
- ²⁸J. Zaanen, S. Chakravarty, T. Senthil, P. Anderson, P. Lee, J. Schmalian, M. Imada, D. Pines, M. Randeria, C. Varma, et al.: *Towards a complete theory of high T_c* , "Nature Physics" vol. 2, no. 3, 138–143 (2006) (cited on page 4).
- ²⁹D. Wollman, D. J. Van Harlingen, J. Giapintzakis, and D. Ginsberg: *Evidence for $d_x^2 - y^2$ Pairing from the Magnetic Field Modulation of $YBa_2Cu_3O_{7-Pb}$ Josephson Junctions*, "Physical Review Letters" vol. 74, no. 5, 797 (1995) (cited on pages 4, 5, 63).
- ³⁰A. A. Golubov, M. Y. Kupriyanov, and E. Il'ichev: *The current-phase relation in Josephson junctions*, "Reviews of modern physics" vol. 76, no. 2, 411 (2004) (cited on pages 4, 79, 80, 83, 85).
- ³¹C. Gough, M. Colclough, E. Forgan, R. Jordan, M. Keene, C. Muirhead, A. Rae, N. Thomas, J. Abell, and S. Sutton: *Flux quantization in a high- T_c superconductor*, "Nature" vol. 326, no. 6116, 855–855 (1987) (cited on pages 4, 62).
- ³²D. Wollman, D. J. Van Harlingen, W. Lee, D. Ginsberg, and A. J. Leggett: *Experimental determination of the superconducting pairing state in YBCO from the phase coherence of YBCO-Pb dc SQUIDs*, "Physical Review Letters" vol. 71, no. 13, 2134 (1993) (cited on pages 5, 63).
- ³³P. W. Anderson: *Resonating valence bonds: A new kind of insulator?*, "Materials Research Bulletin" vol. 8, no. 2, 153–160 (1973) (cited on page 5).
- ³⁴G. Kotliar and J. Liu: *Superexchange mechanism and d -wave superconductivity*, "Physical Review B" vol. 38, no. 7, 5142 (1988) (cited on page 5).
- ³⁵S. Sachdev: *Quantum criticality: competing ground states in low dimensions*, "Science" vol. 288, no. 5465, 475–480 (2000) (cited on page 5).
- ³⁶S. Sachdev: *Quantum phase transitions*, "Handbook of Magnetism and Advanced Magnetic Materials" (2007) (cited on page 5).
- ³⁷J. Tranquada, B. Sternlieb, J. Axe, Y. Nakamura, and S. Uchida: *Evidence for stripe correlations of spins and holes in copper oxide superconductors*, "Nature" vol. 375, no. 6532, 561–563 (1995) (cited on page 5).
- ³⁸C. de La Cruz, Q. Huang, J. Lynn, J. Li, W. Ratcliff II, J. L. Zarestky, H. Mook, G. Chen, J. Luo, N. Wang, et al.: *Magnetic order close to superconductivity in the iron-based layered $LaO_{1-x}F_xFeAs$ systems*, "Nature" vol. 453, no. 7197, 899–902 (2008) (cited on page 5).

- ³⁹S. Sachdev: *Condensed matter and AdS/CFT*, in *From gravity to thermal gauge theories: the AdS/CFT correspondence*, Springer 2011, pp. 273–311 (cited on page 5).
- ⁴⁰S. Sachdev: *What can gauge-gravity duality teach us about condensed matter physics?*, “Annu. Rev. Condens. Matter Phys.” vol. 3, no. 1, 9–33 (2012) (cited on page 5).
- ⁴¹G. Carleo and M. Troyer: *Solving the quantum many-body problem with artificial neural networks*, “Science” vol. 355, no. 6325, 602–606 (2017) (cited on page 5).
- ⁴²R. P. Feynman: *Simulating physics with computers*, “International journal of theoretical physics” vol. 21, no. 6, 467–488 (1982) (cited on page 5).
- ⁴³D. Jaksch, C. Bruder, J. I. Cirac, C. W. Gardiner, and P. Zoller: *Cold bosonic atoms in optical lattices*, “Physical Review Letters” vol. 81, no. 15, 3108 (1998) (cited on page 5).
- ⁴⁴I. Bloch, J. Dalibard, and W. Zwerger: *Many-body physics with ultracold gases*, “Reviews of modern physics” vol. 80, no. 3, 885 (2008) (cited on pages 5, 16).
- ⁴⁵M. Greiner, O. Mandel, T. Esslinger, T. W. Hänsch, and I. Bloch: *Quantum phase transition from a superfluid to a Mott insulator in a gas of ultracold atoms*, “Nature” vol. 415, no. 6867, 39 (2002) (cited on page 5).
- ⁴⁶R. Jördens, N. Strohmaier, K. Günter, H. Moritz, and T. Esslinger: *A Mott insulator of fermionic atoms in an optical lattice*, “Nature” vol. 455, no. 7210, 204–207 (2008) (cited on page 5).
- ⁴⁷A. Mazurenko, C. S. Chiu, G. Ji, M. F. Parsons, M. Kanász-Nagy, R. Schmidt, F. Grusdt, E. Demler, D. Greif, and M. Greiner: *A cold-atom Fermi–Hubbard antiferromagnet*, “Nature” vol. 545, no. 7655, 462 (2017) (cited on pages 5, 69).
- ⁴⁸C. Chin, R. Grimm, P. Julienne, and E. Tiesinga: *Feshbach resonances in ultracold gases*, “Reviews of Modern Physics” vol. 82, no. 2, 1225 (2010) (cited on page 5).
- ⁴⁹W. Zwerger: *The BCS-BEC crossover and the unitary Fermi gas*, Vol. 836, Springer Science & Business Media 2011 (cited on pages 5, 15).
- ⁵⁰C. Regal, M. Greiner, and D. S. Jin: *Observation of resonance condensation of fermionic atom pairs*, “Physical Review Letters” vol. 92, no. 4, 040403 (2004) (cited on page 5).
- ⁵¹S. Jochim, M. Bartenstein, A. Altmeyer, G. Hendl, S. Riedl, C. Chin, J. H. Denschlag, and R. Grimm: *Bose-Einstein condensation of molecules*, “Science” vol. 302, no. 5653, 2101–2103 (2003) (cited on page 5).
- ⁵²M. Zwierlein, C. Stan, C. Schunck, S. Raupach, A. Kerman, and W. Ketterle: *Condensation of pairs of fermionic atoms near a Feshbach resonance*, “Physical Review Letters” vol. 92, no. 12, 120403 (2004) (cited on page 5).

- ⁵³M. W. Zwierlein, C. A. Stan, C. H. Schunck, S. M. Raupach, S. Gupta, Z. Hadzibabic, and W. Ketterle: *Observation of Bose-Einstein condensation of molecules*, “Physical Review Letters” vol. 91, no. 25, 250401 (2003) (cited on page 5).
- ⁵⁴M. Greiner, C. A. Regal, and D. S. Jin: *Emergence of a molecular Bose-Einstein condensate from a Fermi gas*, “Nature” vol. 426, no. 6966, 537 (2003) (cited on page 5).
- ⁵⁵M. W. Zwierlein, J. R. Abo-Shaeer, A. Schirotzek, C. H. Schunck, and W. Ketterle: *Vortices and superfluidity in a strongly interacting Fermi gas*, “Nature” vol. 435, no. 7045, 1047 (2005) (cited on page 5).
- ⁵⁶J. Kinast, S. Hemmer, M. Gehm, A. Turlapov, and J. Thomas: *Evidence for superfluidity in a resonantly interacting Fermi gas*, “Physical Review Letters” vol. 92, no. 15, 150402 (2004) (cited on page 5).
- ⁵⁷D. Miller, J. Chin, C. Stan, Y. Liu, W. Setiawan, C. Sanner, and W. Ketterle: *Critical velocity for superfluid flow across the BEC-BCS crossover*, “Physical Review Letters” vol. 99, no. 7, 070402 (2007) (cited on pages 5, 97).
- ⁵⁸M. J. Ku, A. T. Sommer, L. W. Cheuk, and M. W. Zwierlein: *Revealing the superfluid lambda transition in the universal thermodynamics of a unitary Fermi gas*, “Science” vol. 335, no. 6068, 563–567 (2012) (cited on pages 5, 99).
- ⁵⁹W. Weimer, K. Morgener, V. P. Singh, J. Siegl, K. Hueck, N. Luick, L. Mathey, and H. Moritz: *Critical velocity in the BEC-BCS crossover*, “Physical Review Letters” vol. 114, no. 9, 095301 (2015) (cited on pages 5, 97).
- ⁶⁰Y. Uemura, L. Le, G. Luke, B. Sternlieb, W. Wu, J. Brewer, T. Rise-man, C. Seaman, M. Maple, M. Ishikawa, et al.: *Basic similarities among cuprate, bismuthate, organic, Chevrel-phase, and heavy-fermion superconductors shown by penetration-depth measurements*, “Physical Review Letters” vol. 66, no. 20, 2665 (1991) (cited on page 6).
- ⁶¹Y. Uemura: *Condensation, excitation, pairing, and superfluid density in high-Tc superconductors: the magnetic resonance mode as a roton analogue and a possible spin-mediated pairing*, “Journal of Physics: Condensed Matter” vol. 16, no. 40, S4515 (2004) (cited on page 6).
- ⁶²D. Petrov, M. Baranov, and G. Shlyapnikov: *Superfluid transition in quasi-two-dimensional Fermi gases*, “Physical Review A” vol. 67, no. 3, 031601 (2003) (cited on pages 6, 19, 21, 24, 69, 90).
- ⁶³M. Ries, A. Wenz, G. Zürn, L. Bayha, I. Boettcher, D. Kedar, P. Murthy, M. Neidig, T. Lompe, and S. Jochim: *Observation of pair condensation in the quasi-2D BEC-BCS crossover*, “Physical Review Letters” vol. 114, no. 23, 230401 (2015) (cited on pages 6, 38, 45, 48, 52, 69, 89).
- ⁶⁴M. Randeria, J.-M. Duan, and L.-Y. Shieh: *Bound states, Cooper pairing, and Bose condensation in two dimensions*, “Physical Review Letters” vol. 62, no. 9, 981 (1989) (cited on page 6).

- ⁶⁵Q. Chen, J. Stajic, S. Tan, and K. Levin: *BCS–BEC crossover: From high temperature superconductors to ultracold superfluids*, “Physics Reports” vol. 412, no. 1, 1–88 (2005) (cited on page 6).
- ⁶⁶R. Friedberg and T. Lee: *Boson-fermion model of superconductivity*, “Physics Letters A” vol. 138, no. 8, 423–427 (1989) (cited on page 6).
- ⁶⁷T. K. Worthington, W. Gallagher, and T. Dinger: *Anisotropic nature of high-temperature superconductivity in single-crystal $Y_{1-x}Ba_2Cu_3O_{7-x}$* , “Physical Review Letters” vol. 59, no. 10, 1160 (1987) (cited on page 6).
- ⁶⁸P. Chaudhari, R. Collins, P. Freitas, R. Gambino, J. Kirtley, R. Koch, R. Laibowitz, F. LeGoues, T. McGuire, T. Penney, et al.: *Properties of epitaxial films of $YBa_2Cu_3O_{7-\delta}$* , “Physical Review B” vol. 36, no. 16, 8903 (1987) (cited on page 6).
- ⁶⁹P. Nozieres and S. Schmitt-Rink: *Bose condensation in an attractive fermion gas: From weak to strong coupling superconductivity*, “Journal of Low Temperature Physics” vol. 59, no. 3-4, 195–211 (1985) (cited on page 6).
- ⁷⁰Y. Uemura: *Energy scales of high-Tc cuprates, doped fullerenes, and other exotic superconductors*, in Proc. Int. Symp./Workshop on High-Tc Superconductivity and the C, Vol. 60 (1995), pp. 113–42 (cited on page 6).
- ⁷¹A. Damascelli, Z. Hussain, and Z.-X. Shen: *Angle-resolved photoemission studies of the cuprate superconductors*, “Reviews of modern physics” vol. 75, no. 2, 473 (2003) (cited on page 6).
- ⁷²J. Levinsen and M. M. Parish: *Strongly interacting two-dimensional Fermi gases*, in *Annual review of cold atoms and molecules*, World Scientific 2015, pp. 1–75 (cited on pages 6, 15, 16, 19, 21, 69).
- ⁷³K. Martiyanov, V. Makhalov, and A. Turlapov: *Observation of a two-dimensional Fermi gas of atoms*, “Physical Review Letters” vol. 105, no. 3, 030404 (2010) (cited on page 6).
- ⁷⁴V. Makhalov, K. Martiyanov, and A. Turlapov: *Ground-state pressure of quasi-2D Fermi and Bose gases*, “Physical Review Letters” vol. 112, no. 4, 045301 (2014) (cited on pages 6, 17, 69).
- ⁷⁵I. Boettcher, L. Bayha, D. Kedar, P. Murthy, M. Neidig, M. Ries, A. Wenz, G. Zuern, S. Jochim, and T. Enss: *Equation of state of ultracold fermions in the 2D BEC-BCS crossover region*, “Physical Review Letters” vol. 116, no. 4, 045303 (2016) (cited on pages 6, 15, 17, 91).
- ⁷⁶K. Fenech, P. Dyke, T. Pepler, M. Lingham, S. Hoinka, H. Hu, and C. Vale: *Thermodynamics of an attractive 2D Fermi gas*, “Physical Review Letters” vol. 116, no. 4, 045302 (2016) (cited on pages 6, 69).
- ⁷⁷P. A. Murthy, M. Neidig, R. Klemt, L. Bayha, I. Boettcher, T. Enss, M. Holten, G. Zürn, P. M. Preiss, and S. Jochim: *High-temperature pairing in a strongly interacting two-dimensional Fermi gas*, “Science” vol. 359, no. 6374, 452–455 (2018) (cited on page 6).

- ⁷⁸P. Murthy, I. Boettcher, L. Bayha, M. Holzmann, D. Kedar, M. Neidig, M. Ries, A. Wenz, G. Zürn, and S. Jochim: *Observation of the Berezinskii-Kosterlitz-Thouless phase transition in an ultracold Fermi gas*, “Physical Review Letters” vol. 115, no. 1, 010401 (2015) (cited on pages 7, 19, 34, 37, 41, 88, 90).
- ⁷⁹K. Hueck: *A homogeneous, two-dimensional fermi gas. Measurements in Position- and Momentum-Space*, PhD thesis, Universität Hamburg 2017 (cited on pages 10, 26, 27, 31, 34, 35).
- ⁸⁰A. Turlapov and M. Y. Kagan: *Fermi-to-Bose crossover in a trapped quasi-2D gas of fermionic atoms*, “J. Phys. Condens. Matter” vol. 29, no. 38, 383004 (2017) (cited on pages 15, 17, 33, 76).
- ⁸¹Z. Hadzibabic and J. Dalibard: *Two-dimensional Bose fluids: An atomic physics perspective*, “RIV NUOVO CIMENTO” vol. 34, no. 6 (2011) (cited on pages 15, 16, 18, 19, 33, 87, 90, 92).
- ⁸²K. H. Morgener: *Microscopy of 2D Fermi Gases Exploring excitations and thermodynamics*, PhD thesis, Universität Hamburg 2014 (cited on pages 15, 19, 21, 22, 24).
- ⁸³D. Petrov and G. Shlyapnikov: *Interatomic collisions in a tightly confined Bose gas*, “Physical Review Letters” vol. 64, no. 1, 012706 (2001) (cited on pages 15, 17, 73).
- ⁸⁴D. Petrov, C. Salomon, and G. V. Shlyapnikov: *Weakly bound dimers of fermionic atoms*, “Physical Review Letters” vol. 93, no. 9, 090404 (2004) (cited on page 16).
- ⁸⁵S. K. Baur, B. Fröhlich, M. Feld, E. Vogt, D. Pertot, M. Koschorreck, and M. Köhl: *Radio-frequency spectra of Feshbach molecules in quasi-two-dimensional geometries*, “Physical Review A” vol. 85, no. 6, 061604 (2012) (cited on page 16).
- ⁸⁶H. Hu, B. C. Mulkerin, U. Toniolo, L. He, and X.-J. Liu: *Reduced Quantum Anomaly in a Quasi-Two-Dimensional Fermi Superfluid: Significance of the Confinement-Induced Effective Range of Interactions*, “Physical Review Letters” vol. 122, no. 7, 070401 (2019) (cited on page 17).
- ⁸⁷F. Wu, J. Hu, L. He, X.-J. Liu, and H. Hu: *Effective theory for ultracold strongly interacting fermionic atoms in two dimensions*, “arXiv preprint arXiv:1906.08578” (2019) (cited on page 17).
- ⁸⁸B. C. Mulkerin, H. Hu, and X.-J. Liu: *Role of the confinement-induced effective range on the thermodynamics of a strongly correlated Fermi gas in two dimensions*, “arXiv preprint arXiv:1909.03578” (2019) (cited on page 17).
- ⁸⁹D. R. Nelson and J. Kosterlitz: *Universal jump in the superfluid density of two-dimensional superfluids*, “Physical Review Letters” vol. 39, no. 19, 1201 (1977) (cited on pages 18, 87).
- ⁹⁰N. Prokof'ev, O. Ruebenacker, and B. Svistunov: *Critical point of a weakly interacting two-dimensional Bose gas*, “Physical Review Letters” vol. 87, no. 27, 270402 (2001) (cited on pages 19, 83).

- ⁹¹K. Miyake: *Fermi liquid theory of dilute submonolayer ^3He on thin ^4He II film: dimer bound state and Cooper pairs*, “Progress of theoretical physics” vol. 69, no. 6, 1794–1797 (1983) (cited on page 19).
- ⁹²B. C. Mulkerin, L. He, P. Dyke, C. J. Vale, X.-J. Liu, and H. Hu: *Superfluid density and critical velocity near the Berezinskii-Kosterlitz-Thouless transition in a two-dimensional strongly interacting Fermi gas*, “Physical Review Letters” vol. 96, no. 5, 053608 (2017) (cited on page 19).
- ⁹³W. Weimer: *Probing superfluid properties in strongly correlated Fermi gases with high spatial resolution*, PhD thesis, Universität Hamburg 2014 (cited on pages 21, 23, 26, 27, 29).
- ⁹⁴K. Hueck, A. Mazurenko, N. Luick, T. Lompe, and H. Moritz: *Note: Suppression of kHz-frequency switching noise in digital micro-mirror devices*, “Review Sci. Instrum.” vol. 88, no. 1, 016103 (2017) (cited on pages 21, 48).
- ⁹⁵J. Siegl: *Probing coherence properties of strongly interacting Bose gases*, PhD thesis, Universität Hamburg 2018 (cited on pages 21, 25).
- ⁹⁶K. Hueck, N. Luick, L. Sobirey, J. Siegl, T. Lompe, and H. Moritz: *Two-dimensional homogeneous Fermi gases*, “Physical Review Letters” vol. 120, no. 6, 060402 (2018) (cited on pages 21, 32–34, 38, 39, 69, 72, 73).
- ⁹⁷N. Luick, L. Sobirey, M. Bohlen, V. P. Singh, L. Mathey, T. Lompe, and H. Moritz: *An ideal Josephson junction in an ultracold two-dimensional Fermi gas*, “arXiv preprint arXiv:1908.09776” (2019) (cited on page 21).
- ⁹⁸H. J. Metcalf and P. Van der Straten: *Laser cooling and trapping of neutral atoms*, “The Optics Encyclopedia: Basic Foundations and Practical Applications” (2007) (cited on page 23).
- ⁹⁹M. E. Gehm: *Properties of ^6Li* , “Jetlab,” (2003) (cited on page 23).
- ¹⁰⁰M. G. Ries: *A two-dimensional Fermi gas in the BEC-BCS crossover*, PhD thesis, 2015 (cited on pages 23, 37).
- ¹⁰¹F. G. Huber: *Site-resolved imaging with the Fermi gas microscope*, PhD thesis, 2014 (cited on page 23).
- ¹⁰²D. Mitra: *Exploring attractively interacting fermions in 2D using a quantum gas microscope*, PhD thesis, Princeton University 2018 (cited on page 23).
- ¹⁰³B. Zimmermann: *Microscopy of ultra-cold fermionic lithium*, PhD thesis, ETH Zurich 2010 (cited on page 23).
- ¹⁰⁴F. Wittkötter: *Realizing a Resonator Cooling Scheme for Ultra-cold Fermi Gases*, Diploma thesis, Universität Hamburg 2011 (cited on page 23).
- ¹⁰⁵S. Eckel, D. S. Barker, J. A. Fedchak, N. N. Klimov, E. Norrgard, J. Scherschligt, C. Makrides, and E. Tiesinga: *Challenges to miniaturizing cold atom technology for deployable vacuum metrology*, “Metrologia” vol. 55, no. 5, S182 (2018) (cited on page 25).
- ¹⁰⁶T. Hartmann: *An experiment apparatus for the production of ultracold bosonic dipolar ground state $^{23}\text{Na}^{39}\text{K}$ molecules and Feshbach spectroscopy in a cold mixture of ^{23}Na and ^{39}K* , PhD thesis, Universität Hannover 2019 (cited on page 25).

- ¹⁰⁷T. Kessler, C. Hagemann, C. Grebing, T. Legero, U. Sterr, F. Riehle, M. Martin, L. Chen, and J. Ye: *A sub-40-mHz-linewidth laser based on a silicon single-crystal optical cavity*, “Nature Photonics” vol. 6, no. 10, 687 (2012) (cited on page 26).
- ¹⁰⁸E. D. Black: *An introduction to Pound–Drever–Hall laser frequency stabilization*, “American journal of physics” vol. 69, no. 1, 79–87 (2001) (cited on page 28).
- ¹⁰⁹K. Hueck: *Erzeugung und Untersuchung von ultrakalten, zweidimensionalen Fermi-Gasen*, Master’s thesis, Universität Hamburg 2013 (cited on page 31).
- ¹¹⁰P. Dyke, K. Fenech, T. Peppler, M. G. Lingham, S. Hoinka, W. Zhang, S.-G. Peng, B. Mulkerin, H. Hu, X.-J. Liu, and C. J. Vale: *Criteria for two-dimensional kinematics in an interacting Fermi gas*, “Physical Review A” vol. 93, 011603 (2016) (cited on pages 32, 33, 38).
- ¹¹¹J. Kestner and L.-M. Duan: *Conditions of low dimensionality for strongly interacting atoms under a transverse trap*, “Physical Review A” vol. 74, no. 5, 053606 (2006) (cited on page 33).
- ¹¹²A. L. Gaunt, T. F. Schmidutz, I. Gotlibovych, R. P. Smith, and Z. Hadzibabic, “Physical Review Letters” vol. 110, 200406 (2013) (cited on pages 34, 45).
- ¹¹³A. L. Navon N. Gaunt, R. P. Smith, and Z. Hadzibabic, “Science” vol. 347, 167 (2015) (cited on pages 34, 45).
- ¹¹⁴B. Mukherjee, Z. Yan, P. B. Patel, Z. Hadzibabic, T. Yefsah, J. Struck, and M. W. Zwierlein: *Homogeneous Atomic Fermi Gases*, “Physical Review Letters” vol. 118, 123401 (2017) (cited on pages 34, 45, 46, 52).
- ¹¹⁵K. Hueck, A. Mazurenko, N. Luick, T. Lompe, and H. Moritz: *Note: Suppression of kHz-frequency switching noise in digital micro-mirror devices*, “Review of Scientific Instruments” vol. 88, no. 1, 016103 (2017) (cited on page 35).
- ¹¹⁶K. Hueck, N. Luick, L. Sobirey, T. Lompe, H. Moritz, L. Clark, and C. Chin: *Calibrating High Intensity Absorption Imaging of Ultracold Atoms*, “Opt. Exp.” vol. 25 (2017) (cited on pages 36, 37, 48).
- ¹¹⁷J. W. Goodman: *Introduction to Fourier optics*, Roberts and Company Publishers 2005 (cited on page 37).
- ¹¹⁸K. Martiyanov, V. Makhlov, and A. Turlapov: *Observation of a Two-Dimensional Fermi Gas of Atoms*, “Physical Review Letters” vol. 105, 030404 (2010) (cited on page 45).
- ¹¹⁹P. Dyke, E. D. Kuhnle, S. Whitlock, H. Hu, M. Mark, S. Hoinka, M. Lingham, P. Hannaford, and C. J. Vale, “Physical Review Letters” vol. 106, 105304 (2011) (cited on page 45).
- ¹²⁰W. Ong, C. Cheng, I. Arakelyan, and J. E. Thomas, “Physical Review Letters” vol. 114, 110403 (2015) (cited on pages 45, 69).

- ¹²¹D. Mitra, P. T. Brown, P. Schauß, S. S. Kondov, and W. S. Bakr: *Phase Separation and Pair Condensation in a Spin-Imbalanced 2D Fermi Gas*, “Physical Review Letters” vol. 117, 093601 (2016) (cited on pages 45, 69).
- ¹²²B. Fröhlich, M. Feld, E. Vogt, M. Koschorreck, W. Zwerger, and M. Köhl, “Physical Review Letters” vol. 106, 105301 (2011) (cited on pages 45, 69).
- ¹²³M. Feld, B. Fröhlich, E. Vogt, M. Koschorreck, and M. Köhl, “Nature” vol. 480, 75 (2011) (cited on page 45).
- ¹²⁴A. T. Sommer, L. W. Cheuk, M. J. H. Ku, W. S. Bakr, and M. W. Zwierlein, “Physical Review Letters” vol. 108, 045302 (2012) (cited on pages 45, 69).
- ¹²⁵C. Cheng, J. Kangara, I. Arakelyan, and J. E. Thomas, “Physical Review A” vol. 94, 031606(R) (2016) (cited on page 45).
- ¹²⁶B. Fröhlich, M. Feld, E. Vogt, M. Koschorreck, M. Köhl, C. Berthod, and T. Giamarchi, “Physical Review Letters” vol. 109, 130403 (2012) (cited on page 45).
- ¹²⁷M. Koschorreck, D. Pertot, E. Vogt, B. Fröhlich, M. Feld, and M. Köhl, “Nature” vol. 485, 619 (2012) (cited on page 45).
- ¹²⁸Y. Zhang, W. Ong, I. Arakelyan, and J. E. Thomas, “Physical Review Letters” vol. 108, 235302 (2012) (cited on page 45).
- ¹²⁹V. Makhalov, K. Martiyanov, and A. Turlapov: *Ground-State Pressure of Quasi-2D Fermi and Bose Gases*, “Physical Review Letters” vol. 112, 045301 (2014) (cited on page 45).
- ¹³⁰K. Fenech, P. Dyke, T. Pepler, M. Lingham, S. Hoinka, H. Hu, and C. Vale, “Physical Review Letters” vol. 116, 045302 (2016) (cited on page 45).
- ¹³¹I. Boettcher, L. Bayha, D. Kedar, P. A. Murthy, M. Neidig, M. G. Ries, A. N. Wenz, G. Zürn, S. Jochim, and T. Enss: *Equation of State of Ultracold Fermions in the 2D BEC-BCS Crossover Region*, “Physical Review Letters” vol. 116, 045303 (2016) (cited on pages 45, 48).
- ¹³²P. A. Murthy, I. Boettcher, L. Bayha, M. Holzmann, D. Kedar, M. Neidig, M. G. Ries, A. N. Wenz, G. Zürn, and S. Jochim: *Observation of the Berezinskii-Kosterlitz-Thouless Phase Transition in an Ultracold Fermi Gas*, “Physical Review Letters” vol. 115, 010401 (2015) (cited on page 45).
- ¹³³P. Fulde and R. A. Ferrell: *Superconductivity in a Strong Spin-Exchange Field*, “Phys. Rev.” vol. 135, A550–A563 (1964) (cited on page 45).
- ¹³⁴A. Larkin and Y. Ovchinnikov: *Inhomogeneous State of Superconductors*, “Sov. Phys. JETP” vol. 20, 762 (1965) (cited on page 45).
- ¹³⁵G. J. Conduit, P. H. Conlon, and B. D. Simons: *Superfluidity at the BEC-BCS crossover in two-dimensional Fermi gases with population and mass imbalance*, “Physical Review A” vol. 77, 053617 (2008) (cited on page 45).

- ¹³⁶U. Toniolo, B. Mulkerin, X.-J. Liu, and H. Hu: *Larkin-Ovchinnikov superfluidity in a two-dimensional imbalanced atomic Fermi gas*, “[Physical Review A](#)” vol. 95, 013603 (2017) (cited on page 45).
- ¹³⁷T. F. Schmidutz, I. Gotlibovych, A. L. Gaunt, R. P. Smith, N. Navon, and Z. Hadzibabic, “[Physical Review Letters](#)” vol. 112, 040403 (2014) (cited on page 45).
- ¹³⁸L. Corman, L. Chomaz, T. Bienaimé, R. Desbuquois, C. Weitenberg, S. Nascimbène, J. Dalibard, and J. Beugnon, “[Physical Review Letters](#)” vol. 113, 135302 (2014) (cited on page 45).
- ¹³⁹L. Chomaz, L. Corman, T. Bienaimé, R. Desbuquois, C. Weitenberg, S. Nascimbène, J. Beugnon, and J. Dalibard, “[Nat. Commun.](#)” vol. 6, 6162 (2015) (cited on page 45).
- ¹⁴⁰W. Weimer, K. Morgener, V. P. Singh, J. Siegl, K. Hueck, N. Luick, L. Mathey, and H. Moritz: *Critical Velocity in the BEC-BCS Crossover*, “[Physical Review Letters](#)” vol. 114, 095301 (2015) (cited on pages 46, 101).
- ¹⁴¹J. H. McLeod: *The Axicon: A New Type of Optical Element*, “[J. Opt. Soc. Am.](#)” vol. 44, no. 8, 592–597 (1954) (cited on page 46).
- ¹⁴²I. Manek, Y. Ovchinnikov, and R. Grimm: *Generation of a hollow laser beam for atom trapping using an axicon*, “[Opt. Commun.](#)” vol. 147, no. 1–3, 67–70 (1998) (cited on page 46).
- ¹⁴³D. S. Petrov, M. Holzmann, and G. V. Shlyapnikov: *Bose-Einstein Condensation in Quasi-2D Trapped Gases*, “[Physical Review Letters](#)” vol. 84, 2551–2555 (2000) (cited on page 46).
- ¹⁴⁴Z. Hadzibabic, P. Krüger, M. Cheneau, B. Battelier, and J. Dalibard, “[Nature](#)” vol. 441, 1118 (2006) (cited on pages 46, 87).
- ¹⁴⁵G. Reinaudi, T. Lahaye, Z. Wang, and D. Guéry-Odelin, “[Opt. Lett.](#)” vol. 32, 3143 (2007) (cited on pages 48, 100, 101, 103).
- ¹⁴⁶M. Bauer, M. M. Parish, and T. Enss: *Universal Equation of State and Pseudogap in the Two-Dimensional Fermi Gas*, “[Physical Review Letters](#)” vol. 112, 135302 (2014) (cited on page 48).
- ¹⁴⁷C.-L. Hung, X. Zhang, N. Gemelke, and C. Chin: *Observation of scale invariance and universality in two-dimensional Bose gases*, “[Nature](#)” vol. 470, no. 7333, 236–239 (2011) (cited on pages 48, 99, 100, 106).
- ¹⁴⁸S. I., C. Buggle, D. S. Petrov, K. Dieckmann, M. Zielonkowski, M. Kemmann, T. G. Tiecke, W. von Klitzing, G. V. Shlyapnikov, and J. T. M. Walraven, “[Physical Review Letters](#)” vol. 89, 270404 (2002) (cited on page 48).
- ¹⁴⁹S. Tung, G. Lamporesi, D. Lobser, L. Xia, and E. A. Cornell, “[Physical Review Letters](#)” vol. 105, 230408 (2010) (cited on page 48).
- ¹⁵⁰P. A. Murthy, D. Kedar, T. Lompe, M. Neidig, M. G. Ries, A. N. Wenz, G. Zürn, and S. Jochim: *Matter-wave Fourier optics with a strongly interacting two-dimensional Fermi gas*, “[Physical Review A](#)” vol. 90, 043611 (2014) (cited on page 48).

- ¹⁵¹G. Zürn, T. Lompe, A. N. Wenz, S. Jochim, P. S. Julienne, and J. M. Hutson: *Precise Characterization of ⁶Li Feshbach Resonances Using Trap-Sideband-Resolved RF Spectroscopy of Weakly Bound Molecules*, “*Physical Review Letters*” vol. 110, 135301 (2013) (cited on page 52).
- ¹⁵²C. A. Regal, M. Greiner, S. Giorgini, M. Holland, and D. S. Jin: *Momentum Distribution of a Fermi Gas of Atoms in the BCS-BEC Crossover*, “*Physical Review Letters*” vol. 95, 250404 (2005) (cited on page 52).
- ¹⁵³P. Krüger, Z. Hadzibabic, and J. Dalibard, “*Physical Review Letters*” vol. 99, 040402 (2007) (cited on page 52).
- ¹⁵⁴P. Cladé, C. Ryu, A. Ramanathan, K. Helmerson, and W. D. Phillips, “*Physical Review Letters*” vol. 102, 170401 (2009) (cited on page 52).
- ¹⁵⁵M. Weinberg, O. Jürgensen, C. Ölschläger, D.-S. Lühmann, K. Senegstock, and J. Simonet: *Symmetry-broken momentum distributions induced by matter-wave diffraction during time-of-flight expansion of ultracold atoms*, “*Physical Review A*” vol. 93, no. 3, 033625 (2016) (cited on page 52).
- ¹⁵⁶S. Murmann, F. Deuretzbacher, G. Zürn, J. Bjerlin, S. M. Reimann, L. Santos, T. Lompe, and S. Jochim: *Antiferromagnetic Heisenberg spin chain of a few cold atoms in a one-dimensional trap*, “*Physical Review Letters*” vol. 115, no. 21, 215301 (2015) (cited on page 52).
- ¹⁵⁷P. Bloom: *Two-dimensional Fermi gas*, “*Physical Review B*” vol. 12, 125–129 (1975) (cited on page 52).
- ¹⁵⁸A. M. Fischer and M. M. Parish: *Quasi-two-dimensional Fermi gases at finite temperatures*, “*Physical Review B*” vol. 90, 214503 (2014) (cited on page 52).
- ¹⁵⁹M. Greiner, C. A. Regal, J. T. Stewart, and D. S. Jin, “*Physical Review Letters*” vol. 94, 110401 (2005) (cited on page 53).
- ¹⁶⁰B. D. Josephson: *Possible new effects in superconductive tunnelling*, “*Physics Letters*” vol. 1, no. 7, 251–253 (1962) (cited on page 59).
- ¹⁶¹P. W. Anderson and J. M. Rowell, “*Physical Review Letters*” vol. 10, 230 (1963) (cited on page 59).
- ¹⁶²F. Liu, J. Tong, J. Mao, R. Bohn, J. Messina, L. Badger, and D. Leaf: *National Institute of Standards and Technology Special Publication*, 2011 (cited on page 61).
- ¹⁶³C. A. Hamilton: *Josephson voltage standards*, “*Review of scientific instruments*” vol. 71, no. 10, 3611–3623 (2000) (cited on page 61).
- ¹⁶⁴C. A. Hamilton, R. L. Kautz, R. L. Steiner, and F. L. Lloyd: *A practical Josephson voltage standard at 1 V*, “*IEEE electron device letters*” vol. 6, no. 12, 623–625 (1985) (cited on page 61).
- ¹⁶⁵I. des Poids et Mesures: *The International System of Units (SI)*, 9th ed. Vol. 9, 2019 (cited on page 61).
- ¹⁶⁶B. Field, T. Finnegan, and J. Toots: *Volt maintenance at NBS via 2e/h: A new definition of the NBS volt*, “*Metrologia*” vol. 9, no. 4, 155 (1973) (cited on page 61).

- ¹⁶⁷J. Clarke and A. I. Braginski: *The SQUID handbook: Applications of SQUIDs and SQUID systems*, John Wiley & Sons 2006 (cited on page 62).
- ¹⁶⁸R. Hari and R. Salmelin: *Magnetoencephalography: from SQUIDs to neuroscience: Neuroimage 20th anniversary special edition*, "Neuroimage" vol. 61, no. 2, 386–396 (2012) (cited on page 62).
- ¹⁶⁹C. F. Everitt, D. DeBra, B. Parkinson, J. Turneare, J. Conklin, M. Heifetz, G. Keiser, A. Silbergleit, T. Holmes, J. Kolodziejczak, et al.: *Gravity probe B: final results of a space experiment to test general relativity*, "Physical Review Letters" vol. 106, no. 22, 221101 (2011) (cited on page 62).
- ¹⁷⁰D. J. Van Harlingen: *Phase-sensitive tests of the symmetry of the pairing state in the high-temperature superconductors—evidence for $d_{x^2-y^2}$ symmetry*, "Rev. Mod. Phys." vol. 67, no. 2, 515 (1995) (cited on page 62).
- ¹⁷¹H. Ding, M. Norman, J. Campuzano, M. Randeria, A. Bellman, T. Yokoya, T. Takahashi, T. Mochiku, and K. Kadowaki: *Angle-resolved photoemission spectroscopy study of the superconducting gap anisotropy in $\text{Bi}_2\text{Sr}_2\text{CaCu}_2\text{O}_{8+x}$* , "Physical Review B" vol. 54, no. 14, R9678 (1996) (cited on page 63).
- ¹⁷²P. Krantz, M. Kjaergaard, F. Yan, T. P. Orlando, S. Gustavsson, and W. D. Oliver: *A quantum engineer's guide to superconducting qubits*, "Applied Physics Reviews" vol. 6, no. 2, 021318 (2019) (cited on page 64).
- ¹⁷³J. Koch, M. Y. Terri, J. Gambetta, A. A. Houck, D. Schuster, J. Majer, A. Blais, M. H. Devoret, S. M. Girvin, and R. J. Schoelkopf: *Charge-insensitive qubit design derived from the Cooper pair box*, "Physical Review A" vol. 76, no. 4, 042319 (2007) (cited on page 64).
- ¹⁷⁴F. Arute, K. Arya, R. Babbush, D. Bacon, J. C. Bardin, R. Barends, R. Biswas, S. Boixo, F. G. Brandao, D. A. Buell, et al.: *Quantum supremacy using a programmable superconducting processor*, "Nature" vol. 574, no. 7779, 505–510 (2019) (cited on page 64).
- ¹⁷⁵E. Hoskinson, Y. Sato, I. Hahn, and R. Packard: *Transition from phase slips to the Josephson effect in a superfluid ^4He weak link*, "Nature Physics" vol. 2, no. 1, 23–26 (2006) (cited on page 65).
- ¹⁷⁶R. Simmonds, A. Marchenkov, E. Hoskinson, J. Davis, and R. Packard: *Quantum interference of superfluid ^3He* , "Nature" vol. 412, no. 6842, 55–58 (2001) (cited on page 65).
- ¹⁷⁷J. Javanainen: *Oscillatory exchange of atoms between traps containing Bose condensates*, "Physical Review Letters" vol. 57, no. 25, 3164 (1986) (cited on page 66).
- ¹⁷⁸M. H. Anderson, J. R. Ensher, M. R. Matthews, C. E. Wieman, and E. A. Cornell: *Observation of Bose-Einstein condensation in a dilute atomic vapor*, "Science", 198–201 (1995) (cited on pages 66, 99).

- ¹⁷⁹K. B. Davis, M.-O. Mewes, M. R. Andrews, N. J. van Druten, D. S. Durfee, D. Kurn, and W. Ketterle: *Bose-Einstein condensation in a gas of sodium atoms*, "Physical Review Letters" vol. 75, no. 22, 3969 (1995) (cited on pages 66, 99).
- ¹⁸⁰R. Gati and M. Oberthaler: *A bosonic Josephson junction*, "Journal of Physics B: Atomic, Molecular and Optical Physics" vol. 40, no. 10, R61 (2007) (cited on page 66).
- ¹⁸¹F. Cataliotti, S. Burger, C. Fort, P. Maddaloni, F. Minardi, A. Trombettoni, A. Smerzi, and M. Inguscio: *Josephson junction arrays with Bose-Einstein condensates*, "Science" vol. 293, no. 5531, 843–846 (2001) (cited on page 66).
- ¹⁸²M. Albiez, R. Gati, J. Fölling, S. Hunsmann, M. Cristiani, and M. K. Oberthaler: *Direct observation of tunneling and nonlinear self-trapping in a single bosonic Josephson junction*, "Physical Review Letters" vol. 95, no. 1, 010402 (2005) (cited on page 66).
- ¹⁸³S. Levy, E. Lahoud, I. Shomroni, and J. Steinhauer: *The ac and dc Josephson effects in a Bose-Einstein condensate*, "Nature" vol. 449, no. 7162, 579 (2007) (cited on page 66).
- ¹⁸⁴T. Betz, S. Manz, R. Bücke, T. Berrada, C. Koller, G. Kazakov, I. E. Mazets, H.-P. Stimming, A. Perrin, T. Schumm, et al.: *Two-point phase correlations of a one-dimensional bosonic Josephson junction*, "Physical Review Letters" vol. 106, no. 2, 020407 (2011) (cited on page 66).
- ¹⁸⁵G. Spagnolli, G. Semeghini, L. Masi, G. Ferioli, A. Trenkwalder, S. Coop, M. Landini, L. Pezze, G. Modugno, M. Inguscio, et al.: *Crossing over from attractive to repulsive interactions in a tunneling bosonic Josephson junction*, "Physical Review Letters" vol. 118, no. 23, 230403 (2017) (cited on pages 66, 67).
- ¹⁸⁶C. Ryu, P. Blackburn, A. Blinova, and M. Boshier: *Experimental realization of Josephson junctions for an atom SQUID*, "Physical Review Letters" vol. 111, no. 20, 205301 (2013) (cited on page 66).
- ¹⁸⁷M. Andrews, C. Townsend, H.-J. Miesner, D. Durfee, D. Kurn, and W. Ketterle: *Observation of interference between two Bose condensates*, "Science" vol. 275, no. 5300, 637–641 (1997) (cited on page 66).
- ¹⁸⁸A. Smerzi, S. Fantoni, S. Giovanazzi, and S. Shenoy: *Quantum coherent atomic tunneling between two trapped Bose-Einstein condensates*, "Physical Review Letters" vol. 79, no. 25, 4950 (1997) (cited on page 66).
- ¹⁸⁹T. Anker, M. Albiez, R. Gati, S. Hunsmann, B. Eiermann, A. Trombettoni, and M. Oberthaler: *Nonlinear self-trapping of matter waves in periodic potentials*, "Physical Review Letters" vol. 94, no. 2, 020403 (2005) (cited on page 66).
- ¹⁹⁰S. Raghavan, A. Smerzi, S. Fantoni, and S. Shenoy: *Coherent oscillations between two weakly coupled Bose-Einstein condensates: Josephson effects, π oscillations, and macroscopic quantum self-trapping*, "Physical Review A" vol. 59, no. 1, 620 (1999) (cited on page 67).

- ¹⁹¹G. Valtolina, A. Burchianti, A. Amico, E. Neri, K. Khani, J. A. Seman, A. Trombettoni, A. Smerzi, M. Zaccanti, M. Inguscio, et al.: *Josephson effect in fermionic superfluids across the BEC-BCS crossover*, "Science" vol. 350, no. 6267, 1505–1508 (2015) (cited on page 68).
- ¹⁹²A. Burchianti, F. Scazza, A. Amico, G. Valtolina, J. Seman, C. Fort, M. Zaccanti, M. Inguscio, and G. Roati: *Connecting dissipation and phase slips in a Josephson junction between fermionic superfluids*, "Physical Review Letters" vol. 120, no. 2, 025302 (2018) (cited on pages 68, 69, 75).
- ¹⁹³W. Kwon, G. Del Pace, R. Panza, M. Inguscio, W. Zwerger, M. Zaccanti, F. Scazza, and G. Roati: *Strongly correlated superfluid order parameters from dc Josephson supercurrents*, "arXiv preprint arXiv:1908.09696" (2019) (cited on pages 68, 90).
- ¹⁹⁴M. Zaccanti and W. Zwerger: *Critical Josephson current in BCS-BEC crossover superfluids*, "arXiv:1907.08052" (2019) (cited on pages 68, 90, 93).
- ¹⁹⁵J. G. Lee, B. J. McIlvain, C. Lobb, and W. Hill III: *Analogs of basic electronic circuit elements in a free-space atom chip*, "Sci. Rep." vol. 3, 1034 (2013) (cited on pages 69, 75).
- ¹⁹⁶S. Eckel, J. G. Lee, F. Jendrzejewski, C. Lobb, G. Campbell, and W. Hill III: *Contact resistance and phase slips in mesoscopic superfluid-atom transport*, "Physical Review Letters" vol. 93, no. 6, 063619 (2016) (cited on pages 69, 75).
- ¹⁹⁷P. Murthy, D. Kedar, T. Lompe, M. Neidig, M. Ries, A. Wenz, G. Zürn, and S. Jochim: *Matter-wave Fourier optics with a strongly interacting two-dimensional Fermi gas*, "Physical Review Letters" vol. 90, no. 4, 043611 (2014) (cited on page 73).
- ¹⁹⁸V. P. Singh, N. Luick, L. Sobirey, and L. Mathey: *Josephson junction dynamics in a two-dimensional ultracold Bose gas*, "arXiv preprint arXiv:2002.08375" (2020) (cited on pages 76, 83, 90, 91, 93).
- ¹⁹⁹V. P. Singh, C. Weitenberg, J. Dalibard, and L. Mathey: *Superfluidity and relaxation dynamics of a laser-stirred two-dimensional Bose gas*, "Physical Review Letters" vol. 95, no. 4, 043631 (2017) (cited on page 76).
- ²⁰⁰S. Eckel, F. Jendrzejewski, A. Kumar, C. Lobb, and G. Campbell: *Interferometric measurement of the current-phase relationship of a superfluid weak link*, "Physical Review Letters" vol. 4, no. 3, 031052 (2014) (cited on pages 79, 80).
- ²⁰¹F. M. Fernández: *Introduction to perturbation theory in quantum mechanics*, in, CRC press 2000, p. 197 (cited on page 85).
- ²⁰²D. Bishop and J. Reppy: *Study of the superfluid transition in two-dimensional He 4 films*, "Physical Review Letters" vol. 40, no. 26, 1727 (1978) (cited on page 87).

- ²⁰³A. Polkovnikov, E. Altman, and E. Demler: *Interference between independent fluctuating condensates*, “Proceedings of the National Academy of Sciences of the United States of America” vol. 103, no. 16, 6125–6129 (2006) (cited on page 87).
- ²⁰⁴N. V. Prokof’ev and B. V. Svistunov: *Algebraic Time Crystallization in a Two-dimensional Superfluid*, “J. Exp. Theor. Phys.” vol. 127, no. 5, 860–864 (2018) (cited on page 90).
- ²⁰⁵Z. Hadzibabic, P. Krüger, M. Cheneau, B. Battelier, and J. Dalibard: *Berezinskii–Kosterlitz–Thouless crossover in a trapped atomic gas*, “Nature” vol. 441, no. 7097, 1118 (2006) (cited on page 90).
- ²⁰⁶C. Mora and Y. Castin: *Extension of Bogoliubov theory to quasicondensates*, “Physical Review A” vol. 67, no. 5, 053615 (2003) (cited on page 90).
- ²⁰⁷F. Meier and W. Zwerger: *Josephson tunneling between weakly interacting Bose-Einstein condensates*, “Physical Review Letters” vol. 64, no. 3, 033610 (2001) (cited on page 93).
- ²⁰⁸M. Bohlen, L. Sobirey, N. Luick, H. Biss, T. Enss, T. Lompe, and H. Moritz: *Sound propagation and quantum limited damping in a two-dimensional Fermi gas*, “arXiv preprint arXiv:2003.02713” (2020) (cited on page 96).
- ²⁰⁹M. Bohlen: *in preparation*, PhD thesis, Universität Hamburg 2020 (cited on page 96).
- ²¹⁰J. Ville, R. Saint-Jalm, É. Le Cerf, M. Aidelsburger, S. Nascimbène, J. Dalibard, and J. Beugnon: *Sound propagation in a uniform superfluid two-dimensional Bose gas*, “Physical Review Letters” vol. 121, no. 14, 145301 (2018) (cited on page 96).
- ²¹¹M. Ota and S. Stringari: *Second sound in a two-dimensional Bose gas: From the weakly to the strongly interacting regime*, “Physical Review A” vol. 97, no. 3, 033604 (2018) (cited on page 96).
- ²¹²T. Schäfer and D. Teaney: *Nearly perfect fluidity: from cold atomic gases to hot quark gluon plasmas*, “Reports on Progress in Physics” vol. 72, no. 12, 126001 (2009) (cited on page 96).
- ²¹³L. Sobirey, N. Luick, M. Bohlen, H. Biss, H. Moritz, and T. Lompe: *Observation of superfluidity in a strongly correlated two-dimensional Fermi gas*, “arXiv preprint arXiv:2005.07607” (2020) (cited on page 97).
- ²¹⁴L. Sobirey: *in preparation*, PhD thesis, Universität Hamburg 2020 (cited on page 97).
- ²¹⁵L.-C. Ha, L. W. Clark, C. V. Parker, B. M. Anderson, and C. Chin: *Roton-maxon excitation spectrum of Bose condensates in a shaken optical lattice*, “Physical Review Letters” vol. 114, no. 5, 055301 (2015) (cited on page 97).
- ²¹⁶L. Landau: *Theory of the Superfluidity of Helium II*, “Physical Review” vol. 60, no. 4, 356 (1941) (cited on page 97).

- ²¹⁷C. Raman, M. Köhl, R. Onofrio, D. Durfee, C. Kuklewicz, Z. Hadzibabic, and W. Ketterle: *Evidence for a critical velocity in a Bose-Einstein condensed gas*, “Physical Review Letters” vol. 83, no. 13, 2502 (1999) (cited on page 97).
- ²¹⁸R. Desbuquois, L. Chomaz, T. Yefsah, J. Léonard, J. Beugnon, C. Weitenberg, and J. Dalibard: *Superfluid behaviour of a two-dimensional Bose gas*, “Nature Physics” vol. 8, no. 9, 645–648 (2012) (cited on page 97).
- ²¹⁹M. R. Matthews, B. P. Anderson, P. Haljan, D. Hall, C. Wieman, and E. Cornell: *Vortices in a Bose-Einstein condensate*, “Physical Review Letters” vol. 83, no. 13, 2498 (1999) (cited on page 99).
- ²²⁰J. R. Abo-Shaeer, C. Raman, J. M. Vogels, and W. Ketterle: *Observation of Vortex Lattices in Bose-Einstein Condensates*, “Science” vol. 292, no. 5516, 476–479 (2001) (cited on page 99).
- ²²¹W. Ketterle, D. Durfee, and D. Stamper-Kurn: *Making, probing and understanding Bose-Einstein condensates*, in *Bose-Einstein condensation in atomic gases*, edited by M. Inguscio, S. Stringari, and C. Wieman, Proceedings of the International School of Physics “Enrico Fermi”, Course CXL (1999), pp. 67–176 (cited on pages 100, 102).
- ²²²T. Yefsah, R. Desbuquois, L. Chomaz, K. J. Günter, and J. Dalibard: *Exploring the Thermodynamics of a Two-Dimensional Bose Gas*, “Physical Review Letters” vol. 107, 130401 (2011) (cited on page 100).
- ²²³C. J. Foot: *Atomic physics*, Vol. 7, Oxford University Press 2005 (cited on page 101).
- ²²⁴L. Chomaz, L. Corman, T. Yefsah, R. Desbuquois, and J. Dalibard: *Absorption imaging of a quasi-two-dimensional gas: a multiple scattering analysis*, “New Journal of Physics” vol. 14, no. 5, 055001 (2012) (cited on page 103).
- ²²⁵M. G. Ries, A. N. Wenz, G. Zürn, L. Bayha, I. Boettcher, D. Kedar, P. A. Murthy, M. Neidig, T. Lompe, and S. Jochim: *Observation of Pair Condensation in the Quasi-2D BEC-BCS Crossover*, “Physical Review Letters” vol. 114, 230401 (2015) (cited on page 103).
- ²²⁶M. Horikoshi, A. Ito, T. Ikemachi, Y. Aratake, M. Kuwata-Gonokami, and M. Koashi: *Accurate in situ acquisition of column density of a dense cloud of ultracold ^6Li atoms using absorption imaging*, “arXiv:1608:07152” (2016) (cited on page 103).

DANKSAGUNG

Diese Arbeit wäre nicht möglich gewesen ohne die Unterstützung einer Vielzahl von Personen, denen ich hier danken will.

Als erstes möchte ich Henning danken. Bereits zu Beginn meines Physikstudiums hat mich deine Begeisterung für Physik inspiriert. Seit meiner Bachelorarbeit in deiner Gruppe hast du mir stets als Mentor zur Seite gestanden und mit deiner engagierten Betreuung maßgeblich zu meinem Werdegang beigetragen. Du schaffst es in deiner Gruppe eine Arbeitsatmosphäre zu schaffen, in der sich alle wertgeschätzt fühlen und toll zusammenarbeiten. Vielen Dank dafür!

Danke Lennart und Thomas für die tolle Zusammenarbeit, die zahllosen Diskussionen über Physik und die Welt, und nicht zuletzt die wundervollen Road Trips und Wanderungen mit euch, an die ich mich immer gerne zurückerinnere. Danke Markus, Hauke, Alexandra, Martin und Phillip! Mir hat es sehr viel Spaß gemacht mit euch zusammenzuarbeiten.

Ebenso danken möchte ich Wolf, Kai, Jonas und Klaus, dafür, dass ihr mich bereits während meiner Bachelor- und Masterarbeit so gut ins Team aufgenommen und mit dem Experiment vertraut gemacht habt. Ihr habt dafür gesorgt, dass ich mich von Anfang an in der Gruppe wohlfühlt habe.

Danke auch an Ludwig und Vijay für die vielen aufschlussreichen Diskussionen und die Geduld, mit der ihr unsere Fragen beantwortet habt.

Mein Dank gilt ebenfalls Klaus Sengstock, Reinhard Mielck, Ralf Lühr, Ellen Gloy, Janina Neubert, Loreen Tornier und den zahlreichen Mitarbeiterinnen und Mitarbeitern in der Verwaltung und der Werkstatt, ohne deren Engagement unsere Forschungsarbeit am Institut nicht möglich wäre.

Nicht zuletzt gilt mein Dank meiner Familie, meinen Freunden und meiner Freundin Kendra. Ich bin so dankbar solch wundervolle Menschen in meinem Leben zu haben.

EIDESSTATTLICHE VERSICHERUNG

Hiermit versichere ich an Eides statt, die vorliegende Dissertationschrift selbst verfasst und keine anderen als die angegebenen Hilfsmittel und Quellen benutzt zu haben.

Die eingereichte schriftliche Fassung entspricht der auf dem elektronischen Speichermedium.

Die Dissertation wurde in der vorgelegten oder einer ähnlichen Form nicht schon einmal in einem früheren Promotionsverfahren angenommen oder als ungenügend beurteilt.

Hamburg, den 19.05.2020



Niclas Clemens Luick